

Università degli Studi di Napoli “Federico II”

Scuola Politecnica e delle Scienze di Base
Area Didattica di Scienze Matematiche Fisiche e Naturali

Dipartimento di Fisica “Ettore Pancini”



Laurea Magistrale in Fisica

Study of the $B \rightarrow \tau\nu$ decay with the Belle II experiment

Relatori:

Prof. Guglielmo De Nardo
Dott. Mario Merola

Candidato:

Daniele Buono
Matricola N94/000331

A.A. 2018/2019

Contents

Introduction	1
1 Flavour Physics and leptonic decays of B mesons	4
1.1 Introduction to Flavour Physics and CKM matrix	4
1.1.1 Parameterizations of CKM matrix	8
1.1.2 Unitarity triangle	10
1.2 Theory of the Leptonic B decays	13
1.2.1 $B \rightarrow \tau\nu$ decay in New Physics models	15
1.2.2 τ decay modes	16
2 Belle II experiment	19
2.1 B-Factory and physics motivations	19
2.2 SuperKEKB collider	22
2.2.1 Nano-beams scheme	25
2.2.2 Beam-induced background	26
2.3 Belle II detector	27
2.3.1 Detector overview	27
2.3.2 Vertex Detector	29
2.3.3 Central Drift Chamber	31
2.3.4 TOP and ARICH	33
2.3.5 Electromagnetic Calorimeter	35
2.3.6 Magnet	36
2.3.7 Neutral kaons and muons system	37
2.3.8 Trigger	38

3	A preliminary look at Phase II data with $\tau^+ - \tau^-$ sample	40
3.1	Overview on BASF2	41
3.2	Preselection on data sample	43
3.3	Signal selection	46
3.4	Data-MonteCarlo agreement	52
3.5	Data-driven technique	61
4	Study of $B \rightarrow \tau\nu$ decay	69
4.1	Dataset	70
4.2	Signal event selection	71
	4.2.1 Full Event Interpretation	72
	4.2.2 Event selection for B_{sig}	76
4.3	Selection optimization	84
4.4	Signal Cross Feeds	93
4.5	Expected number of signal events and statistical significance .	96
4.6	Expected systematic uncertainties	101
4.7	Projections	101
4.8	Data-MonteCarlo agreement	103
4.9	Signal extraction and branching ratio measurement on data- challenge sample	106
	Conclusions	114
	Bibliography	117

List of Figures

1.1	The Unitarity Triangle.	11
1.2	Feynman diagram of a leptonic B decay.	13
1.3	Constraints on Unitarity Triangle from CKMFitter Collaboration [15].	15
1.4	Tree level diagram of $B \rightarrow l\nu$ decay through a charged Higgs.	15
1.5	Feynman diagram of $\tau \rightarrow l\bar{\nu}_l\nu_\tau$ decay.	16
1.6	Feynman diagram of $\tau \rightarrow \pi\nu_\tau$ decay.	17
1.7	Feynman diagram of $\tau \rightarrow 3\pi\nu_\tau$ decay through a_1 resonance.	17
2.1	Goal of SuperKEKB and Belle II in terms of instantaneous and integrated luminosity.	22
2.2	SuperKEKB collider structure.	23
2.3	SuperKEKB parameters respect to KEKB.	25
2.4	Geometry of the interaction point in the nano-beams scheme.	26
2.5	Structure of Belle II detector.	29
2.6	View of Silicon Pixel Detector.	30
2.7	View of Silicon Vertex Detector.	31
2.8	View of Central Drift Chamber.	32
2.9	Scheme of a single module of Time of Propagation Counter.	34
2.10	Scheme of Aerogel Ring-Imaging Čerenkov counter structure.	35
3.1	Schematization of processes that conduct from raw data to analyzable data.	42
3.2	BASF2 architecture.	43
3.3	Offline luminosity and run range of prod6 data sample.	43

3.4	$ \sum_{i=0}^2 \cos\theta_{Thrust_0_i} $ distribution of charged tracks on 3-prong side.	48
3.5	$ \cos\theta_{Thrust_1_0} $ distribution of charged track on 1-prong side.	48
3.6	FOM and μ_{rej}^{bkg} vs ϵ_{sel}^{sig} plots for both selection optimizations on $\sum_{i=0}^2 \cos\theta_{Thrust_0_i}$ and $\cos\theta_{thrust_1_0}$	51
3.7	Comparison of data (dots) and MC (histograms) distributions of $ \sum_{i=0}^2 \cos\theta_{thrust_0_i} $ variable.	53
3.8	Comparison of data (dots) and MC (histograms) distributions of $ \cos\theta_{thrust_1_0} $ variable.	53
3.9	Comparison of data (dots) and MC (histograms) distributions of $p_{trk}^{3-prong}$ variable.	54
3.10	Comparison of data (dots) and MC (histograms) distributions of $p_{trk}^{1-prong}$ variable.	54
3.11	Comparison of data (dots) and MC (histograms) distributions of $E_{ECL}^{3-prong}$ variable.	55
3.12	Comparison of data (dots) and MC (histograms) distributions of $E_{ECL}^{1-prong}$ variable.	55
3.13	Comparison of data (dots) and MC (histograms) distributions of $E/p _{3-prong}$ variable.	56
3.14	Comparison of data (dots) and MC (histograms) distributions of $E/p _{1-prong}$ variable.	56
3.15	Comparison of data (dots) and MC (histograms) distributions of p_{miss} variable.	57
3.16	Comparison of data (dots) and MC (histograms) distributions of $\theta_{p_{miss}}$ variable.	57
3.17	Comparison of data (dots) and MC (histograms) distributions of $\theta_{ECL}^{3-prong}$ variable.	58
3.18	Comparison of data (dots) and MC (histograms) distributions of $\theta_{ECL}^{1-prong}$ variable.	58
3.19	Comparison of data (dots) and MC (histograms) distributions of $M_{inv}^{3-prong}$ variable.	59
3.20	Comparison of data (dots) and MC (histograms) distributions of M_{miss}^2 variable.	59

3.21	Comparison of data (dots) and MC (histograms) distributions of E_{vis}^{CMS} variable.	60
3.22	Comparison of data (dots) and MC (histograms) distributions of E_{miss}^{CMS} variable.	60
3.23	E/p 1-prong MC distribution splitted in particle species contributes.	62
3.24	E/p 3-prong MC distribution in which the signal plus background component is scaled to the hadronic fraction f_{had}	63
3.25	Resulting subtraction between $E/p^{1-prong}$ and scaled $E/p^{3-prong}$ distribution both for data and MC and their agreement.	63
3.26	Resulting subtraction between $E/p^{1-prong}$ and scaled $E/p^{3-prong}$ distributions both for data and MC and their agreement, in ranges of momentum and angular regions of ECL.	67
4.1	Decay of $\Upsilon(4S)$ into a charged B meson pair. The signal-side is shown on the right and an example of tag-side on the left.	71
4.2	Hierarchical approach of the Full Event Interpretation.	73
4.3	$SigProb$ distribution for $B\bar{B}$ background (blue), continuum (green) and τ pair (light green).	75
4.4	M_{bc} distribution before the cut on M_{bc} for signal (red, enhanced by a factor 15), $B\bar{B}$ background (blue), continuum (green) and τ pair (light green).	77
4.5	M_{miss}^2 distribution for leptonic mode for signal (red, enhanced by a factor 10), $B\bar{B}$ background (blue), continuum (green) and τ pair (light green).	78
4.6	M_{miss}^2 distribution for hadronic mode for signal (red, enhanced by a factor 10), $B\bar{B}$ background (blue), continuum (green) and τ pair (light green).	78
4.7	R_2 as input to the BDT. Blue histogram represents the signal and red histogram represents the background.	79
4.8	$\cos\theta_{Thrust}$ as input to the BDT. Blue histogram represents the signal and red histogram represents the background.	80
4.9	Example of Cleo Clones (02) as input to the BDT. Blue histogram represents the signal and red histogram represents the background.	80

4.10	Example of Super-Fox-Wolfram moment (02) as input to the BDT. Blue histogram represents the signal and red histogram represents the background.	81
4.11	BDT_{cont} distribution for leptonic mode for signal (red, enhanced by a factor 10), $B\bar{B}$ background (blue), continuum (green) and τ pair (light green).	81
4.12	BDT_{cont} distribution for hadronic mode for signal (red, enhanced by a factor 10), $B\bar{B}$ background (blue), continuum (green) and τ pair (light green).	82
4.13	P^* distribution for hadronic mode for signal (red, enhanced by a factor 10), $B\bar{B}$ background (blue), continuum (green) and τ pair (light green).	83
4.14	P_{miss} distribution for hadronic mode for signal (red, enhanced by a factor 10), $B\bar{B}$ background (blue), continuum (green) and τ pair (light green).	83
4.15	E_{Extra} distribution for signal (red, enhanced by a factor 20), $B\bar{B}$ background (blue), continuum (green) and τ pair (light green).	84
4.16	E_{Extra} distribution for signal (red, enhanced by a factor 10), $B\bar{B}$ background (blue), continuum (green) and τ pair (light green) in the $E_{Extra} < 1 GeV$ window.	85
4.17	Comparison between E_{Extra} shapes for both signal (scaled to background histogram integral) and background in the $E_{Extra} < 1 GeV$ window.	85
4.18	Plot of S_{L1} as a function of cut on $SigProb$	86
4.19	Signal yield distribution after 20000 pseudo-experiments (with the condition $SigProb > 0.015$).	87
4.20	Background yield distribution after 20000 pseudo-experiments (with the condition $SigProb > 0.015$).	87
4.21	Extended maximum likelihood fit to pseudo-data E_{Extra} distribution as a result of a toy experiment (with the condition $SigProb > 0.015$). The red and blue histograms represent the signal and background fit functions (templates from simulation). The black histogram is the result of fit.	88

4.22	Plot of S_{L1} as a function of cut on $(BDT_{cont})_{lep}$.	89
4.23	Plot of S_{L1} as a function of cut on $(BDT_{cont})_{had}$.	89
4.24	Plot of S_{L1} as a function of cut on $SigProb$.	90
4.25	Plot of S_{L1} as a function of cut on $(BDT_{cont})_{lep}$.	90
4.26	Plot of S_{L1} as a function of cut on $(BDT_{cont})_{lep}$.	91
4.27	Plot of S_{L1} as a function of cut on P^* .	92
4.28	Plot of S_{L1} as a function of cut on P_{miss} .	92
4.29	E_{Extra} distribution after applying all selection criteria for signal (red, enhanced by a factor 2), $B\bar{B}$ background (blue), continuum (green) and τ pair (light green).	93
4.30	E_{Extra} distribution for the e^- mode with reconstructed signal (red) and cross feeds (green, blue and magenta). The black histogram is the sum of them.	94
4.31	E_{Extra} distribution for the μ^- mode with reconstructed signal (green) and cross feeds (red, blue and magenta). The black histogram is the sum of them.	94
4.32	E_{Extra} distribution for the π^- mode with reconstructed signal (blu) and cross feeds (red, green and magenta). The black histogram is the sum of them.	95
4.33	E_{Extra} distribution for the $\pi^-\pi^0$ mode with reconstructed signal (magenta) and cross feeds (red, green and blue). The black histogram is the sum of them.	95
4.34	Extended maximum likelihood fit to E_{Extra} distribution as a result of a toy experiment for the $\tau^- \rightarrow e^- \bar{\nu}_e \nu_\tau$ mode.	97
4.35	Extended maximum likelihood fit to E_{Extra} distribution as a result of a toy experiment for the $\tau^- \rightarrow \mu^- \bar{\nu}_\mu \nu_\tau$ mode.	97
4.36	Extended maximum likelihood fit to E_{Extra} distribution as a result of a toy experiment for the $\tau^- \rightarrow \pi^- \nu_\tau$ mode.	98
4.37	Extended maximum likelihood fit to E_{Extra} distribution as a result of a toy experiment for the $\tau^- \rightarrow \pi^- \pi^0 \nu_\tau$ mode.	98
4.38	Extended maximum likelihood fit to E_{Extra} distribution as a result of a toy experiment for all of the four τ 1-prong decay modes.	99
4.39	Hypothesis test for the expected statistical significance.	100

4.40	Plot of statistical uncertainty as a function of integrated luminosity.	102
4.41	Plot of statistical significance as a function of integrated luminosity.	102
4.42	Data/MC agreement in the M_{bc} sideband for BDT_{cont} , $SigProb$, ΔE , M_{bc} , M_{miss}^2 , P_{miss} , P^* , E_{Extra} distributions for $B\bar{B}$ background (blue), continuum (green), τ pair (light green) and data (dots).	104
4.43	Data/MC agreement in the E_{Extra} sideband for BDT_{cont} , $SigProb$, ΔE , M_{bc} , M_{miss}^2 , P_{miss} , P^* , E_{Extra} distributions for $B\bar{B}$ background (blue), continuum (green), τ pair (light green) and data (dots).	106
4.44	Extended maximum likelihood fit to E_{Extra} distribution on data-challenge sample for the $\tau^- \rightarrow e^- \bar{\nu}_e \nu_\tau$ mode.	107
4.45	Extended maximum likelihood fit to E_{Extra} distribution on data-challenge sample for the $\tau^- \rightarrow \mu^- \bar{\nu}_\mu \nu_\tau$ mode.	107
4.46	Extended maximum likelihood fit to E_{Extra} distribution on data-challenge sample for the $\tau^- \rightarrow \pi^- \nu_\tau$ mode.	108
4.47	Extended maximum likelihood fit to E_{Extra} distribution on data-challenge sample for the $\tau^- \rightarrow \pi^- \pi^0 \nu_\tau$ mode.	108
4.48	Extended maximum likelihood fit to E_{Extra} distribution on data-challenge sample for all of the four τ 1-prong decay modes.	109
4.49	Simultaneous fit to E_{Extra} distribution on data-challenge sample for the $\tau^- \rightarrow e^- \bar{\nu}_e \nu_\tau$ mode.	110
4.50	Simultaneous fit to E_{Extra} distribution on data-challenge sample for the $\tau^- \rightarrow \mu^- \bar{\nu}_\mu \nu_\tau$ mode.	111
4.51	Simultaneous fit to E_{Extra} distribution on data-challenge sample for the $\tau^- \rightarrow \pi^- \nu_\tau$ mode.	111
4.52	Simultaneous fit to E_{Extra} distribution on data-challenge sample for the $\tau^- \rightarrow \pi^- \pi^0 \nu_\tau$ mode.	112

List of Tables

1.1	Branching ratio of the main τ -decay modes.	17
3.1	Background processes with corresponding cross sections at $\sqrt{s} = m_{\Upsilon(4S)}$	47
3.2	MonteCarlo fractions of electrons, muons, charged pions, charged kaons and protons in 1-prong side.	61
4.1	Categories of simulated events and corresponding generated pairs.	70
4.2	B^+ , B^0 and D decay modes included in the FEI.	74
4.3	Final selection of the signal region.	93
4.4	Summary of correctly-reconstructed efficiencies and cross feeds.	96
4.5	Selection efficiencies, average signal yields and statistical uncertainties resulting from 20000 toy experiments corresponding to the four τ 1-prong decay modes.	99
4.6	Expected uncertainties and statistical significances on the $B \rightarrow \tau\nu$ branching ratio measurement for different luminosity scenarios with hadronic tag method.	101
4.7	Signal yields resulting from extended binned maximum likelihood fits on E_{Extra} distributions on data-challenge sample and measured branching ratio corresponding to the four τ 1-prong decay modes.	109

Introduction

The present work has been developed at the University Federico II of Naples, within the Belle II collaboration. The Belle II experiment is an high energy physics experiment with headquarters at KEK laboratory in Tsukuba, Japan. Beams of electrons (7 GeV) and positrons (4 GeV) are injected in the SuperKEKB accelerator and collide at the energy of the $\Upsilon(4S)$ resonance, which decays mainly in a B mesons pair. The energy of the two beams is different in order to have a boost of the center of mass and be able to measure the time-dependent CP asymmetry. At the interaction point the Belle II general-purpose detector is installed.

This analysis is divided in two parts. In the first explorative-type part the τ -pairs production is studied on collision data collected during the so-called Phase II and corresponding to an integrated luminosity of 480 pb^{-1} . In particular, events from channels $\tau^\pm \rightarrow 3h^\pm(n\pi^0)\nu_\tau$ (3-prong decays) and $\tau^\pm \rightarrow h^\pm(n\pi^0)\nu_\tau$, $\tau^\pm \rightarrow \mu^\pm\bar{\nu}_\mu\nu_\tau$ and $\tau^\pm \rightarrow e^\pm\bar{\nu}_e\nu_\tau$ (1-prong decays), where $h^\pm = \pi^\pm, K^\pm$, are selected. After a selection optimized to enrich the data sample in signal events, the distributions of the main variables are compared to evaluate the agreement between experimental data and MonteCarlo simulation. Subsequently a data-driven technique is developed to obtain a separation of electron and muon candidates based on the ratio between the energy released in the electromagnetic calorimeter and the momentum of the track measured by the drift chamber in order to easily count electrons and muons in a certain phase space region without any use of particle identification criteria.

The second part consists in the sensitivity study of the $B \rightarrow \tau\nu$ decay with MonteCarlo samples, corresponding to an integrated luminosity of 1600 fb^{-1} ,

and in the measurement of its branching ratio based on the data-challenge sample (1000 fb^{-1}).

From the Standard Model prediction:

$$\mathcal{B}(B \rightarrow \tau\nu) = \frac{G_F^2 m_B \tau_B}{8\pi} f_B^2 |V_{ub}|^2 m_\tau^2 \left(1 - \frac{m_\tau^2}{m_B^2}\right)^2, \quad (1)$$

it is possible to extract the product $f_B |V_{ub}|$, where f_B is the B meson decay constant and $|V_{ub}|$ is the Cabibbo-Kobayashi-Maskawa matrix element absolute value. The branching ratio is sensitive to physics beyond the Standard Model. In the Two Higgs Doublet Model, it is expressed as:

$$\mathcal{B}(B \rightarrow \tau\nu) = \mathcal{B}_{SM} \times \left(1 - \tan^2 \beta \frac{m_{B^\pm}^2}{m_{H^\pm}^2}\right), \quad (2)$$

where $\tan\beta$ is the ratio of the vacuum expectation values of the two Higgs fields and m_{H^\pm} is the mass of the charged Higgs. With this relation constraints on m_{H^\pm} and $\tan\beta$ can be imposed.

This work is composed of four chapters. The first chapter is an introduction to the Standard Model and the CKM matrix, the leptonic B decay theory and the $B \rightarrow \tau\nu$ branching ratio expression in the Standard Model and in a New Physics scenario. The second chapter introduces the Belle II experiment with the description of the SuperKEKB collider and the Belle II general-purpose detector. The third chapter describes the preliminary look at $e^+e^- \rightarrow \tau^+\tau^-$ events in Phase II data with the evaluation of the data-MonteCarlo agreements and the development of the data-driven technique. Finally, the fourth chapter is focused on the sensitivity study of the $B \rightarrow \tau\nu$ decay and on the measurement of its branching ratio.

Chapter 1

Flavour Physics and leptonic decays of B mesons

This chapter is an introduction to the theoretical framework relevant to the study of the leptonic decays of B mesons in the Standard Model and in models of New Physics. An overview of the phenomenology of electroweak interactions is given in order to introduce and to describe the Cabibbo-Kobayashi-Maskawa matrix, the most used parameterizations and the unitarity triangle. Since there are only leptons in the final state, the leptonic decays of B mesons are theoretically clear and the effect of the strong interactions are limited to a single decay constant f_B . The final sections are devoted to the possible effects on the $B \rightarrow \tau\nu$ decay from models of New Physics and to a brief description of the most abundant τ decay modes.

1.1 Introduction to Flavour Physics and CKM matrix

The Fermi's theory of the β -decay and the subsequent developments led to a phenomenological description of weak interactions characterized by the Lagrangian:

$$\mathcal{L}_F = \frac{G_F}{\sqrt{2}} J_\mu J^{\mu\dagger} \quad (1.1)$$

where $G_F \simeq 1.16 \times 10^{-5} \text{ GeV}^{-2}$ is the Fermi constant. Here \mathcal{L}_F describes a contact interaction between the *weak currents* J_μ , that include a weak leptonic current (l_μ) and a weak hadronic current (h_μ):

$$J_\mu = l_\mu + h_\mu = \hat{f} \gamma_\mu (1 - \gamma_5) \hat{i} \quad (1.2)$$

where \hat{i} is the initial fermionic field operator, \hat{f} the final fermionic field operator and $P_L \equiv (1 - \gamma_5)/2$ is the left-handed chiral projection operator such that:

$$\bar{f} \gamma_\mu P_L i \rightarrow f_L \gamma_\mu i_L.$$

Only left-handed particles are involved in the interaction. This is a consequence of the vectorial-axial ($V - A$) current structure. Each chiral projection is a combination of both positive and negative helicity states and only in the relativistic limit a left-handed 1/2-spin particle become a pure $-1/2$ helicity state. As the weak interactions are parity-violating, a term non-invariant under parity transformation is needed [1, 2]. Among all the possibles bilinear Lorentz-invariant forms, only the $V - A$ combination produces particles with the left chirality and maximizes the parity violation [3]. According to the gauge principle in the Standard Model (SM) the weak interaction is written starting from the free Lagrangian [4, 5]:

$$\mathcal{L}_0 = i \bar{\psi}_L \gamma^\mu \partial_\mu \psi_L + i \bar{\psi}_R \gamma^\mu \partial_\mu \psi_R \quad (1.3)$$

where ψ_L and ψ_R stands for the left- and right-handed fields. This Lagrangian has two symmetries. The first is the $U(1)$ ipercharge symmetry Y :

$$\psi_L \rightarrow \psi'_L = e^{g' \frac{i}{2} Y \alpha} \psi_L \quad \psi_R \rightarrow \psi'_R = e^{g' \frac{i}{2} Y \alpha} \psi_R. \quad (1.4)$$

The second is the isotopic $SU(2)$ symmetry with the Pauli's matrices τ_i being the generators:

$$\psi_L \rightarrow \psi'_L = e^{g \frac{i}{2} \vec{\tau} \cdot \vec{\omega}} \psi_L \quad \psi_R \rightarrow \psi'_R = \psi_R. \quad (1.5)$$

The theory is invariant under these global transformations. The extension of the invariance to local transformations is obtained by substituting $\alpha \rightarrow \alpha(x)$ and $\vec{\omega} \rightarrow \vec{\omega}(x)$ which allows to build a gauge theory. The interactions are de-

rived introducing a covariant derivative for each symmetry of the Lagrangian. The electroweak interaction is written as:

$$\mathcal{L}_{int}^{EW} = \mathcal{L}_{CC} + \mathcal{L}_{NC} \quad (1.6)$$

where \mathcal{L}_{CC} and \mathcal{L}_{NC} are the charged and neutral interaction currents.

The quark flavour changing transitions are governed by:

$$\mathcal{L}_{CC} = \frac{g}{2\sqrt{2}}(J_\mu W^{+\mu} + J_\mu^\dagger W^{-\mu}) \quad (1.7)$$

where g is the $SU(2)_L$ coupling constant, J_μ is the charged current and $W^{+\mu}$ is the field operator that annihilate quarks and W respectively. In the quark sector the current has the following structure after the symmetry breaking:

$$J_\mu = \sum_{ij} V_{ij} J_{ij}^\mu = \sum_{ij} \bar{u}_i \gamma^\mu \frac{1}{2}(1 - \gamma_5) V_{ij} d_j \quad (1.8)$$

where V_{ij} are the elements of a unitary 3×3 matrix called Cabibbo-Kobayashi-Maskawa (CKM) matrix.

The interactions in the Standard Model are described by the gauge symmetry $SU(3)_C \otimes SU(2)_L \otimes U(1)_Y$. $SU(3)_C$ is the gauge symmetry for the QCD whose generators are the Gell-Mann matrices λ^a [6]. The overall theory is governed by the Lagrangian:

$$\mathcal{L} = \mathcal{L}(QCD) + \mathcal{L}(SU(2)_L \otimes U(1)_Y) + \mathcal{L}(Higgs). \quad (1.9)$$

The strong interactions are mediated by the eight gluons G_a , the electroweak interactions by the W^\pm , Z^0 and γ bosons and the Higgs neutral boson H^0 .

In the SM quarks and leptons are disposed in $SU(2)_L$ left-handed doublets:

$$\begin{pmatrix} \nu_e \\ e^- \end{pmatrix}_L \quad \begin{pmatrix} \nu_\mu \\ \mu^- \end{pmatrix}_L \quad \begin{pmatrix} \nu_\tau \\ \tau^- \end{pmatrix}_L \quad (1.10)$$

$$\begin{pmatrix} u \\ d' \end{pmatrix}_L \quad \begin{pmatrix} c \\ s' \end{pmatrix}_L \quad \begin{pmatrix} t \\ b' \end{pmatrix}_L \quad (1.11)$$

while the corresponding right-handed fields are singlets under $SU(2)_L$. The

flavour of quarks is conserved in all vertexes with neutral gauge bosons (Z^0 , γ and G_a). Otherwise charged current processes involving W^\pm bosons are flavour violating and the intensity of this violation is given by the gauge coupling constant g . This coupling constant is related to the Fermi constant by

$$\frac{G_F}{\sqrt{2}} = \frac{g^2}{8M_W^2}. \quad (1.12)$$

The CKM matrix ([7, 8]) connects the weak eigenstates (d' , s' , b') and the corresponding mass eigenstates (d , s , b):

$$\begin{pmatrix} d' \\ s' \\ b' \end{pmatrix} = \begin{pmatrix} V_{ud} & V_{us} & V_{ub} \\ V_{cd} & V_{cs} & V_{cb} \\ V_{td} & V_{ts} & V_{tb} \end{pmatrix} \begin{pmatrix} d \\ s \\ b \end{pmatrix} = V_{CKM} \begin{pmatrix} d \\ s \\ b \end{pmatrix}. \quad (1.13)$$

The same mixing matrix for the leptons would be the unit matrix in the hypothesis of null neutrino masses. The fermion masses are fundamental SM inputs. Both the fermion masses and the CKM elements values are originated by the fermion couplings with the Higgs field. The couplings of the Higgs field to the quarks are given by the Yukawa coupling (Y_{ij}) under the $SU(2)_L$ gauge symmetry. The Higgs doublets symmetry is spontaneously broken:

$$\begin{pmatrix} \phi^+ \\ \phi^0 \end{pmatrix} \rightarrow \frac{1}{\sqrt{2}} \begin{pmatrix} 0 \\ v + H(x) \end{pmatrix}$$

where v is the Higgs expectation value and $H(x)$ is the Higgs particle field. After the symmetry breaking:

$$\mathcal{L}_{Yukawa} = \sum_{i,j} [\bar{u}_{Li} Y_{ij} u_{Rj} + \bar{d}_{Li} Y'_{ij} d_{Rj} + h.c.] \frac{1}{\sqrt{2}} (v + H(x)). \quad (1.14)$$

The terms proportional to v couple the left- and right-handed components of the quark fields and generate the mass terms. To determine the quark mass eigenstates it is necessary to diagonalize the mass matrices:

$$m_{ij}^u \equiv \frac{-v}{\sqrt{2}} Y_{ij}, \quad m_{ij}^d \equiv \frac{-v}{\sqrt{2}} Y'_{ij}. \quad (1.15)$$

The diagonalization is given by unitary transformations:

$$u_{L(R)\alpha} = \left(U_{L(R)}^u \right)_{\alpha i} u_{L(R)i} \quad d_{L(R)\alpha} = \left(U_{L(R)}^d \right)_{\alpha i} d_{L(R)i}. \quad (1.16)$$

The charged current Lagrangian of quarks becomes:

$$\mathcal{L}_{CC} = -\frac{g}{\sqrt{2}} \bar{u}_{L\alpha} \left[\left(U_L^u \right)_{\alpha j} \left(U_L^d \right)_{j\beta}^\dagger \right] \gamma^\mu d_{L\beta} W_\mu^+ + h.c. \quad (1.17)$$

where $V_{\alpha\beta} = \left[U_L^u U_L^{d\dagger} \right]_{\alpha\beta}$ is the CKM unitary matrix.

1.1.1 Parameterizations of CKM matrix

A generic $n \times n$ unitary matrix is defined by means of $2n^2$ real parameters. The constraints from unitary conditions are expressed by n^2 equations:

$$\sum_j V_{ij}^* V_{jk} = \delta_{ik} \quad (1.18)$$

reducing the number of real parameters to n^2 . An additional reduction of the number parameters comes from the equation 1.8, where the interaction term appears in the form $\bar{u}_i \gamma^\mu V_{ij} d_j$: the relative field phases of the quark \bar{u}_i and d_j can be redefined to cancel $2n - 1$ parameters of the matrix. Eventually there are $(n - 1)^2$ free parameters. Considering only two families of quarks there would be one free parameter and the matrix would be written as:

$$V = \begin{pmatrix} \cos\theta_c & \sin\theta_c \\ -\sin\theta_c & \cos\theta_c \end{pmatrix} \quad (1.19)$$

where θ_c is the Cabibbo angle. This parameter introduces a rotation among the quarks and permits to justify the strong suppression of decays with flavour changing neutral current. The Kobayashi and Maskawa idea was to introduce a third generation of quark. In this way there are four parameters: three rotation angles and a physical phase (that cannot be canceled out), which is responsible of CP-violation in the SM.

The *standard parameterization* of the CKM matrix is [9]:

$$V_{CKM} = \begin{pmatrix} c_{12}c_{13} & s_{12}c_{13} & s_{13}e^{-i\delta_{13}} \\ -s_{12}c_{23} - c_{12}s_{23}s_{13}e^{i\delta_{13}} & c_{12}c_{23} - s_{12}s_{23}s_{13}e^{i\delta_{13}} & s_{23}c_{13} \\ s_{12}s_{23} - c_{12}c_{23}s_{13}e^{i\delta_{13}} & -c_{12}s_{23} - s_{12}c_{23}s_{13}e^{i\delta_{13}} & c_{23}c_{13} \end{pmatrix} \quad (1.20)$$

where $c_{ij} = \cos\theta_{ij}$, $s_{ij} = \sin\theta_{ij}$ (with $c_{ij}, s_{ij} \geq 0$) and δ_{13} ($\simeq 70^\circ$) is the CP-violating phase. The values of the rotation angles are:

$$\theta_{12} \simeq 12.9^\circ \quad \theta_{23} \simeq 2.4^\circ \quad \theta_{13} \simeq 0.2^\circ.$$

In this scheme the four elements V_{ud} , V_{us} , V_{cb} , and V_{tb} are real. The overall rotation is described by the product of three orthogonal rotation matrices (rotations of θ_{12} around z axis, θ_{13} around y axis and θ_{23} around z axis again):

$$V = \begin{pmatrix} 1 & 0 & 0 \\ 0 & c_{23} & s_{23} \\ 0 & -s_{23} & c_{23} \end{pmatrix} \begin{pmatrix} c_{13} & 0 & s_{13}e^{-i\delta} \\ 0 & 1 & 0 \\ -s_{13}e^{i\delta} & 0 & c_{13} \end{pmatrix} \begin{pmatrix} c_{12} & s_{12} & 0 \\ -s_{12} & c_{12} & 0 \\ 0 & 0 & 1 \end{pmatrix} \quad (1.21)$$

A more convenient representation of the CKM matrix is the *Wolfenstein parameterization* [10] where is made explicit an expansion in terms of the small parameter

$$\lambda = s_{12} = \sin\theta_{12} = |V_{us}| \simeq 0.22$$

due to the inequalities $s_{13} \ll s_{23} \ll s_{12} \ll 1$:

$$V_{CKM} = \begin{pmatrix} 1 - \frac{\lambda^2}{2} & \lambda & A\lambda^3(\rho - i\eta) \\ -\lambda & 1 - \frac{\lambda^2}{2} & A\lambda^2 \\ A\lambda^3(1 - \rho - i\eta) & -A\lambda^2 & 1 \end{pmatrix} + \mathcal{O}(\lambda^4). \quad (1.22)$$

The four independent real parameters are λ , A , ρ and η . The relation to the standard parameterization is given by [11]:

$$s_{12} = \lambda, \quad s_{23} = A\lambda^2 \simeq V_{cb}, \quad s_{13}e^{i\delta_{13}} = A\lambda^3(\rho + i\eta) = V_{ub}^*. \quad (1.23)$$

Instead of ρ and η , the parameters $\bar{\rho}$ and $\bar{\eta}$ are often used. They are defined by:

$$\bar{\rho} + i\bar{\eta} = -\frac{V_{ud}V_{ub}^*}{V_{cd}V_{cb}^*} \quad (1.24)$$

where at order $\mathcal{O}(\lambda^2)$:

$$\bar{\rho} = \rho \left(1 - \frac{\lambda^2}{2}\right), \quad \bar{\eta} = \eta \left(1 - \frac{\lambda^2}{2}\right). \quad (1.25)$$

Considering the order of magnitude of the elements in terms of λ powers, the hierarchical structure of the matrix is made explicit:

$$V_{CKM} \approx \begin{pmatrix} \lambda^0 & \lambda^1 & \lambda^3 \\ \lambda^1 & \lambda^0 & \lambda^2 \\ \lambda^3 & \lambda^2 & \lambda^0 \end{pmatrix}. \quad (1.26)$$

There are no explanations in the SM about the origin of this structure. From PDG [14] the measured values of CKM module elements are:

$$V_{CKM} = \begin{pmatrix} 0.97446 \pm 0.00010 & 0.22452 \pm 0.00044 & 0.00365 \pm 0.00012 \\ 0.22438 \pm 0.00044 & 0.97359^{+0.00010}_{-0.00011} & 0.04214 \pm 0.00076 \\ 0.00896^{+0.00024}_{-0.00023} & 0.04133 \pm 0.00074 & 0.999105 \pm 0.000032 \end{pmatrix}.$$

Finally the values of the Wolfenstein parameters result to be:

$$\lambda = 0.22453 \pm 0.00044 \quad A = 0.836 \pm 0.015 \quad \bar{\rho} = 0.122^{+0.018}_{-0.017} \quad \bar{\eta} = 0.355^{+0.012}_{-0.011}.$$

1.1.2 Unitarity triangle

The unitarity of the CKM matrix implies the existence of relations between the rows and the columns of the matrix itself. The following three relations involving the columns are of particular interest:

$$V_{ud}V_{us}^* + V_{cd}V_{cs}^* + V_{td}V_{ts}^* = 0 \quad (1.27)$$

$$V_{us}V_{ub}^* + V_{cs}V_{cb}^* + V_{ts}V_{tb}^* = 0 \quad (1.28)$$

$$V_{ud}V_{ub}^* + V_{cd}V_{cb}^* + V_{td}V_{tb}^* = 0. \quad (1.29)$$

They represent triangles in the complex plane (ρ, η) , called *unitarity triangles* (UT) [9, 12, 13]. The triangles have areas equal to $|J|/2$, where J is the *Jarlskog invariant* given by $\text{Im}[V_{ij}V_{kl}V_{il}^*V_{kj}^*] = J \sum_{m,n=1}^3 \epsilon_{ikm}\epsilon_{jln}$. In the Wolfenstein representation the Jarlskog invariant is $J = A^2\lambda^6\eta$. The triangles are invariant under any phase rotation. The most common used unitarity triangle is the one in eq. 1.29. The Wolfenstein parametrization permits to explain the reason: in terms of λ powers, in this triangle all of the three sides lengths are of the same magnitude order $\mathcal{O}(\lambda^3)$. Dividing it by the better known length, the UT is usually expressed as follow:

$$\frac{V_{ud}V_{ub}^*}{V_{cd}V_{cb}^*} + \frac{V_{td}V_{tb}^*}{V_{cd}V_{cb}^*} + 1 = 0 \quad (1.30)$$

where the vertices are $(0, 0)$, $(1, 0)$ and $(\bar{\rho}, \bar{\eta})$. The UT 1.30 is shown in Figure 1.1.

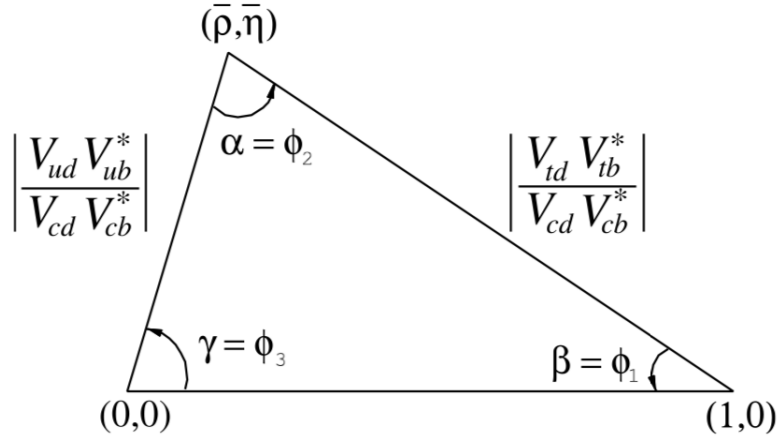


Figure 1.1: The Unitarity Triangle.

Moreover the angles are defined by:

$$\gamma = \text{arg} \left(-\frac{V_{ub}^* V_{ud}}{V_{cb}^* V_{cd}} \right) \quad (1.31)$$

$$\beta = \arg \left(-\frac{V_{tb}^* V_{td}}{V_{cb}^* V_{cd}} \right) \quad (1.32)$$

$$\alpha = \arg \left(-\frac{V_{tb}^* V_{td}}{V_{ub}^* V_{ud}} \right). \quad (1.33)$$

The angles β and γ are directly related to V_{td} and V_{ub} :

$$V_{td} = |V_{td}|e^{-i\beta}, \quad V_{ub} = |V_{ub}|e^{-i\gamma} \quad (1.34)$$

and so:

$$\gamma = \delta. \quad (1.35)$$

The UT together with $|V_{us}|$ and $|V_{cb}|$ provides a complete description of the CKM matrix. The CP-violating condition is $\eta \neq 0$ (or the area $|J|/2$ of the triangle must be not equal to 0). The angles of the UT can be determined by measurements of CP-violation and asymmetries in the B-mesons system:

- $\sin 2\beta$ from $B_d \rightarrow J/\psi K_S, \Phi K_S$;
- $\sin 2\alpha$ from $B_d \rightarrow \pi\pi, \rho\pi$;
- $\sin(2\beta + \gamma)$ from $B_d \rightarrow D\pi$ and $B_s \rightarrow D_s K$;
- γ from $B_d \rightarrow \pi\pi, DK$.

Current measurements from PDG are:

- $\sin 2\beta = 0.691 \pm 0.017$;
- $\alpha = \left(84.5_{-5.2}^{+5.9} \right)^\circ$;
- $\gamma = \left(73.5_{-5.1}^{+4.2} \right)^\circ$;
- $J = (3.18 \pm 0.15) \times 10^5$.

1.2 Theory of the Leptonic B decays

The purely leptonic decays $B \rightarrow l\nu_l$ are of particular interest due to their clear theoretical description. On the other hand, it can be challenging to observe them experimentally. The Feynman diagram for a leptonic B decay is shown in Figure 1.2.

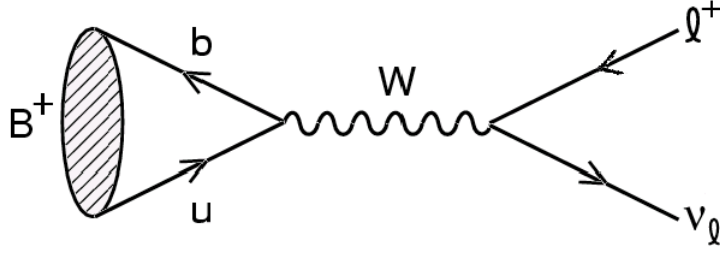


Figure 1.2: Feynman diagram of a leptonic B decay.

The B meson of mass m_B and four momentum p_μ contains a $u\bar{b}$ pair that annihilates into a W^+ going into a lepton-neutrino pair. The CKM element V_{ub} enters into the annihilation vertex and the four-momentum q_μ of the W is forced to have $q_\mu = p_\mu$ and $q^2 = m_B^2$. Since the final lepton-neutrino system does not interact strongly, the matrix element is factorized into a hadronic and a leptonic current:

$$M = \frac{G_F^2 m_B}{\sqrt{2}} V_{ub} \langle 0 | J_\mu | B \rangle \bar{u} \gamma_\mu (1 - \gamma_5) v \quad (1.36)$$

where u and v are the lepton and neutrino Dirac spinors. The current J_μ contributes with an axial term only. The hadronic current results to be:

$$i f_B p_\mu \quad (1.37)$$

where f_B is the B meson decay constant that is determined by strong inter-

actions. Using 1.36 and 1.37, the branching fraction in the SM is:

$$\mathcal{B}(B^- \rightarrow l^- \bar{\nu}_l) = \frac{G_F^2 m_B \tau_B}{8\pi} f_B^2 |V_{ub}|^2 m_l^2 \left(1 - \frac{m_l^2}{m_B^2}\right)^2, \quad (1.38)$$

where G_F is the Fermi coupling constant, m_l and m_B are the lepton and the B meson masses, τ_B is the B^- lifetime. The dependence of $\mathcal{B}(B^- \rightarrow l^- \bar{\nu})$ on the lepton mass is due to helicity so that low mass leptons are suppressed with respect to high mass leptons (which makes the τ channel the most favorite). The ratio between the rates for the lepton species $\tau : \mu : e$ is $\sim 1 : 10^{-3} : 10^{-7}$. The predicted values for the SM are found to be [21]:

$$\mathcal{B}_\tau = (7.7 \pm 0.6) \times 10^{-5}, \quad \mathcal{B}_\mu = (3.5 \pm 0.3) \times 10^{-7}, \quad \mathcal{B}_e = (8.1 \pm 0.6) \times 10^{-12}. \quad (1.39)$$

In the SM context the observation of $B^- \rightarrow l^- \bar{\nu}$ provides a first direct measurement of f_B ($|V_{ub}|$ is measured from semi-leptonic B meson decays). Viceversa if f_B is calculated precisely from QCD, the branching ratio measurement could infer precise information about $|V_{ub}|$ value. The ratio between parameters $|V_{ub}/V_{td}|$ is obtained by comparing $\mathcal{B}(B^- \rightarrow l^- \bar{\nu})$ with the difference in heavy and light neutral B_d masses (Δm_d , known from B_d mixing measurements). The constraints on the unitarity triangle from the measured values of Δm_d parameter are shown in Figure 1.3. Despite the theoretically clean dependence on relevant parameters, the experimental picture is more complicated. The muon channel is experimentally simpler but the helicity suppression makes this process quite rare. Regarding the τ channel, the necessity to reconstruct the τ lepton from its decay products and the presence of two or three undetectable neutrinos in the final state make the background rejection an experimental challenge.

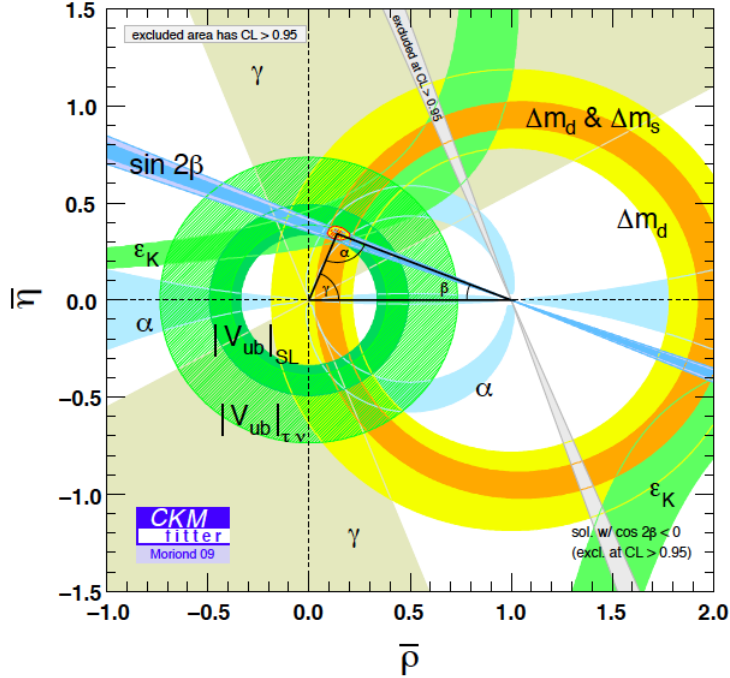


Figure 1.3: Constraints on Unitarity Triangle from CKMFitter Collaboration [15].

1.2.1 $B \rightarrow \tau\nu$ decay in New Physics models

The $B \rightarrow \tau\nu$ decay has an important impact in model beyond the Standard Model (BSM) because it allows to constraint parameter of New Physics (NP). In the two Higgs doublet model (2HDM) [16] the decay involves the contribution of a charged Higgs at tree level, as shown in Figure 1.4.

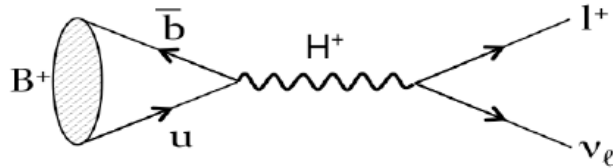


Figure 1.4: Tree level diagram of $B \rightarrow l\nu$ decay through a charged Higgs.

Charged Higgs Yukawa couplings are controlled by the parameter $\tan\beta = v_2/v_1$, the ratio of vacuum expectation values of the two doublets. The W^\pm and H^\pm induce the Fermi interaction

$$\frac{G_F}{\sqrt{2}} V_{ib} ([\bar{u}_i \gamma_\mu (1 - \gamma_5) b] [\bar{l} \gamma_\mu (1 - \gamma_5) \nu] - R_l [\bar{u}_i (1 + \gamma_5) b] [\bar{l} (1 - \gamma_5) \nu]) \quad (1.40)$$

where

$$R_l = \tan^2\beta (m_b m_l / m_{H^\pm}^2). \quad (1.41)$$

The pseudo-scalar coupling of the H^\pm boson is given by:

$$-i f_B (m_B^2 / m_b). \quad (1.42)$$

Finally the branching fraction results to be:

$$\mathcal{B}(B \rightarrow \tau \nu) = \mathcal{B}_{SM} \times \left(1 - \tan^2\beta \frac{m_{B^\pm}^2}{m_{H^\pm}^2} \right). \quad (1.43)$$

Comparing the measured value of the branching ratio and the SM prediction, it is possible to exclude regions in the $(m_{H^\pm}, \tan\beta)$ plane.

1.2.2 τ decay modes

Due to its mass ($m_\tau \sim 1.77 \text{ GeV}/c^2$), the τ is the only lepton that decays in hadrons. This is a powerful window in which to study QCD in the energy region less than 1 GeV . The main τ -decay modes are:

- leptonic decays, i.e. $\tau \rightarrow l \bar{\nu}_l \nu_\tau$ (Figure 1.5);

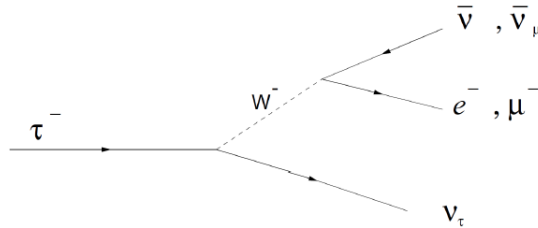


Figure 1.5: Feynman diagram of $\tau \rightarrow l \bar{\nu}_l \nu_\tau$ decay.

- hadronic decays, i.e. $\tau \rightarrow \pi\nu_\tau$, $\tau \rightarrow 3\pi\nu_\tau$ (Figure 1.6 and 1.7).

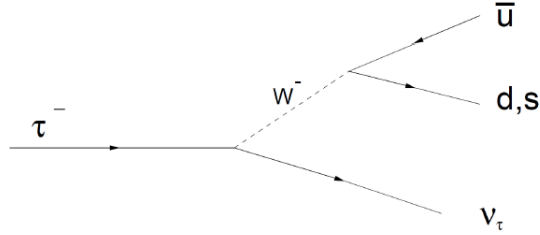


Figure 1.6: Feynman diagram of $\tau \rightarrow \pi\nu_\tau$ decay.

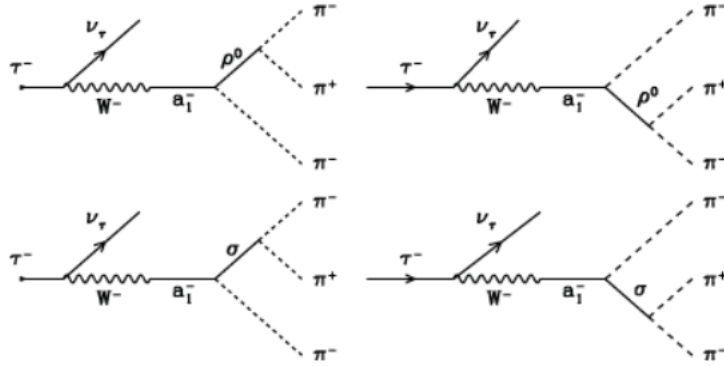


Figure 1.7: Feynman diagram of $\tau \rightarrow 3\pi\nu_\tau$ decay through a_1 resonance.

Their branching ratios [14] are listed in Table 1.1.

Decay	Branching ratio
$\tau^- \rightarrow e^- \bar{\nu}_e \nu_\tau$	$(17.83 \pm 0.04)\%$
$\tau^- \rightarrow \mu^- \bar{\nu}_\mu \nu_\tau$	$(17.41 \pm 0.04)\%$
$\tau^- \rightarrow \pi^- \nu_\tau$	$(10.83 \pm 0.06)\%$
$\tau^- \rightarrow \pi^- \pi^0 \nu_\tau$	$(25.52 \pm 0.09)\%$
$\tau^- \rightarrow \pi^- \pi^+ \pi^- \nu_\tau$	$(9.31 \pm 0.06)\%$
$\tau^- \rightarrow \pi^- 2\pi^0 \nu_\tau$	$(9.30 \pm 0.11)\%$

Table 1.1: Branching ratio of the main τ -decay modes.

Chapter 2

Belle II experiment

The Belle II experiment at the SuperKEKB accelerator represents the new generation of B-Factory, which is planning to collect an integrated luminosity of 50 ab^{-1} at $\Upsilon(4S)$ resonance, with the aim to refine several measurements in heavy flavour sector of Standard Model and searching for New Physics. Here the main features of the B-Factories and the motivation for the Belle II experiment are described, followed by a detailed description of the accelerator and the detector. The figures and the technical specifications are taken from the Belle II Technical Design Report [18].

2.1 B-Factory and physics motivations

In the $e^+ - e^-$ B-Factory [20], the B mesons are produced in pair from the decay of the $\Upsilon(4S)$, a strong resonance with mass $m_{\Upsilon(4S)} \simeq 10.58 \text{ GeV}/c^2$. The quark composition of $\Upsilon(4S)$ is $b\bar{b}$ and it's the lightest resonance with a mass sufficient to decay in b -flavoured mesons. The branching ratio in $B\bar{B}$ pair is about 96%. The two B mesons are produced in an entangled quantum state in the decay so that from the knowledge of the flavour of one B it's possible to assign the (opposite) flavour to the second B . The *flavour tagging* is performed reconstructing specific B decays correlated to the flavour of the decaying meson B_{tag} . If the signal decay $B \rightarrow f$ is reconstructed from the other tracks of the events, the initial flavour of the B_{sig} is known. The $\Upsilon(4S)$ is produced boosted with respect to the laboratory frame. In its frame the

$B\bar{B}$ pair is produced almost at rest ($m_{\Upsilon(4S)} - 2m_{B^0} \approx 19 \text{ MeV}$), thus in the laboratory frame the flight direction of both B is almost the same of the boost. After the decay and the reconstruction of the first B the decay vertex position z_1 is evaluated. The second B is reconstructed if it decays in the signal f . From the evaluation of the second vertex position z_2 it's possible to obtain $\delta z = z_2 - z_1$ and thus Δt . Without the boosted center of mass it would not be possible to obtain the time interval in which the two channels can interfere.

The main features of a B-Factory are summarized as follows:

- completely known initial state;
- boosted center of mass, with $\beta\gamma = 0.28$ at Belle II, necessary to increase the decay length of the $B\bar{B}$ pair at a measurable level;
- high luminosity, with $L \geq 8 \cdot 10^{35} \text{ cm}^{-2} \text{ s}^{-1}$ at SuperKEKB, in order to produce a large sample of $B\bar{B}$ pairs;
- high performance detector, with good vertex resolution to extrapolate the vertices position and an excellent particle identification capability to perform a high purity flavour tag.

The first generation of B-Factory has tested the CKM mechanism at the 10% level, but there are margins of NP to exists below this. In case LHC finds NP at the energy frontier, precision measurement are essential to further understand the discoveries or, in case LHC finds no evidence of NP, the B-Factories offer a unique way to probe for NP beyond TeV scale.

One of the main questions addressed to Belle II experiment is the investigation of Beyond Standard Model (BSM) sources of violation in quark sector: the SM CP violation is not sufficient to solve the baryon asymmetry and Belle, BaBar and LHCb measurements show several tensions with respect to SM expectation. With this purposes it is interesting to study time-dependent CP violation (TDCPV) in $b \rightarrow s$ transitions, in which the SM CP violation is expected to be very small, and an observation can be interpreted as a BSM signal. With the same purpose, CP violation in charm mixing can be investigated.

Another interesting sector in flavour physics is the searches for flavour-changing neutral currents (FCNC) beyond the SM: the FCNC are strongly suppressed by the GIM mechanism, thus the measurement is very sensitive to NP contributions. Approaches include TDCPV searches in neutral channels or transitions with large missing energy like $b \rightarrow s\nu\bar{\nu}$. In this classes of decays is crucial the vertex resolution and the neutral reconstruction capability of a B-Factory.

The cross section of $e^+e^- \rightarrow \tau^+\tau^-$ at B-Factory center-of-mass energy is similar to that of $B\bar{B}$, therefore the B-Factory results an effective τ -factory too. The lepton flavour violation (LFV) has been measured in neutrino mixing phenomena only, but the study of the τ physics allows to investigate BSM sources of LFV. The τ physics program includes CP violation measurement, electric dipole moment measurement and $(g-2)_\tau$ measurement too.

Despite the discovery of the SM Higgs, many extensions of Higgs sector are not excluded yet, and B decays with τ production ($B \rightarrow \tau\nu, B \rightarrow D^{(*)}\tau\nu$) offer a not trivial way to investigate this sector of possible NP. Currently this class of decays shows tensions with SM, and the B-Factory environment has the correct properties (in term of vertex resolution, missing mass identification, luminosity) to study the tauonic and semitauonic B decays. More in general, the decays which involve τ are challenging because of the large number of neutrinos involved, but accessible with Belle II experiment. The semileptonic B decays can be useful also to test the lepton universality.

The capability of a new generation of B-Factory to discover NP is not limited to the flavour sector. A B-Factory has a high sensitivity to dark matter via missing energy decays, i.e. via direct detection of new particles. Appropriate specific triggers can be developed for this purpose. In addition, the possibility to tune the center-of-mass of the collider on various strong resonance $\Upsilon(4S)$ allows studying a large family of quarkonia decays, to investigate low energy QCD with high level of precision. At last, a B-Factory with increased performance can measure with unprecedented precision the CKM observables increasing the knowledge of the SM.

2.2 SuperKEKB collider

SuperKEKB [22] is the upgrade of KEKB, in operations at KEK Laboratory in Tsukuba, Japan. The upgrade started in 2010 and has finished at the end of 2017. The principal motivation for this substantial upgrade was to increase the instantaneous luminosity of the machine from $2.1 \times 10^{34} \text{ cm}^{-2} \text{ s}^{-1}$ (KEKB) to $8 \times 10^{35} \text{ cm}^{-2} \text{ s}^{-1}$, to reach the statistic needed for the physics goals of the Belle II experimental program. This luminosity increase is obtained by using larger beam currents and by smaller beam dimension at the *interaction point* (IP), with the use of the nano-beam scheme, for which is crucial to keep the beam emittance (the phase-space volume of the bunch) as low as possible. The goal of SuperKEKB is to reach the full peak luminosity around 2022 and 50 ab^{-1} of integrated luminosity around 2025 (Figure 2.1).

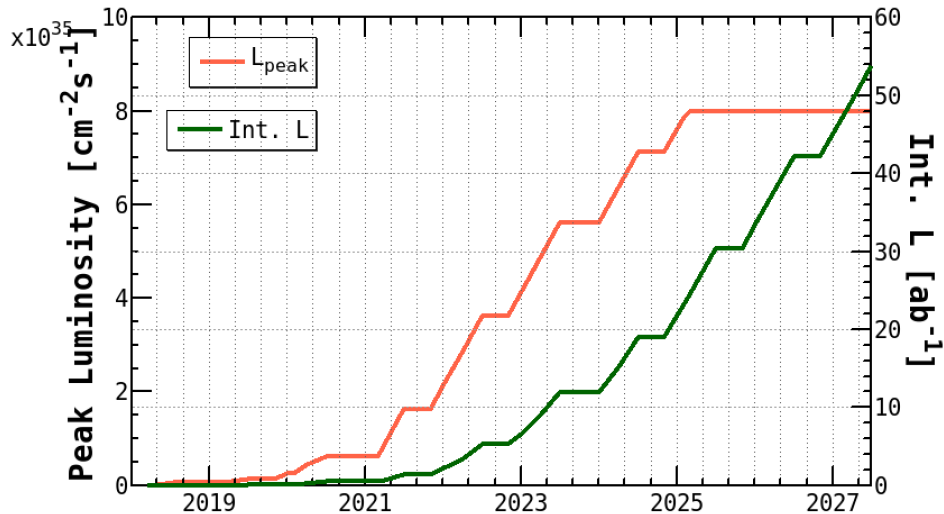


Figure 2.1: Goal of SuperKEKB and Belle II in terms of instantaneous and integrated luminosity.

SuperKEKB is an e^+e^- asymmetric collider with the bunched electron beam with an energy of 7 GeV and the positron beam with an energy of 4 GeV . The center-of-mass energy is $\sqrt{s} \simeq \sqrt{4E_+E_-} = 10.58 \text{ GeV}$. The electrons are produced in a pre-injector by a pulsed laser directed on a cold

cathode target, then they are accelerated by a linear accelerator (*Linac*) to 7 GeV and injected in the *High Energy Ring* (HER) of SuperKEKB. The positrons are produced by the collision of electrons with a tungsten target and then they are injected in a damping ring to reduce their emittance. When the positrons reach the required emittance they are accelerated to 4 GeV in the Linac and injected in *Low Energy Ring* (LER). The structure of the collider is reported in Figure 2.2.

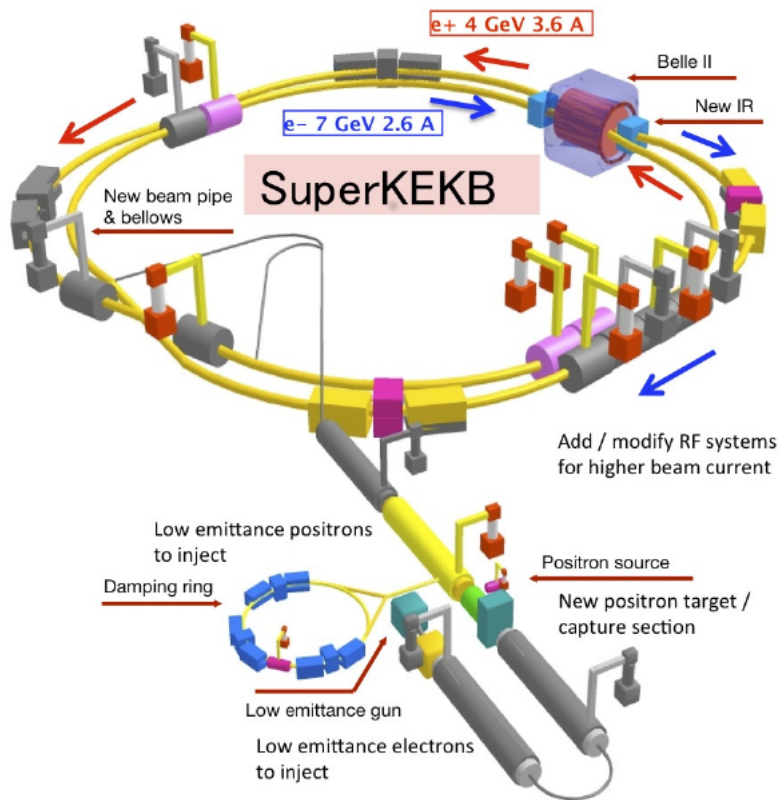


Figure 2.2: SuperKEKB collider structure.

The two beams collide at the IP with the particular nano-beams geometry intended to improve the luminosity of the collider. The beam asymmetry produces a Lorentz boost between the center-of-mass frame of the colliding

leptons and the detector rest frame (i.e. the laboratory frame) equal to:

$$\beta\gamma = \frac{|\vec{p}_{e^+} + \vec{p}_{e^-}| \cdot c}{\sqrt{s}/c^2} \simeq \frac{E_{e^-} - E_{e^+}}{\sqrt{4E_{e^+}E_{e^-}}} \simeq 0.28, \quad (2.1)$$

for a mean flight distance of the B mesons of $130 \mu m$. This distance is sufficient to track the vertices of the B mesons, but is reduced with respect to KEKB (it had a $\beta\gamma = 0.42$). This is due to the exponential increase of power absorption which set a limit to the energy of the HER. On the other hand the beam geometry at IP and bunch shape, that need a strongly reduced dispersion of the bunches, set a lower limit to the LER energy: to obtain the same $\beta\gamma$ of KEKB the energy of the LER should be reduced to $3.5 GeV$, but this implies higher beam losses due to Touschek scattering, not sustainable for the luminosity requirements. The luminosity requirement imposed several other modifications to the accelerator structure: the electron injection and positron target are modified, the damping ring, the radio-frequency system, the optics, the beam-pipe and the vacuum system are renewed. Some relevant collider parameters respect to those of KEKB are reported in Figure 2.3.

The data taking of the B-Factory is subdivided in three main phases:

1. Phase I (completed on February 2016): a preliminary phase without final focus and without collisions, used to evaluate beam background with a radiation detector only (Belle II detector was moved out of the beam line);
2. Phase II (completed on July 2018): run with the final focus, but at low luminosity to calibrate and tune the accelerator and the detector response. During Phase II the vertex detector of Belle II was not installed completely, but only a sector of VXD is present, to calibrate the detector and measure the radiation damage, thus the collected data lacks the full resolution vertex information;
3. Phase III (started on March 2019, currently ongoing): run with almost complete Belle II detector, with one of the two PXD layers missing (to be installed at the end of 2020), to perform the physics program of the collaboration. Most of the data are going to be collected at the $\Upsilon(4S)$ resonance.

		KEKB Achieved	SuperKEKB
Energy(GeV) (LER/HER)	E	3.5/8.0	4.0/7.0
Vertical Beta Function at IP(mm)	$\beta_y(IP)$	5.9/5.9	0.27/0.41
Beam-Beam Parameter	ξ_y	0.129/0.090	0.090/0.088
Horizontal Beamsize at IP(μm)	$\sigma_x(IP)$	10.2/11.2	10.2/7.75
Vertical Beamsize at IP(nm)	$\sigma_y(IP)$	48.3/61.8	59/59
Beam current (A)	I	1.64/1.19	3.60/2.62
Luminosity $10^{34} \text{cm}^{-2} \text{s}^{-1}$	L	2.11	80

Figure 2.3: SuperKEKB parameters respect to KEBB.

2.2.1 Nano-beams scheme

The nano-beams scheme has been designed to reduce the beam size at IP and so increase the luminosity [23]. The instantaneous luminosity of a collider is given by:

$$L = \frac{\gamma_{\pm}}{2er_e} \left(1 + \frac{\sigma_y^*}{\sigma_x^*}\right) \cdot \frac{I_{\pm} \xi_{y\pm}}{\beta_{y\pm}^*} \cdot \frac{R_L}{R_{\xi y}}, \quad (2.2)$$

where γ is the relativistic Lorentz factor, e is the absolute value of the electron charge, r_e is the classical radius of electron, $\sigma_{x,y}^*$ are the widths of the bunch at IP on the transversal plane, I is the current of the beam, β_y^* is the betatron function at IP (perturbation from the nominal trajectory), ξ_y is the vertical beam-beam parameter, R_L and $R_{\xi y}$ are the reduction factors of luminosity and the vertical beam-beam parameter due to not-vanishing crossing angle and the \pm sign is referred to the charge of the particles in the beam. The idea of the nano-beams is to strongly reduce β_y function with the minimization of the longitudinal size of the beam overlap at IP (Figure 2.4).

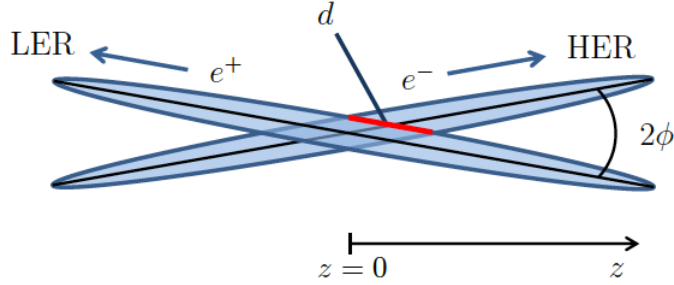


Figure 2.4: Geometry of the interaction point in the nano-beams scheme.

The dimension of the effective overlap region is $d \simeq \sigma_x^*/\phi$, where 2ϕ is the crossing angle of the beams. For that reason, the crossing angle has been chosen $2\phi = 83 \text{ mrad}$ (about four times KEKB crossing angle). In addition σ_y^* is reduced to the size of tens of nm to reach a beam size at IP of 50 nm (from $\sim 1 \mu\text{m}$ of KEKB). In conclusion with this scheme the β_y^* function is reduced by a factor 20 with respect of KEKB and since $\sigma_y^* \ll \sigma_x^*$, $R_L/R_{\xi y} \simeq 1$, $\xi_y^{\text{SuperKEKB}} \simeq \xi_y^{\text{KEKB}}$, the current of the beams must be doubled to reach the required luminosity.

2.2.2 Beam-induced background

A not negligible background produced by SuperKEKB beams is expected in the Belle II detector. This background is made of particles produced by several physical processes of beam-material or beam-beam interaction. The background yields have been partially measured during Phase I, and precise predictions are also based on simulated SuperKEKB data. The first background source is the Touschek effect, an intra-bunch Coulomb scattering process which deviates the particle energies from nominal values. The scattered particles propagate around the accelerating ring and finally are lost at the beam-pipe inner wall, producing a shower. That shower might produce signals in the detector. To mitigate this effect, collimators and metal shields are located in the final section of SuperKEKB close to the detector area. A second background source is the beam-gas scattering, i.e. the interaction between beam particles and residual gas molecules in the beam-pipe, with Coulomb scattering or bremsstrahlung. These interactions might

deviate the trajectories and energies from nominal values producing effects similar to Touschek. The countermeasures used for Touschek background are efficient also for beam-gas background. Another source of background are the photons from radiative Bhabha scattering, which interact with the SuperKEKB magnets iron producing neutrons by photo-nuclear resonance mechanism. In addition, a neutron shielding is placed along the ring and close to the detector. The last background source is the low momentum e^+e^- pairs produced by two-photon QED process $e^+e^- \rightarrow e^+e^-e^+e^-$, which might spiral inside the detector. An additional background source would be the synchrotron radiation of the beam (in particular the HER), which emits photons from few keV to tens of keV. However, the beam-pipe shape is designed to avoid synchrotron radiation photons pass through the detector. Moreover, the inner surface of beryllium beam-pipe is gold-plated to absorb scattered photons. These precautions should completely suppress the synchrotron radiation background.

2.3 Belle II detector

Belle II is the detector designed for SuperKEKB collider, and it is a substantial upgrade of the Belle detector. It's a general purpose experiment, optimized to $\Upsilon(4S) \rightarrow B\bar{B}$ events reconstruction, with the capability to perform efficient tracking of charged particles. In addition, there are a neutral particles identification system and a multi-detector Particle Identification system. Belle II integrates a high efficiency and low bias hardware and software trigger in order to cope the high background of the SuperKEKB events, made possible by a low track multiplicity and low detector occupancy combined with an efficient online reconstruction. In addition, the detector hermeticity and the knowledge of the initial state allow to perform missing mass analysis and use recoil techniques.

2.3.1 Detector overview

The structure of the detector (Figure 2.5) is as hermetic as possible with various sub-detector systems placed at various distances from the IP. The

following coordinate system is used: the origin is set at IP, $r \in [0, \infty]$ is the distance from IP on the transverse plane, $z \in [-\infty, \infty]$ the distance from IP on the longitudinal plane with positive values for forward region, $\phi \in [-\pi, \pi]$ is the azimuth angle where the 0 is set in the upward, $\theta \in [0, 2\pi]$ is the polar angle (0 is set to forward region). In some cases a Cartesian system is used, with z set along the electron beam axis in the forward direction, y upward and x in the right direction.

The detector has an approximate cylindrical symmetry around the z -axis, while it has a significant *forward-backward* asymmetry to improve the solid angle acceptance in the boost direction (forward direction is the boost direction from IP). From the innermost to the outermost sub-detector system Belle II is composed by:

- Pixel Detector (PXD): 2 layers of pixel detector (DEPFET technology) which provide 2-dimensional position information;
- Silicon Strip Detector (SVD): 4 layers of Double Sided Silicon Strip Detector which provide 2-dimensional information. It's used to the tracking tasks for online and offline reconstruction. The SVD and the PXD form the Vertex Detector (VXD) of Belle II;
- Central Drift Chamber (CDC): helium-ethane wire drift chamber, composed of 56 layers with stereo and longitudinal geometry, to obtain position information. It is used by trigger, tracking and particle ID tasks;
- Particle Identification System (TOP, ARICH): Time-Of-Propagation counter for barrel region with a Čerenkov quartz radiator, and Ring-Imaging Čerenkov Detector, with an aerogel radiator for end-caps regions;
- Electromagnetic Calorimeter (ECL): homogeneous calorimeter composed of CsI(Tl) Crystals that provide $16.1 X_0$. It's used to measure the energy of photons and energy deposits from charged particles for particle identification;

- Superconducting coil: NbTi/Cu coil that provides a uniform magnetic field of 1.5 T parallel to the beam direction in the internal region. The iron structure of the KLM detector is used to return yoke of the field;
- K_L and μ system (KLM): alternated layers of Resistive Plate Chambers and iron plates in barrel regions and scintillator strips in end-cap region. It provides 3.9 interaction length in the barrel region and it is used to detect μ and K_L that escape from internal region.

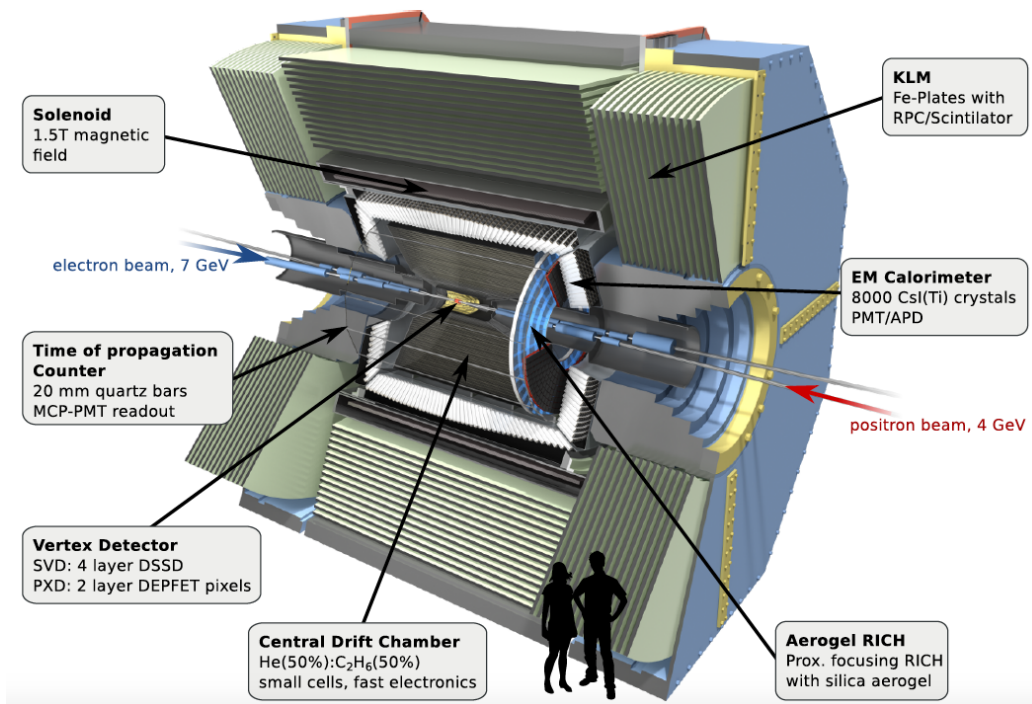


Figure 2.5: Structure of Belle II detector.

2.3.2 Vertex Detector

The Vertex Detector (VXD) is the innermost sub-detector of Belle II. It is composed by two devices, the silicon Pixel Detector (PXD) and the Silicon Vertex Detector (SVD), forming a 6-layer silicon vertex detector.

The PXD (Figure 2.6) is composed of two layers of pixelated sensors with DEPFET technology. The layers are placed at 14 mm and 22 mm from

IP while the beam-pipe radius is about 10 mm . The pixelated sensors have been chosen to sustain the higher hit rate (where a hit is the signal of a detector which return position information) due to the shorter distance from IP and the higher luminosity with respect to Belle. This solution allows keeping the occupancy of the detector, defined as the number of activated pixels in the same time over the total number of pixels, at about 3%. The amount of data provided from the PXD in a single event is higher than the accepted Data Acquisition (DAQ) rate, therefore SVD+CDC-only tracks are reconstructed online and extrapolated onto the PXD sensors during the High Level Trigger (HLT) process. This extrapolation determines some Regions Of Interest (ROI) from which the PXD hits are selected for readout, allowing the system to remain within the DAQ bandwidth.

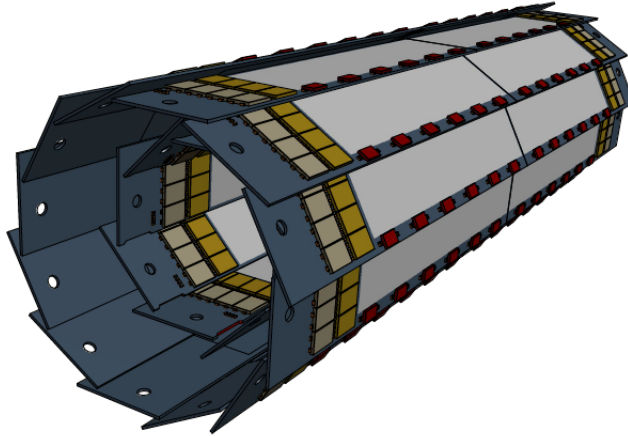


Figure 2.6: View of Silicon Pixel Detector.

The SVD (Figure 2.7) is composed of four layers of Double Sided Silicon Strip Detector, placed at 38 mm , 80 mm , 115 mm , and 140 mm from IP. SVD uses several types of sensors with different shapes and strip pitch. It employs a slanted geometry for the forward sensors to increase the acceptance. An original feature of the SVD is the Origami chip-on-sensor concept, i.e. an innovative solution that uses a flexible fan-out to put all the readout chips on the same side of the modules in the detection region to reduce the

connections and simplify the cooling system.

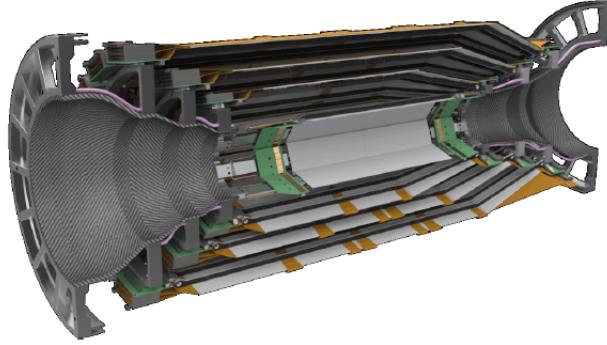


Figure 2.7: View of Silicon Vertex Detector.

2.3.3 Central Drift Chamber

The Central Drift Chamber (CDC) is a wire drift chamber with three main functions in Belle II:

1. it's the main tracking device to precisely measure momenta;
2. it provides particle identification (PID) information by measuring energy loss in gas volume;
3. it's used in hardware and software charged particles trigger.

The chamber is composed of 8 super-layers formed by 6 layers of wires each, and an innermost super-layer formed by 8 layers of wires. The chamber is filled with a mixture of Helium and Ethane (50% He , 50% C_2H_6), and the entire CDC is closed by 2 carbon cylinder and 2 aluminum endplates. There are two classes of wires: the field wires producing the accelerating electric field and the sense wires collecting the released charge. The field wires are composed of aluminum and are thicker ($126 \mu m$ of diameter) than the sense wires, which are made of gold-plated tungsten and have a diameter of $30 \mu m$. The radial cell size is $10 mm$ for the innermost super-layer and $18.2 mm$ for the other super-layers. When a charged particle crosses the CDC ionize the gas mixture of the chamber producing e^- . The electrons are accelerated by

the electric field and produce a charge avalanche that induces a signal on the sense wires, from which is possible to reconstruct the drift time and thus the initial particle position. The front-end electronics is located near the backward endplate, and it uses a chip to amplify, shape and discriminate the signal. A TDC is used to measure the drift time and a FADC to measure the signal charge. To obtain z position information from the CDC half of the super-layers have a *stereo* wire configuration. It means that the wires are not strictly parallel to z -axis but present a small angle on $r - \phi$ plane. With the use of different inclinations it is possible to reconstruct the 3D position. The innermost radius of CDC is 160 mm , larger than the Belle one (77 mm), because the higher expected background rates would make the chamber unusable at smaller radius. A complex endplate geometry is employed to ensure good angular converge while limiting occupancy, especially from Bhabha scattering in the forward direction. The outermost radius is 1130 mm , larger than Belle one (880 mm) because the PID barrel device of Belle II is more compact than in Belle. The angular acceptance is the same of VXD to be able to merge all the tracks of two sub-detectors. The position resolution of CDC is about $100\ \mu\text{m}$, while the dE/dx resolution is about 11.9% for particles with $\theta \simeq \pi/2$.

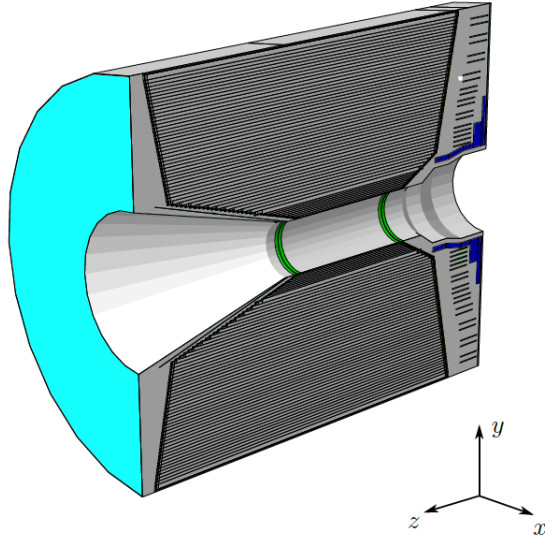


Figure 2.8: View of Central Drift Chamber.

2.3.4 TOP and ARICH

The main devices for particle identification in Belle II located outside the CDC are the Time of Propagation Counter (TOP) in the barrel region and the Aerogel Ring-Imaging Čerenkov counter (ARICH) in the forward end-cap region. Both systems detect Čerenkov light, but the operating principles are substantially different. Čerenkov detectors measure the θ_c angle of photons emitted by relativistic charged particles crossing a radiator material, obtaining β of the particle with the relation: $\cos\theta_c = (\beta n)^{-1}$, where n is the refractive index of the material. In Belle II, using the independent momentum measurement in the tracking system and the measurement of β combined to the energy loss measured in the CDC the mass of the particles is determined.

The structure of the TOP is shown in Figure 2.9: a single TOP module is made of a quartz bar with a focusing mirror in the forward region and an array of Photomultipliers (PMT) in the backward region. The operating principle of the TOP detector is to obtain θ_c from the measurement of the time of arrival of Čerenkov γ 's from the emission point as a function of the angle of the Čerenkov cone Φ on the plane of the bar. From the combined information of the arrival time t_{TOP} , Φ and position and direction of the main particle provided from tracking it's possible to extract the θ_c information. In the TOP detector the emitted photons are reflected internally in the quartz bar and reach the focusing mirror in the forward region. The mirror is built to preserve the Φ angle information and to reflect the photons to a specific PMT channel that measures the t_{TOP} . Thus the Φ angle is evaluated depending on the PMT activated channel. The photons emitted in the backward directions are first reflected by a mirror at the end of the quartz bar and directed to the focusing mirror. The entire TOP detector is made of 16 modules set around the CDC at 1.2 meter of radius from IP, with an angular acceptance of $\theta \in [31^\circ, 128^\circ]$. The bar quartz dimension is $0.45\text{ m} \times 2\text{ cm} \times 2.75\text{ m}$. The TOP has a single photon time resolution of about 100 ps , achieved with 16 channel micro-channel plate (MCP) PMTs. Instead the production time of the main particle is known with the precision of about 50 ps .

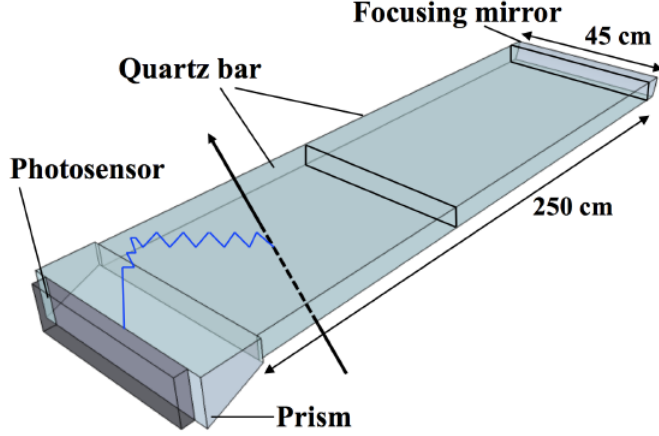


Figure 2.9: Scheme of a single module of Time of Propagation Counter.

The ARICH (Figure 2.10) is a proximity focusing Ring-Imaging detector, which uses as radiator a ring of aerogel. An expansion volume of 20 cm divides the radiator from a ring of hybrid avalanche photon detectors (HAPD), and allows the Čerenkov photons to enlarge into rings. The performance of RICH detectors depends on the number of detected photons N_γ and the single photon resolution on the Čerenkov angle σ_{θ_c} . N_γ increases with the thickness of the radiator and the resolution per track improves as $\sigma_{\theta_c}/\sqrt{N_\gamma}$, but σ_{θ_c} degrades due to the uncertainty of the emission point. In the Belle II ARICH a peculiar solution is adopted to optimize the performance: two layers of aerogel with different refractive indices ($n = 1.045$ upstream, $n = 1.055$ downstream) and 2 cm thickness are used, so that the two produced rings are overlapped on the detection surface, giving the N_γ equivalent to a double radiator thickness. The reached resolution is $\sigma_{\theta_c} \simeq 13\text{ mrad}$, optimized for charged tracks with momentum larger than $3.5\text{ GeV}/c$, but the σ_{θ_c} doesn't show significant degradation also for lower momentum tracks. With $N_\gamma \simeq 10$ per ring, the resolution of a single track is about $\sigma_{\theta_c}^{track} \simeq 3\text{ mrad}$. The angular acceptance is $\theta \in [14^\circ, 30^\circ]$.

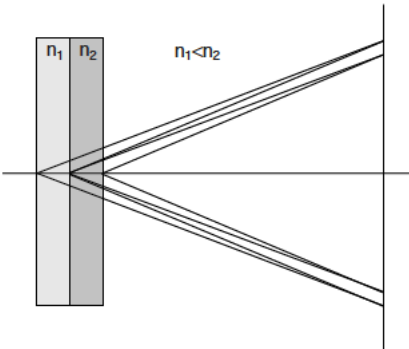


Figure 2.10: Scheme of Aerogel Ring-Imaging Čerenkov counter structure.

2.3.5 Electromagnetic Calorimeter

The Electromagnetic Calorimeter (ECL) has several central roles in Belle II. First, it detects photons with high efficiency and measures their energy and angle. Secondly, it identifies electrons and contributes to the K_L^0 detection with KLM sub-detector. Third, it generates a hardware and software photon trigger. In addition, the ECL is used to monitor online and offline the luminosity of SuperKEKB. The Belle II ECL uses the same crystals of Belle's calorimeter, but a complete upgrade of the readout electronics was needed in order to cope the SuperKEKB increased luminosity. The calorimeter is subdivided into three regions: the barrel region, the forward end-cap and the backward end-cap regions. They collectively cover 90% of the solid angle in the center-of-mass system (with an angular acceptance of $\theta \in [12.01^\circ, 155.03^\circ]$). The barrel region is extended for 3 meters and has an inner radius of 1.25 m. The annular end-cap regions have the internal base at $z = 1.96$ m (forward) and $z = -1.02$ m (backward) from IP. There are two gaps of 1° between the barrel and the end-caps regions to allow the passage of the cables of internal sub-detectors. The ECL is a homogeneous highly segmented calorimeter, composed by 8736 crystals of CSI(Tl) (cesium iodide thallium-doped). The crystals have a shape of a truncated pyramid with a length of 30 cm and a 6×6 cm² base, equivalent to 16.1 radiation lengths (X_0). The crystals are assembled in 8 cells separated by 0.5 mm thick aluminum septum walls

and closed by two cylinders. Each cell provides the optimal operating environment for the crystals in term of humidity and temperature by a dry air flushing and a water cooling system. At the external bases of the crystals $10 \times 20 \text{ mm}^2$ photodiodes (Hamamatsu Photonics s2744-08) are glued with a 1 mm plexiglass plate collecting light from the scintillating material. Each photodiode has a LED to inject light pulses into the crystal volume to monitor the optical stability. The relatively long decay time of scintillations in CsI(T) ($1 \mu\text{s}$), in the presence of elevated background level expected in Belle II, produces a not negligible overlapping of pulses from neighboring background events. Therefore the new readout electronics samples the photodiodes signals in 16 points and then fits the signal shape with a predefined proper function. The energy resolution of ECL is given by:

$$\frac{\sigma_E}{E} = \sqrt{\left(\frac{0.066\%}{E}\right)^2 + \left(\frac{0.81\%}{E^{1/4}}\right)^2 + (1.34\%)^2} \quad (2.3)$$

where E is the energy in GeV. For example it means σ_E/E (100 MeV) $\simeq 2\%$ and σ_E/E (4 GeV) $\simeq 1.4\%$. In Belle the angular resolution of ECL is $\sigma_\theta \simeq 13 \text{ mrad}$ at low energy and $\sigma_\theta \simeq 3 \text{ mrad}$ at high energies, while the π^0 mass resolution is $4.5 \text{ MeV}/c^2$. Despite the higher background level, because of the new electronics, the performances are expected to be similar in Belle II.

2.3.6 Magnet

A superconducting coil produces a 1.5 T homogeneous \vec{B} field parallel to the beam direction. The coil is made of NbTi/Cu, and the internal volume is a cylinder of $2r = 3.4 \text{ m}$ and a length of 4.4 m . It operates with a 4400 A current and a liquid helium cryogenic system. The iron structure of KLM provides the return yoke of the magnetic field, therefore in the region of KLM outside the coil the direction of \vec{B} (i.e. the curvature of the tracks) is inverted.

2.3.7 Neutral kaons and muons system

The neutral kaons and muons system (KLM) is located outside the superconducting coil and it's build by alternating iron plates and active material detectors. The barrel region covers the polar angle range from $\theta = 45^\circ$ to $\theta = 125^\circ$, and the end-caps extend the range from $\theta = 20^\circ$ to $\theta = 155^\circ$. In the barrel region there are 15 detector layers and 15 iron plates, while in each end-cap are present 14 detector layers and 14 iron plates. The iron plates are 4.7 cm thick each and serve as the magnetic flux return for the superconducting solenoid and providing 3.9 interaction lengths (λ_0) in addition to the 0.8 λ_0 of the ECL, in which K_L can shower hadronically. The task of the KLM detector is to identify the muon tracks by measuring their penetration depth in the iron and to reconstruct neutral long-lived kaons with the use of the combined information of ECL and the hadronic KLM showers. The barrel detector layers of KLM are Resistive Plate Chambers (RPC): a proportional gas chamber used in streamer mode with a dielectric plate between the electrodes to prevent the propagation of sparks and so increase the spatial resolution. The signal is read with metallic strips on one side of the chamber. Each KLM module is made of two coupled RPC, with independent power supply and orthogonal strips configuration (this pair of RPC is called *super-layer*). Both the detector layer and the iron structure of the barrel region are exactly the same one used in Belle experiment, because the events rate results sustainable despite the increased luminosity. Instead, in the end-caps region and in the innermost barrel super-layer of the KLM, the RPCs have been replaced by two orthogonal layers of scintillator strips coupled with silicon photomultiplier (SiPM), because the RPCs have a too long dead time to sustain the background rate of this region. The muons are identified starting from CDC tracks: each track is extrapolated to KLM region with a π mass hypothesis, and if a KLM hit is present near the extrapolation region it's assigned to that track. The muon detection efficiency plateaus at 89% above 1 GeV/c with a hadron fake rate of about 1.3% mostly due to pions that decay in flight in softer muons. To reconstructs K_L^0 all the KLM hits within a 5° opening angle cone from IP are clustered, then a charged track veto is applied with the use of a CDC track matching. If the remaining neutral KLM clusters are aligned within a cone of 15° with an ECL cluster the two

showers are associated. The K_L^0 detection efficiency rises linearly from 0 at $0 \text{ GeV}/c$ to a 80% plateau at $3 \text{ GeV}/c$. The angular resolution is about 3° for KLM-only candidates and 1.5° for KLM+ECL candidates. The SiPMs offer an excellent time resolution of $\sigma_t \simeq 0.7 \text{ ns}$, that allows to measure also the time of flight of K_L^0 .

2.3.8 Trigger

The bunch crossing frequency of SuperKEKB is about 250 MHz . Since the bunch crossing time of 4 ns is much faster than the detectors signal collection time for all practical purposes the beam can be considered continuous. Anyway, at full luminosity, the expected event rate is about 50 kHz , and over than 90% of these events are Bhabha scattering or 2γ QED processes. A trigger system is therefore required to select events from beam background and identify interesting ones. Despite $B\bar{B}$ events are characterized by a higher charged track multiplicity with respect to others events, this variable can not be used in the trigger because τ and low multiplicity events would be discarded too. The required trigger must have instead an efficiency close to 100% for $B\bar{B}$ events and a high efficiency for τ and low multiplicity events too. Some efficiency degradations are allowed to suppress the Bhabha and 2γ QED backgrounds. The trigger rate must be below 30 kHz , the maximum acquisition frequency of DAQ, and the trigger must provide time information with a precision below 10 ns to exploit the potential of the Belle II sub-detectors. To cope with the high background and to the several physics scenarios the trigger system must be robust and flexible. The Belle II trigger is subdivided in two main stages: a hardware trigger or *Level 1 trigger* (L1) and a software trigger or *High Level Trigger* (HLT). The first one removes most of the background events with the use of raw information from the faster sub-detectors with an output trigger rate of 30 kHz , while the second one refine the selection with a more exhaustive analysis and reduce the event rate from L1 trigger to a storable rate of 10 kHz .

Chapter 3

A preliminary look at Phase II data with $\tau^+ - \tau^-$ sample

The aim of the work described in this chapter is to analyze the τ -pairs produced by e^+e^- collisions in the *SuperKEKB* accelerator, selecting the events from channels $\tau^\pm \rightarrow 3h^\pm(n\pi^0)\nu_\tau$ (3-prong decays) and $\tau^\pm \rightarrow h^\pm(n\pi^0)\nu_\tau$, $\tau^\pm \rightarrow \mu^\pm\bar{\nu}_\mu\nu_\tau$ and $\tau^\pm \rightarrow e^\pm\bar{\nu}_e\nu_\tau$ (1-prong decays), where $h^\pm = \pi^\pm, K^\pm$. The process $e^+e^- \rightarrow \tau^+\tau^-$ has a cross section $\sigma(e^+e^- \rightarrow \tau^+\tau^-) = 0.92 \text{ nb}$. The BELLE II analysis framework, *BASF2*, is exploited to process real data (*Data*) and to generate MonteCarlo (*MC*) simulation samples. They are analyzed by means of ROOT, used as the main analysis framework.

The analysis shown here is of explorative type. After an initial skimming phase and then a signal selection, the distributions of the main variables (useful to distinguish the signal from the background contributions) are compared to evaluate the agreement between experimental data and MC simulation. In this way it is possible to identify defects in modeling by simulation of the apparatus response, to study the systematic effects and possibly extract corrections. Finally, a data-driven technique is developed to obtain a separation of electron and muon candidates based on the ratio between the energy released in the electromagnetic calorimeter and the momentum of the track measured by the drift chamber in order to easily count electrons and muons in a certain phase space region.

3.1 Overview on BASF2

The raw data coming from the detector are calibrated, reconstructed and stored on tape using PANTHER based data summary tape (DST) files [26]. PANTHER is a custom serialization format. After each experiment the calibration constants are recomputed and stored in the Belle Condition Database. Finally, the data are reprocessed and stored in a compact form called mDST files, a reduced and compressed form of the data summary files in ROOT format [25, 27]. The reconstruction and the processing of the mDST files is handled by the Belle II AnalySis Framework (BASF2). Different types of events are simulated (using the EvtGen and GEANT4 [24] packages) and reconstructed.

The same software framework is used in online data taking and offline reconstruction, Monte Carlo production, and physics analysis. After calibration parameters are determined, the raw data are reconstructed and stored at the KEK computing center. Monte Carlo production and reconstruction data files are distributed to data centers around the world. The reconstructed informations are stored in ROOT-based mDST or uDST files (i.e. only condensed high-level objects, no hits or raw data, plus selected high level analysis objects).

Various levels of data processing can be distinguished:

- online reconstruction: read-out of the detector and the trigger system, producing the raw-data (DST files);
- offline reconstruction: cluster reconstruction, track finding and fitting, producing the mDST data;
- mDST analysis: creation of final state particle hypotheses, reconstruction of intermediate particle candidates and vertex fitting, producing flat Ntuples (in ROOT format);
- Ntuples analysis.

Figure 3.1 briefly schematizes the structure of these processing steps.

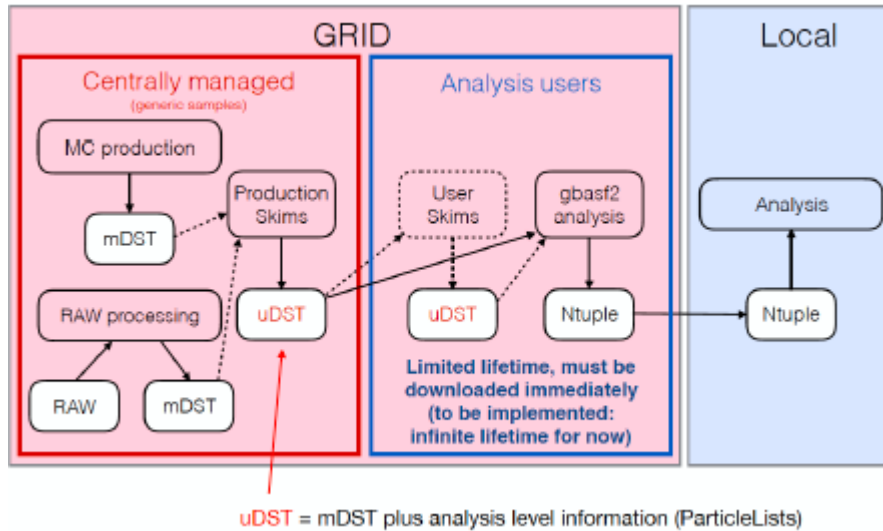


Figure 3.1: Schematization of processes that conduct from raw data to analyzable data.

The framework is written in C++11 and Python 2.7 plus additional third-part libraries (i.e. EvtGen, GEANT4, ROOT). BASF2 is divided into packages, each of them covering a different aspect of data processing: data acquisition, MonteCarlo event generation, detector and sub-detector simulation, track reconstruction, visualization of individual events inside the detector, physics analysis. The packages contain libraries, modules and data-objects. The libraries are implemented in C++ and they provide functionality shared between different modules. The modules are small processing blocks built on top of the libraries and they operate on data event by event performing self-contained tasks. A chain of modules represents a path. The informations shared between modules are encoded in data-objects. They are stored in a common DataStore, which every module can read and write. Typical examples for data-objects are *Track*, *ECLCluster*, *Particle* and *ParticleList* objects. To use BASF2 the user has to provide a steering file written in Python. In this file the path is created and filled with modules, then it is processed. BASF2 architecture is shown in Figure 3.2.

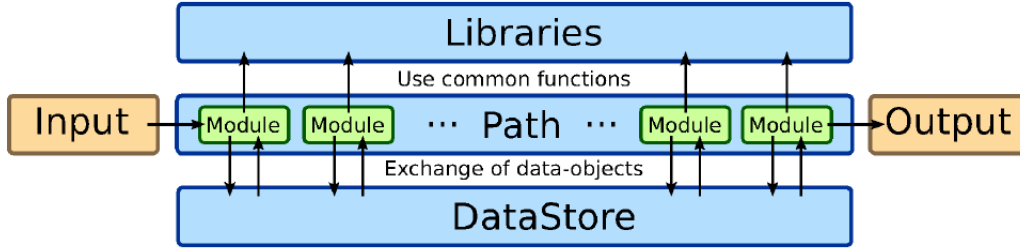


Figure 3.2: BASF2 architecture.

3.2 Preselection on data sample

The data were collected with Belle II detector during *Phase II*, in which the inner layers of the silicon-based VXD tracking system were missing.

In this analysis the processed *prod6* data from Experiment 3 are used with bad runs excluded in accordance with the official selection (informations described in Figure 3.3). The Basf2 release is 02-01-00/GT438. More informations are displayed in the web site.

run range	offline luminosity (bhabha)	offline luminosity (gamma gamma)	offline luminosity	Comments
0-5613	479.8 pb ⁻¹ ★	494.9 pb ⁻¹	pb ⁻¹	bad runs for TOP from 2824 to 3547 (so ~135 pb ⁻¹).

Figure 3.3: Offline luminosity and run range of prod6 data sample.

The MonteCarlo production (11th campaign) considered, with a beam background taken from events with random trigger on data, corresponds to an integrated luminosity equivalent to 1 fb⁻¹. This MC file is *generic*, infact it contains signal events (3 × 1 decays) and several types of background contributions:

- τ -pair;
- *mixed* ($B^0 - \bar{B}^0$);
- *charged* ($B^+ - B^-$);

- *continuum* ($u\bar{u}$, $d\bar{d}$, $s\bar{s}$, $c\bar{c}$).

The Python steering file used to generate the Ntuples is structured as follow. The first step is to fill the particle lists (including their charged conjugated particles) :

- *stdPi*("all"), i.e. pions;
- *stdEl*("all"), i.e. electrons;
- *stdMu*("all"), i.e. muons;
- *stdPhotons*("all"), i.e. photons;
- *stdKshorts*(), i.e. short kaons.

There are preliminary requirements to apply on charged tracks (reconstructed by the CDC hits) and photons (from physics events and machine background), as follows:

- $p_t > 0.2 \text{ GeV}/c$ (transverse momentum), for tracks;
- $|d_0| < 2 \text{ cm}$, $|z_0| < 4 \text{ cm}$ (impact parameters), for tracks;
- $clusterNhits > 1.5$ (number of weighted crystals in the ECL cluster) and $clusterE9E21 > 0.9$ (ratio of the energy between the inner - 3x3 - and outer - 5x5 minus 4 corners - cells of the cluster) and $-0.8660 < \cos\theta < 0.9563$ (CDC acceptance), for calorimetric objects.

In the $e^+e^- \rightarrow \tau^+\tau^-$ centre-of-mass system (CMS), both τ leptons are boosted and their decay products are well separated in two opposite hemispheres defined by the plane perpendicular to the *thrust axis* [21]. The thrust axis \hat{n}_{thrust} is defined such as the direction that maximizes

$$V_{thrust} = \sum_i \frac{|\vec{p}_i^{cm} \cdot \hat{n}_{thrust}|}{\sum_i \vec{p}_i^{cm}}, \quad (3.1)$$

where \vec{p}_i^{cm} is the momentum of each charged particle and photon in the CMS. Defining θ_{thrust} the angle between the track momentum and the thrust axis, the vector \hat{n}_{thrust} divide the detector volume into two event-dependent hemispheres:

- S_1 , in which $\cos\theta_{thrust} > 0$;
- S_2 , in which $\cos\theta_{thrust} < 0$.

One of these hemispheres is expected to contain the products of 3-prong decay (*3-prong side*), while the opposite is expected to contain one charged particle, i.e. the product of 1-prong decay, being either a lepton - e , μ - or a hadron (a number of additional photons and π^0 s are expected for example from $\tau^\pm \rightarrow \rho^\pm \nu_\tau \rightarrow \pi^\pm \pi^0 \nu_\tau$). There is also one neutrino on the 3-prong side and one or two neutrinos in the 1-prong side. This causes a certain missing energy and missing momentum in each event. The candidate events are selected by requiring the following skims (established by *Tau-group* in Belle II) to apply on the above particle lists:

- $1 < nGoodTracks < 7$, where *goodtrack* refers to tracks that satisfy:
 - $|dz| < 0.5cm$, $|dr| < 3.0cm$, $|d_0| < 2cm$, $|z_0| < 4cm$, $nCDCHits > 0$ (number of hits in the CDC), $p_t > 0.2 GeV/c$, $-0.8660 < \cos\theta < 0.9563$.
- $-2 < \Delta Q < 2$, where ΔQ is the charge imbalance;
- $p_{miss} > 0.4 GeV/c$ and $0.0873 rad < \theta_{p_{miss}} < 2.6180 rad$, where p_{miss} is the missing momentum of event (calculated by all the momenta of reconstructed tracks) and $\theta_{p_{miss}}$ the angle between this vector and the beam axis;
- $M_{miss}^2 < 72.25 GeV^2/c^4$, where M_{miss}^2 is the missing mass squared of event defined as

$$M_{miss}^2 = \left(E_{\Upsilon(4S)} - \sum_{n=1}^{N_t} E_n \right)^2 - \sum_{n=1}^{N_t} |p_n|^2 \quad (3.2)$$

where $E_{\Upsilon(4S)}$ is the energy of $\Upsilon(4S)$ and E_n and p_n are the energy and momentum of particle n respectively;

- $E_{tot} < 9.0 GeV$, where E_{tot} is the total energy of event in the laboratory system;

- $[nTrackS_1 = 1 \text{ or } 3 \text{ with } M_{inv}^{S_1} < 1.8 \text{ GeV}/c^2 \text{ and } E_{S_1} < 5 \text{ GeV}]$ or $[nTrackS_2 = 1 \text{ or } 3 \text{ with } M_{inv}^{S_2} < 1.8 \text{ GeV}/c^2 \text{ and } E_{S_2} < 5 \text{ GeV}]$, where M_{inv}^S is the invariant mass of the three charged pions and E_S the total energy in the S hemisphere;
- 4 charged tracks in the event with zero net charge.

In particular, the last two conditions guarantee that if in the S_1 hemisphere there are three charged tracks then in S_2 there is only the fourth track with opposite sign of $\cos\theta_{thrust}$, and viceversa. After imposing these selection criteria, the MonteCarlo *truth-matching* and a list of variables of interest are implemented, then the uDST files are processed and finally the data and MC Ntuples are generated.

3.3 Signal selection

In the following, the label $_0_i$, with $i = 0, 1, 2$, indicates the i -th daughter of $\tau \rightarrow 3 - prong + \nu_\tau$ (i.e. the three charged pions), while $_1_0$ indicates the single charged track of $\tau \rightarrow 1 - prong + \nu_\tau$ (i.e. electron, muon or pion). As an initial condition, the reconstructed tracks are required to be associated to clusters in the ECL ($E_{0_0}, E_{0_1}, E_{0_2}, E_{1_0} > 0$). The candidate events are selected according to an event topology consistent with one (1-prong) against three charged tracks (3-prong). This is done by requiring that:

- $[\cos\theta_{thrust_0_0} > 0, \cos\theta_{thrust_0_1} > 0, \cos\theta_{thrust_0_2} > 0, \cos\theta_{thrust_1_0} < 0]$ and $[\cos\theta_{thrust_0_0} < 0, \cos\theta_{thrust_0_1} < 0, \cos\theta_{thrust_0_2} < 0, \cos\theta_{thrust_1_0} > 0]$.

In order to suppress the background processes satisfying the selection criteria and faking the $\tau^+ - \tau^-$ signal (listed in Table 3.1 with the corresponding cross sections), it is necessary to find one or more discriminant variables, whose shapes permit separation of signal and background, on which to apply cuts.

Processes	Cross section [nb]
$e^+e^- \rightarrow u\bar{u}$	1.61
$e^+e^- \rightarrow d\bar{d}$	0.4
$e^+e^- \rightarrow s\bar{s}$	0.38
$e^+e^- \rightarrow c\bar{c}$	1.3
$e^+e^- \rightarrow B\bar{B}$	1.05

Table 3.1: Background processes with corresponding cross sections at $\sqrt{s} = m_{\Upsilon(4S)}$.

At this point of the selection, the simulated MC sample contains 100441 total events (N_{tot}), splitted in 53708 true background events (N_{bkg}) and in 46703 true signal events (N_{sig}). As seen in Table 3.1, the main sources of background are the continuum events (i.e. $e^+e^- \rightarrow q\bar{q}$, where $q = u, d, s, c$) and the mixed-charged events from $B\bar{B}$ pairs (i.e. $e^+e^- \rightarrow \Upsilon(4S) \rightarrow B^+B^-, B^0\bar{B}^0$). There are 46058 continuum events ($N_{continuum}$) and 7650 mixed-charged events ($N_{B\bar{B}}$). A further cut is imposed on the visible energy in the CMS (defined as the sum of clusters energy and charged tracks energy in the event) and to take into account another condition on data trigger that it is not preimposed on the MC uDST files before the skimming phase:

- $E_{vis}^{CMS} < 8.4 \text{ GeV}$.

The best discriminant variable results to be:

$$\left| \sum_{i=0}^2 \cos\theta_{thrust_0_i} \right|,$$

whose distribution is reported in Figure 3.4. Also $\left| \cos\theta_{thrust_1_0} \right|$ has been considered (Figure 3.5).

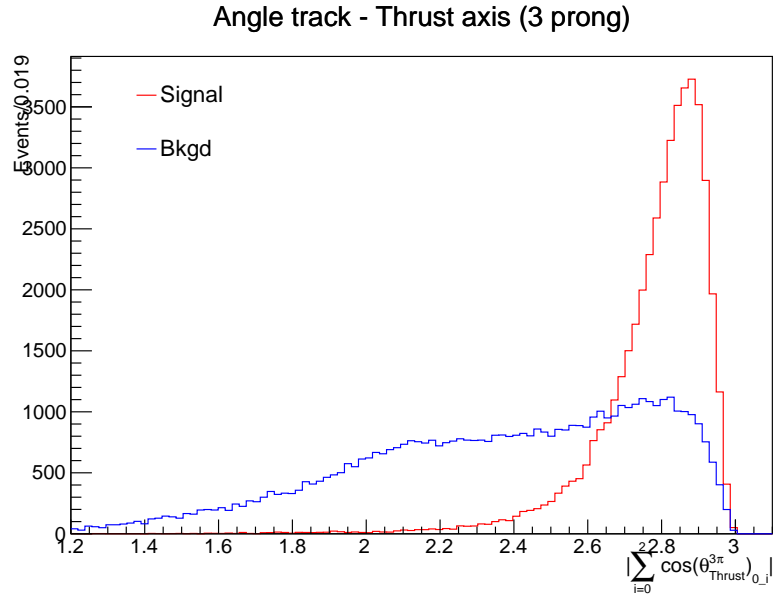


Figure 3.4: $|\sum_{i=0}^2 \cos\theta_{Thrust_0_i}|$ distribution of charged tracks on 3-prong side.

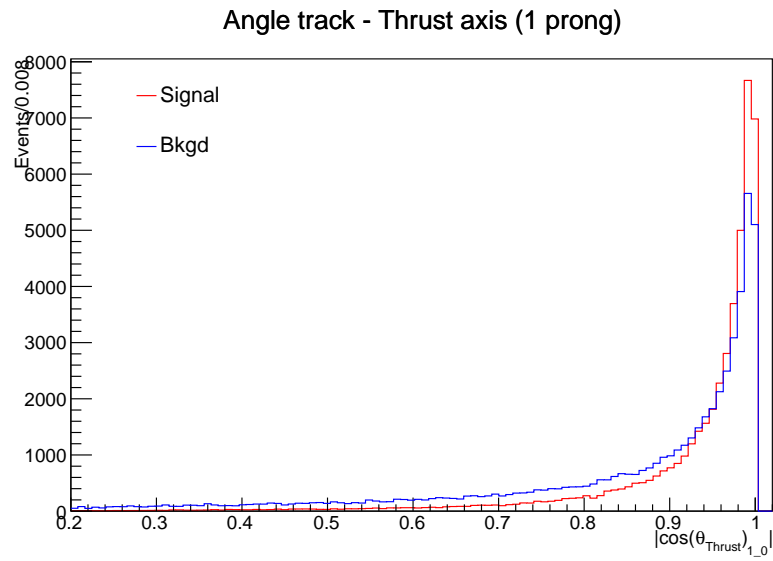
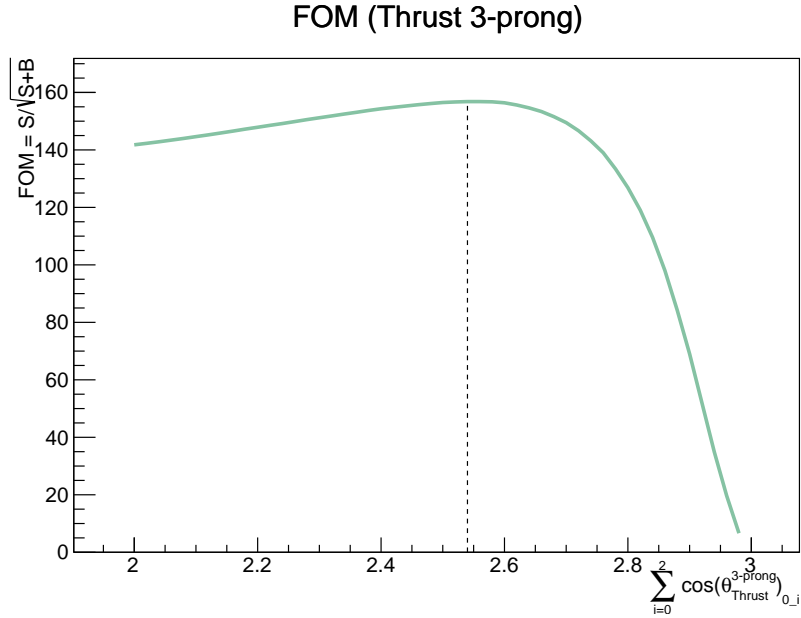


Figure 3.5: $|\cos\theta_{Thrust_1_0}|$ distribution of charged track on 1-prong side.

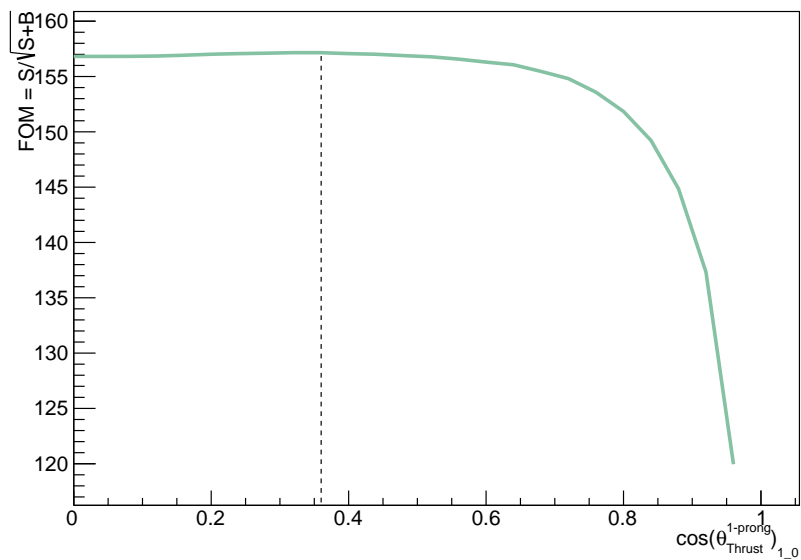
As shown in the histogram in Figure 3.4, the τ signal particles ($3 \pi^\pm$) do not deviate much from the primary τ -trajectory (and so from the thrust axis), while particles arising from background events have more spherical and flat $\cos\theta_{thrust}^{3-prong}$ distribution. Therefore, to optimize a requirement on these two variables the following figure of merit (FOM) has been optimized:

$$FOM = \frac{S}{\sqrt{(S+B)}}, \quad (3.3)$$

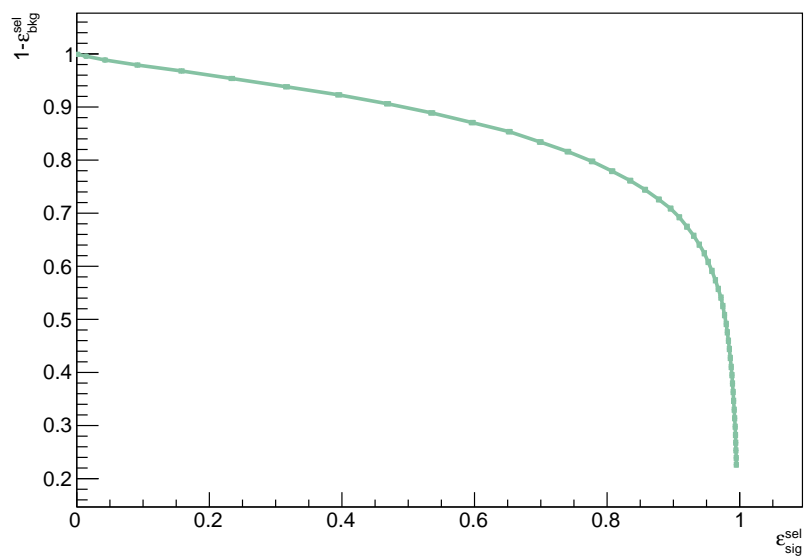
where S is the number of signal events and B the number of total background events. For each step of the selection FOM, *signal selection efficiency* (ϵ_{sel}^{sig} , i.e. number of signal events passing the selection respect to initial number of signal events) *background rejection power* ($\mu_{rej}^{bkg} = 1 - \epsilon_{sel}^{bkg}$, where ϵ_{sel}^{bkg} is the background selection efficiency) are evaluated. The results are illustrated in the plots of Figure 3.6.



FOM (Thrust 1-prong)



Signal selection efficiency vs background rejection power (Thrust 3-prong)



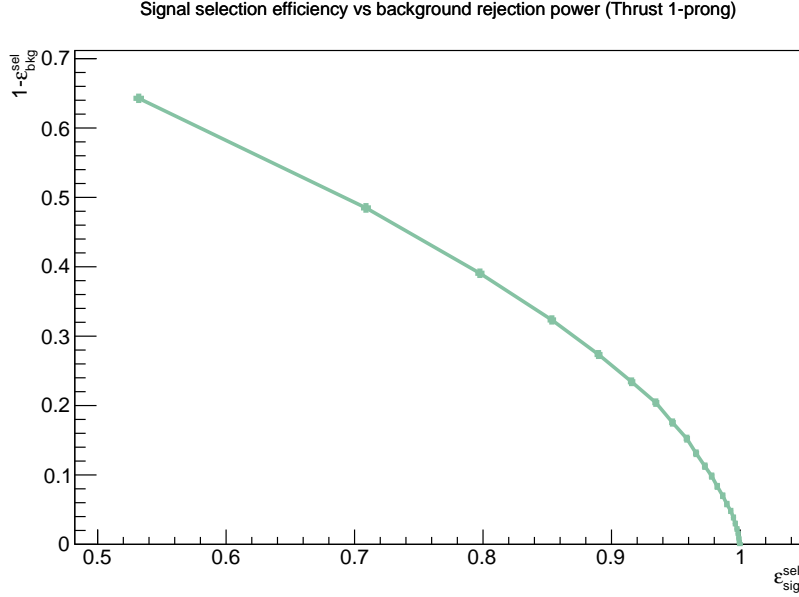


Figure 3.6: FOM and μ_{rej}^{bkg} vs ϵ_{sel}^{sig} plots for both selection optimizations on $\sum_{i=0}^2 \cos\theta_{Thrust_0_i}$ and $\cos\theta_{thrust_1_0}$.

The chosen and applied cuts that maximize the two FOMs are:

- $|\sum_{i=1}^3 \cos\theta_{thrust_0_i} > 2.54|$, with $\epsilon_{sel}^{sig} = 93.05\%$ and $\mu_{rej}^{bkg} = 65.75\%$;
- $|\cos\theta_{thrust_1_0} > 0.36|$, with $\epsilon_{sel}^{sig} = 99.28\%$ and $\mu_{rej}^{bkg} = 4.81\%$.

After the cuts applied in this selection, the overall situation is:

- $N_{tot} = 46135$, $N_{sig} = 33755$, $N_{bkg} = 12380$ (in which $N_{continuum} = 11417$ and $N_{B\bar{B}} = 963$), with $\epsilon_{sel}^{sig} = 72.27\%$, $\mu_{rej}^{bkg} = 76.95\%$.

Other cuts (and relative selection optimizations) has been applied on the missing momentum of event (p_{miss}) and on the invariant mass of $3\pi^\pm$ ($M_{inv}^{3-prong}$) without any improvement in terms of FOM, so they have been released. it is not excluded that with much more statistics these cuts could be more performing and therefore implemented.

3.4 Data-MonteCarlo agreement

The following distributions are compared to evaluate Data-MC agreement::

- $|\sum_{i=0}^2 \cos\theta_{thrust_0_i}|$, for 3-prong side (Figure 3.7);
- $|\cos\theta_{thrust_1_0}|$, for 1-prong side (Figure 3.8);
- p_{trk} , momentum of charged tracks measured in the CDC, both for 3-prong and 1-prong side (Figure 3.9 and 3.10);
- E_{ECL} , energy deposit of particles in the ECL, both for 3-prong and 1-prong side (Figure 3.11 and 3.12);
- E_{ECL}/p_{trk} , both for 3-prong and 1-prong side (Figure 3.13 and 3.14).
- p_{miss} , missing momentum of the event (Figure 3.15);
- $\theta_{p_{miss}}$, angle between beam axis and missing momentum of the event (Figure 3.16);
- θ_{ECL} , polar angle of clusters in the ECL, both for 3-prong and 1-prong side (Figure 3.17 and 3.18);
- $M_{inv}^{3-prong}$, invariant mass of the three charged tracks of the $\tau \rightarrow 3-prong$ channel (Figure 3.19);
- M_{miss}^2 , missing mass squared of the event (Figure 3.20);
- E_{vis}^{CMS} , visible energy of the event in the CMS (Figure 3.21)
- E_{miss}^{CMS} , missing energy of the event in the CMS (Figure 3.22);

All the MC distributions are normalized to the corresponding distributions in data to compare the shapes. In particular, the variable E/p is very useful to discriminate electrons, muons and pions: e^- s tend to deposit all their energy in the ECL (E/p peaking near 1, because the produced electromagnetic shower is all contained in the ECL), μ^- s are minimum ionizing particle (*MIP*, basically peaking in $E/p < 0.4$ region), while π^- s behavior is more similar to that of muons, with a smooth tail towards the electrons peak.

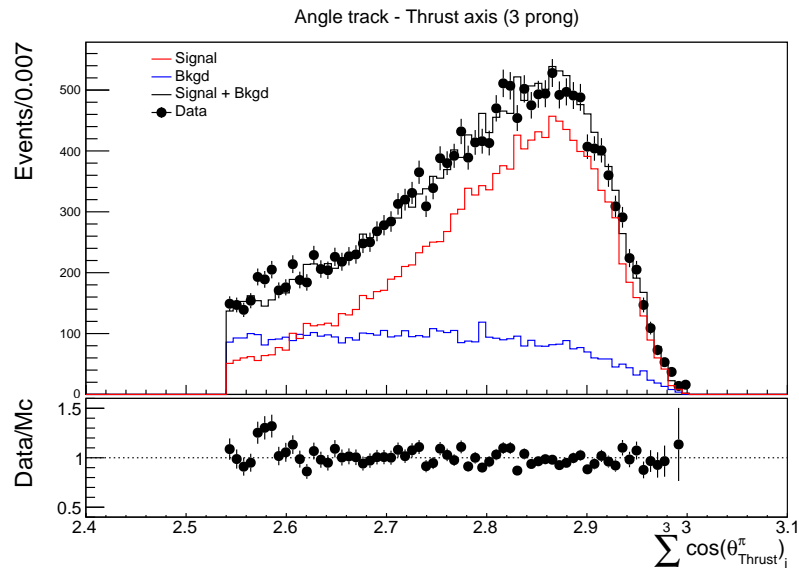


Figure 3.7: Comparison of data (dots) and MC (histograms) distributions of $|\sum_{i=0}^2 \cos\theta_{thrust_0_i}|$ variable.

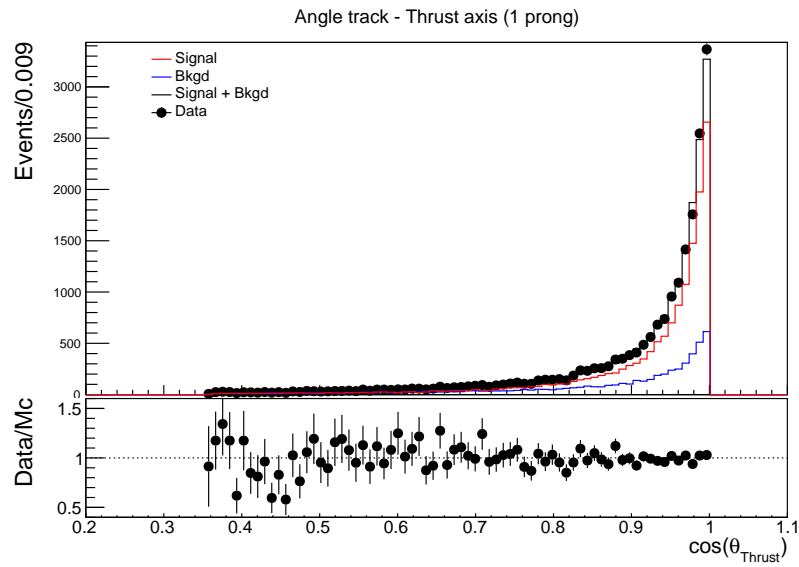


Figure 3.8: Comparison of data (dots) and MC (histograms) distributions of $|\cos\theta_{thrust_1_0}|$ variable.

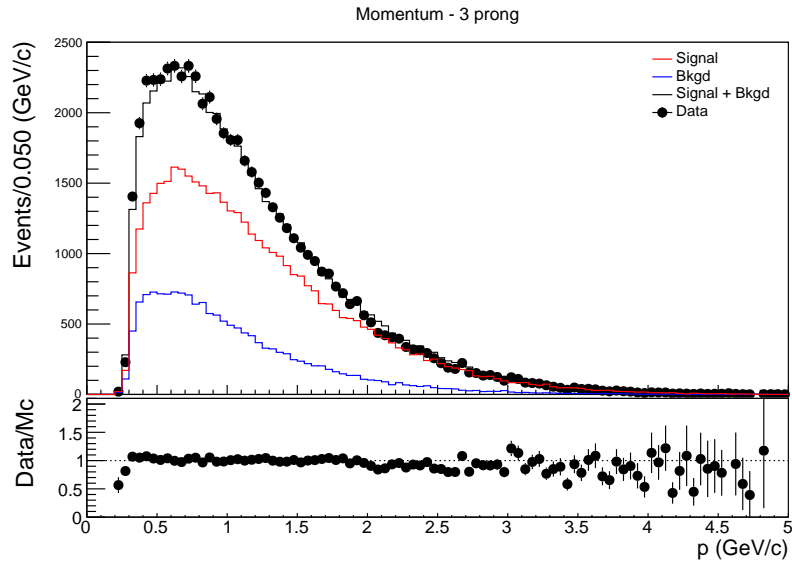


Figure 3.9: Comparison of data (dots) and MC (histograms) distributions of $p_{trk}^{3-prong}$ variable.

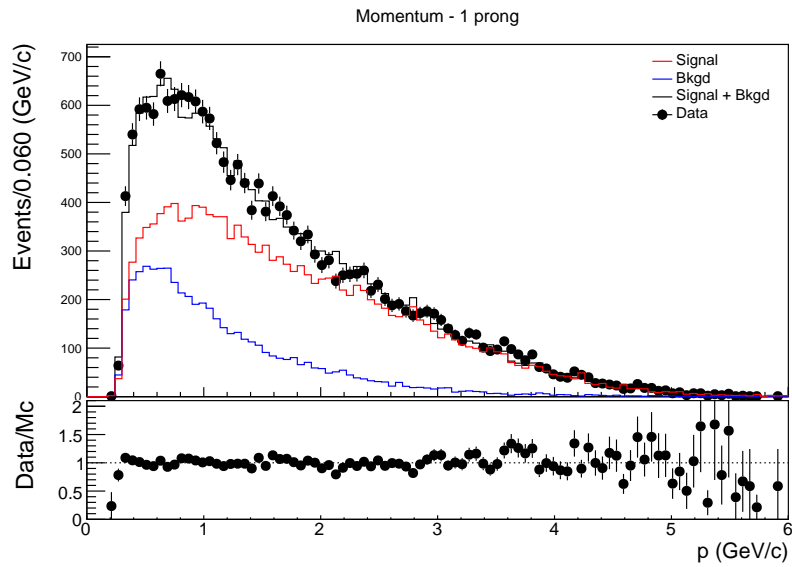


Figure 3.10: Comparison of data (dots) and MC (histograms) distributions of $p_{trk}^{1-prong}$ variable.

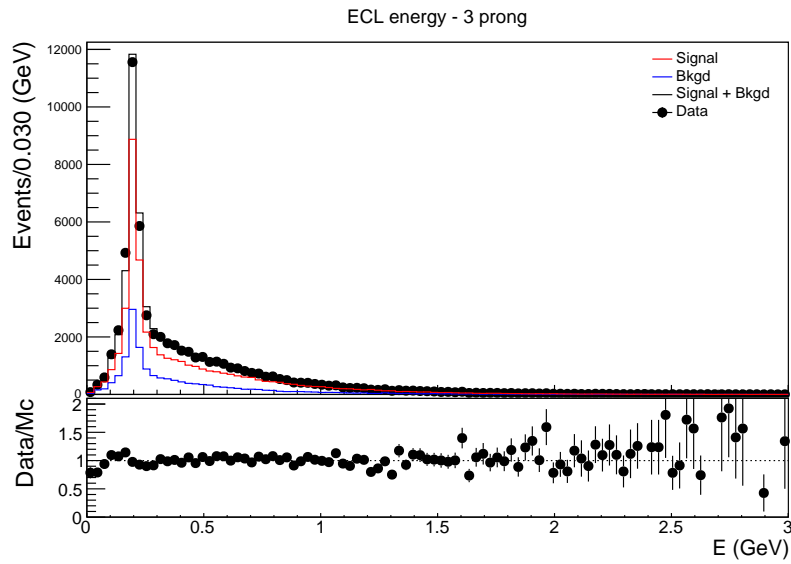


Figure 3.11: Comparison of data (dots) and MC (histograms) distributions of $E_{ECL}^{3-prong}$ variable.

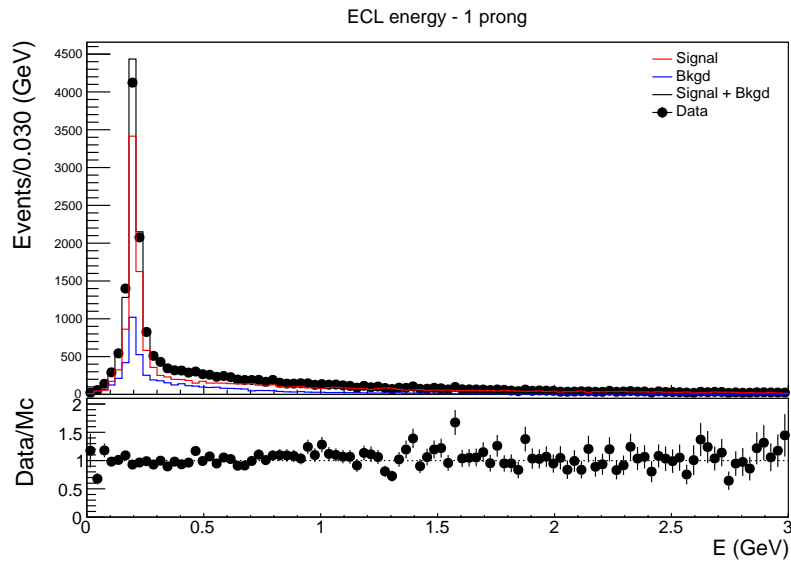


Figure 3.12: Comparison of data (dots) and MC (histograms) distributions of $E_{ECL}^{1-prong}$ variable.

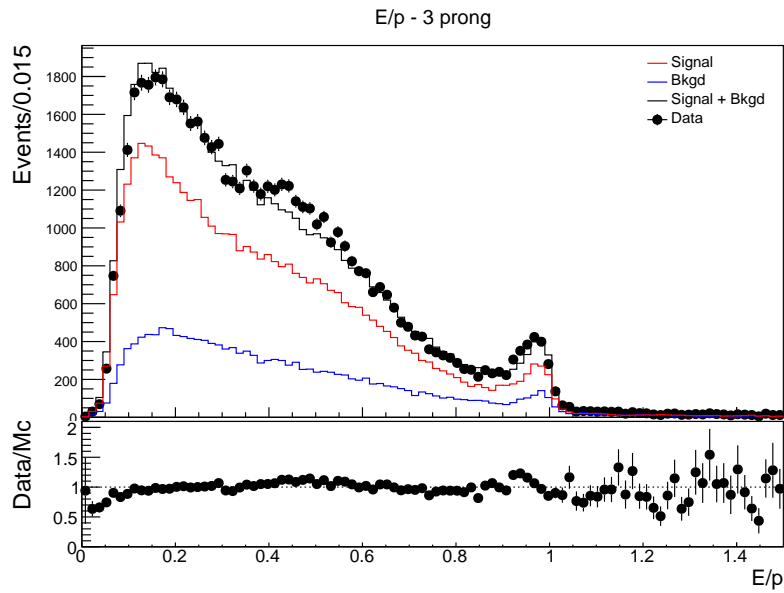


Figure 3.13: Comparison of data (dots) and MC (histograms) distributions of $E/p |_{3\text{-prong}}$ variable.

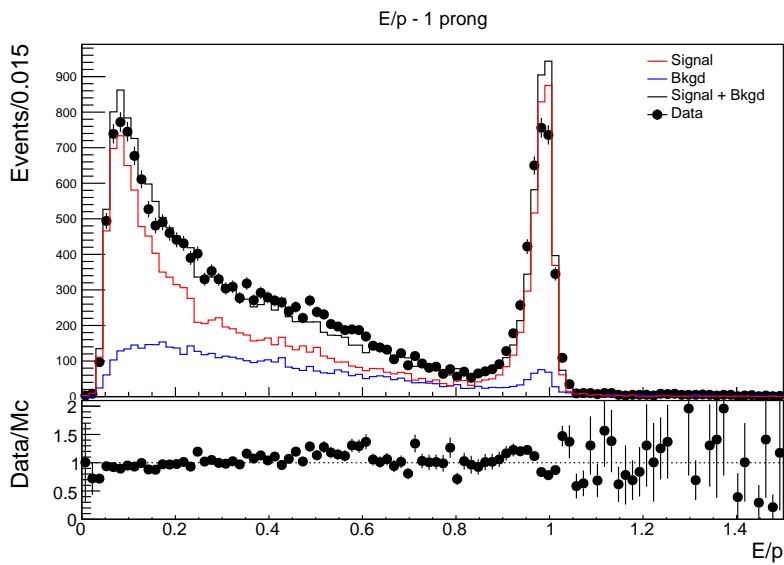


Figure 3.14: Comparison of data (dots) and MC (histograms) distributions of $E/p |_{1\text{-prong}}$ variable.

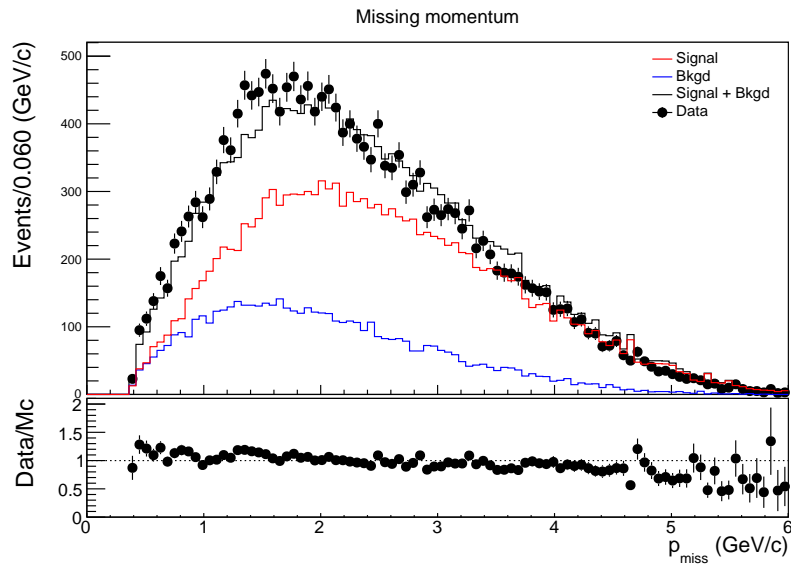


Figure 3.15: Comparison of data (dots) and MC (histograms) distributions of p_{miss} variable.

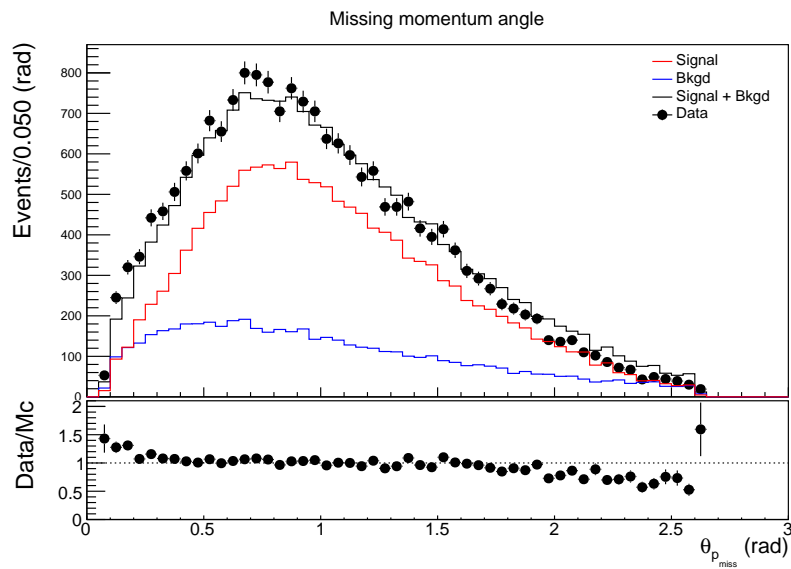


Figure 3.16: Comparison of data (dots) and MC (histograms) distributions of $\theta_{p_{miss}}$ variable.

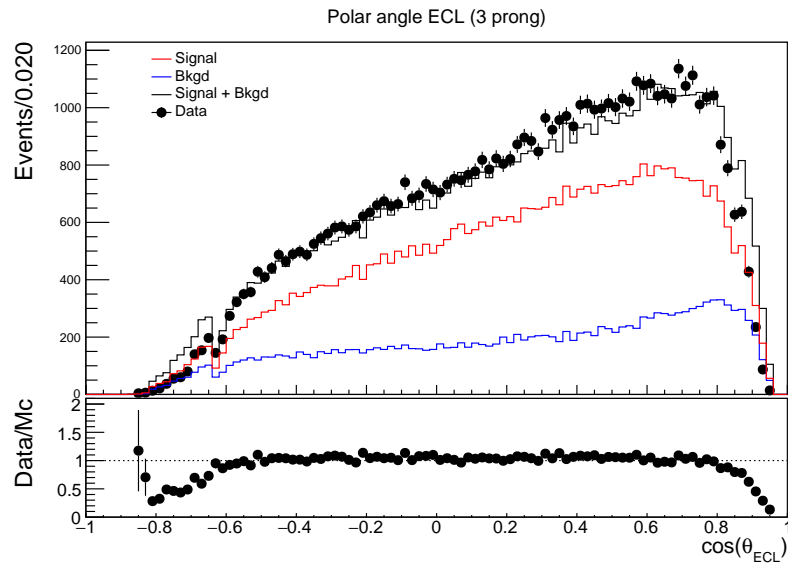


Figure 3.17: Comparison of data (dots) and MC (histograms) distributions of $\theta_{ECL}^{3-prong}$ variable.

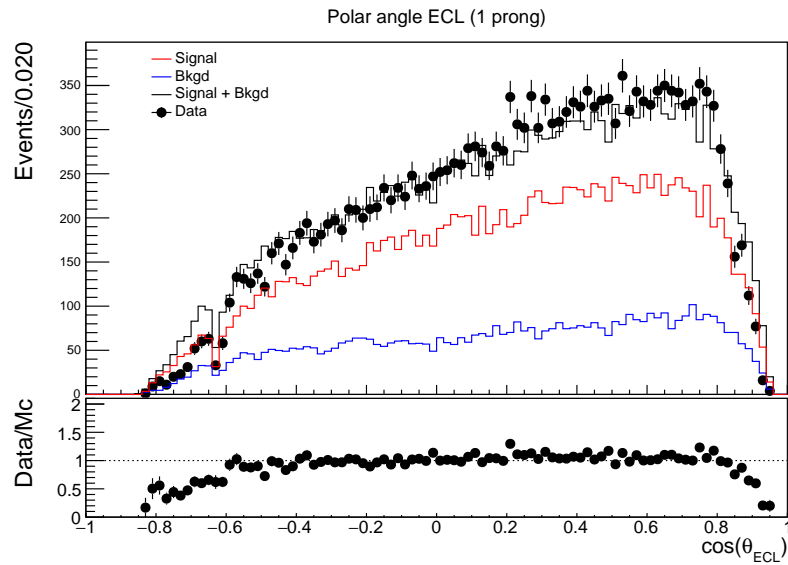


Figure 3.18: Comparison of data (dots) and MC (histograms) distributions of $\theta_{ECL}^{1-prong}$ variable.

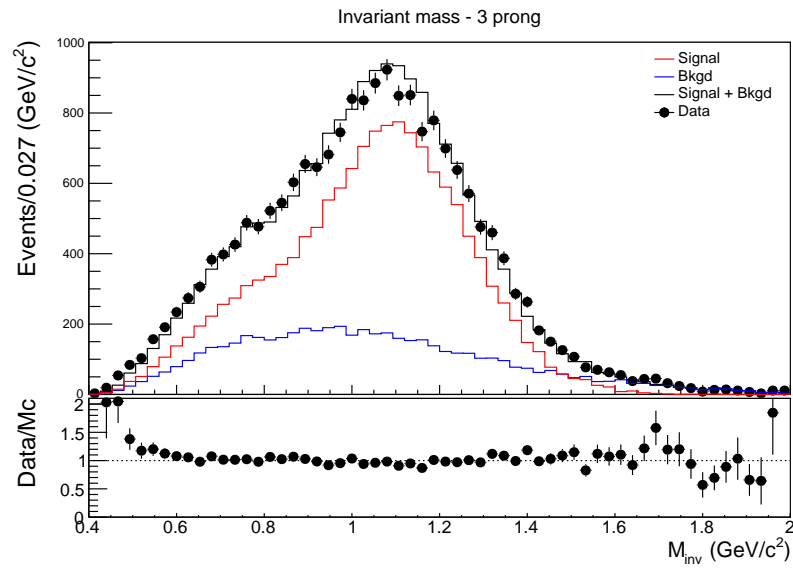


Figure 3.19: Comparison of data (dots) and MC (histograms) distributions of $M_{\text{inv}}^{3\text{-prong}}$ variable.

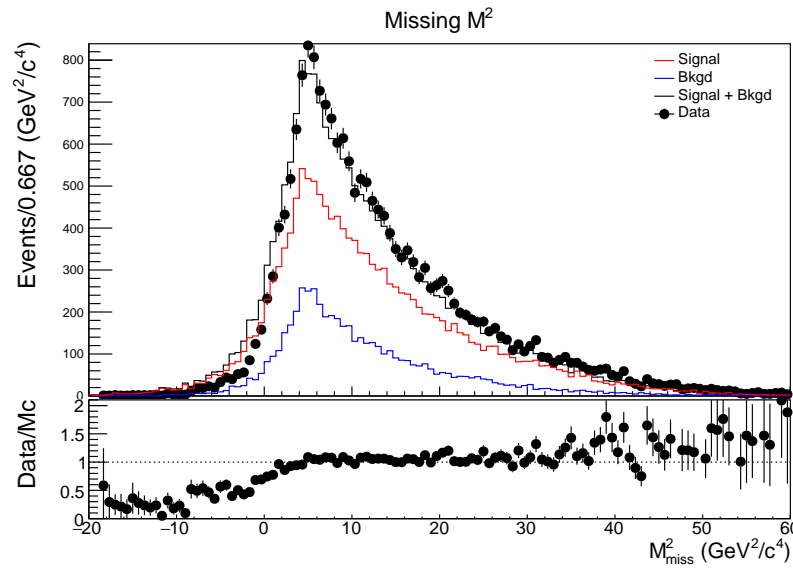


Figure 3.20: Comparison of data (dots) and MC (histograms) distributions of M_{miss}^2 variable.

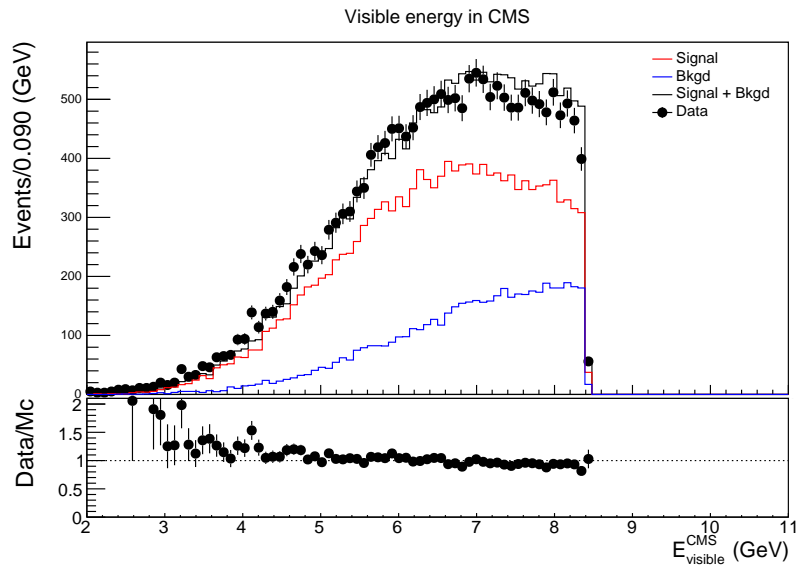


Figure 3.21: Comparison of data (dots) and MC (histograms) distributions of E_{vis}^{CMS} variable.

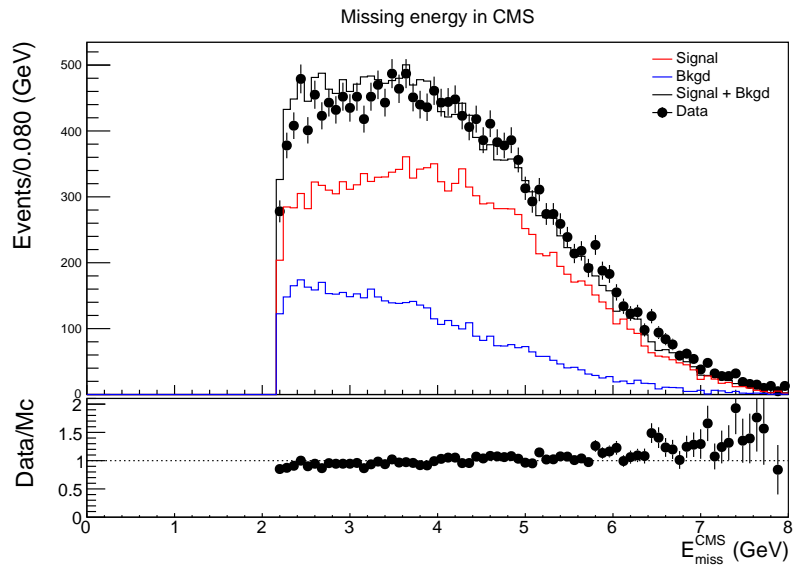


Figure 3.22: Comparison of data (dots) and MC (histograms) distributions of E_{miss}^{CMS} variable.

The agreements are generally satisfying, although the major discrepancies are observed for low missing momentum and for θ_{ECL} (in the backward and forward end-cap regions) distributions. Moreover the electron peak in the E/p 1-prong distribution is not well reproduced by MC: in the MC simulation the peak is higher and centered on 1, while in the data it is more shifted on the left and broader. Probably this discrepancy is due to the imperfect calibration of the ECL.

3.5 Data-driven technique

Starting from the MonteCarlo truth, it is possible to extract the electron, muon, pion, kaon and proton fractions respect to the total in the 1-prong sample (considering signal plus background). They are reported in Table 3.2.

	f
e^\pm	20.50%
μ^\pm	19.69%
π^\pm	52.77%
K^\pm	4.63%
p^\pm	2.24%

Table 3.2: MonteCarlo fractions of electrons, muons, charged pions, charged kaons and protons in 1-prong side.

The contributions of these particle species to E/p 1-prong distribution of MC simulation are shown in Figure 3.23.

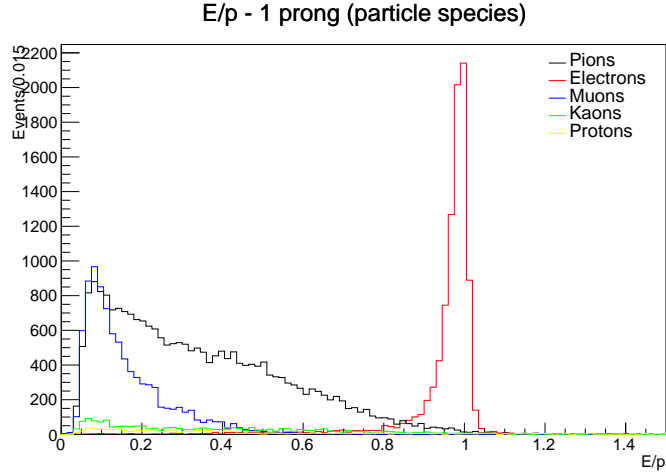


Figure 3.23: E/p 1-prong MC distribution splitted in particle species contributes.

Assuming these fractions on real data as well, the idea is to take the E/p 3-prong distributions both for data and MC and to rescale them to the fraction:

$$f_{had} = \frac{f_{\pi} + f_K + f_p}{3}, \quad (3.4)$$

where the 3 factor takes into account the fact that the histograms of 3-prong distributions are filled with three charged track candidates per event. In Figure 3.24 is reported the histogram of the MC distribution rescaled to the fraction f_{had} .

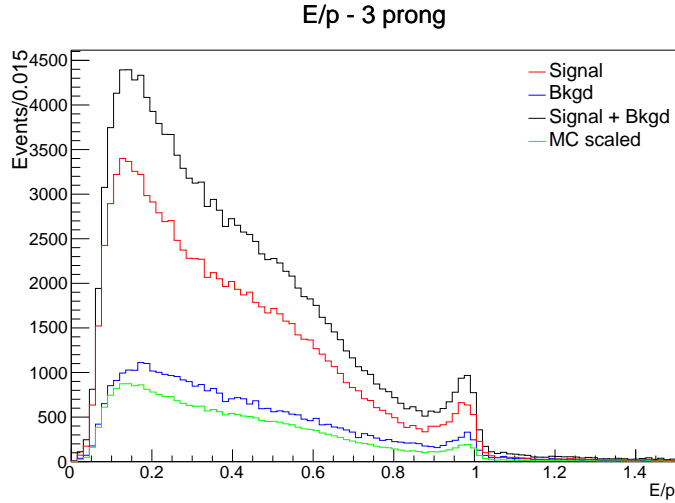


Figure 3.24: E/p 3-prong MC distribution in which the signal plus background component is scaled to the hadronic fraction f_{had} .

Now it is possible to proceed with a subtraction between histograms of E/p 1-prong and rescaled E/p 3-prong distributions. This operation allows to remove from the E/p 1-prong distribution the hadronic contribution in a data-driven way. The resulting distribution is showed in Figure 3.25.

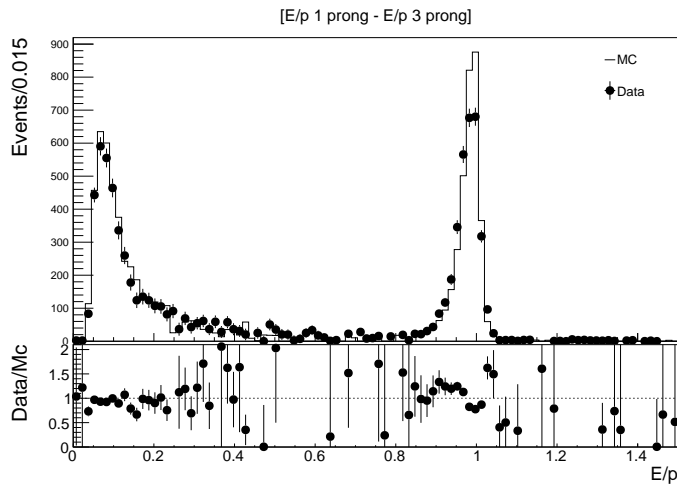
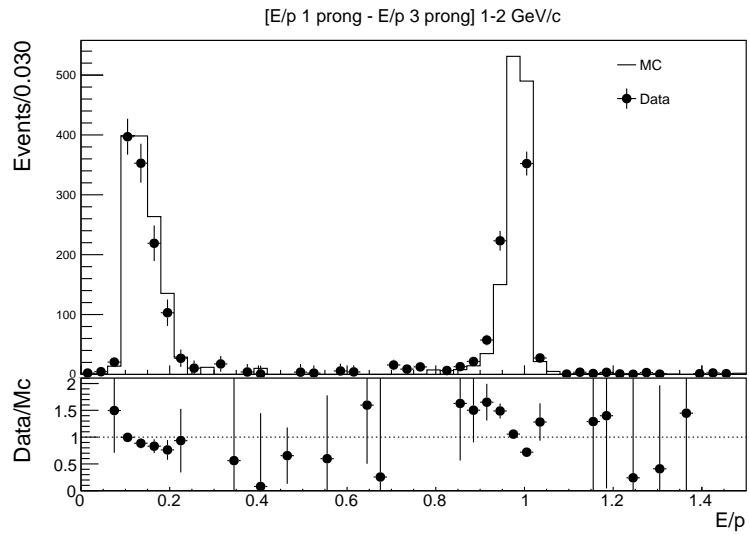
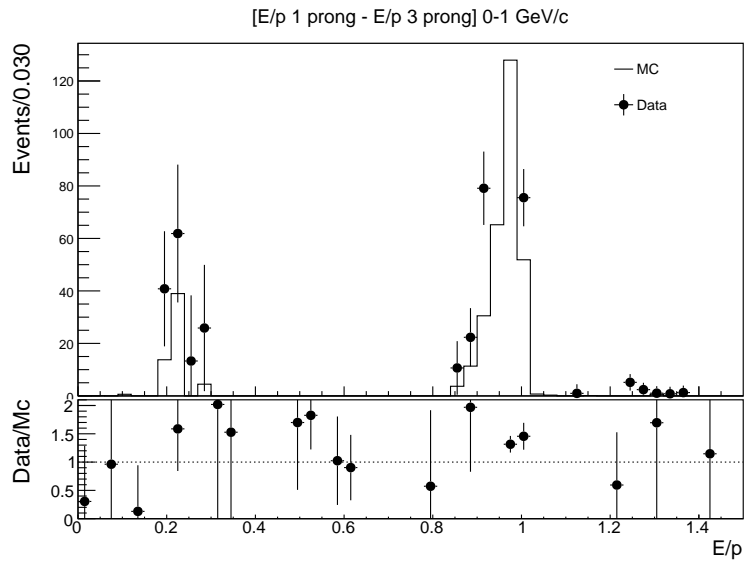


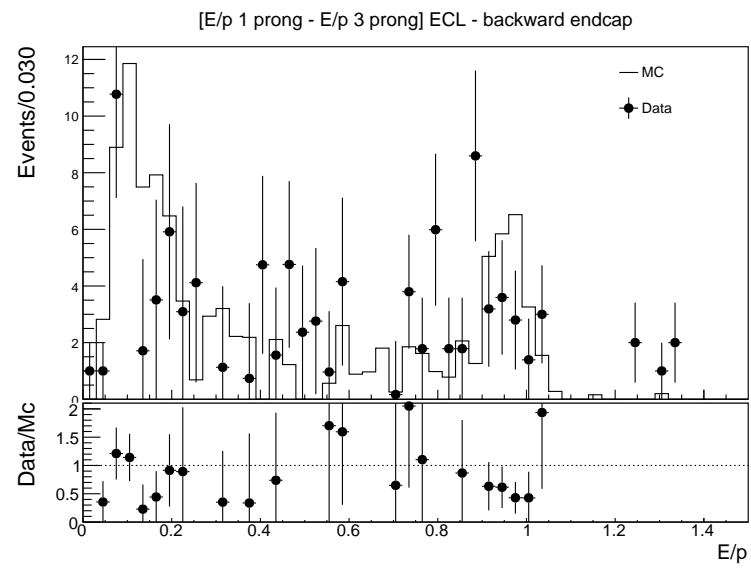
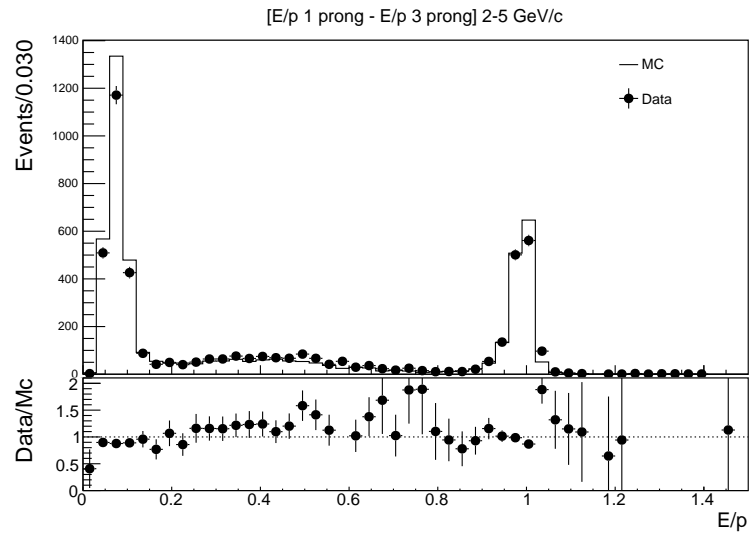
Figure 3.25: Resulting subtraction between $E/p^{1-prong}$ and scaled $E/p^{3-prong}$ distribution both for data and MC and their agreement.

The next step is to repeat this operation in the same way in ranges of momentum and angular regions of ECL:

- $0 < p < 1 \text{ GeV}/c$;
- $1 < p < 2 \text{ GeV}/c$;
- $2 < p < 5 \text{ GeV}/c$;
- ECL forward barrel ($12.01^\circ - 31.36^\circ$);
- ECL barrel ($32.2^\circ - 128.7^\circ$);
- ECL backward end-cap ($131.5^\circ - 155.03^\circ$).

In each region the hadronic fractions f_{had} are computed and used to rescale the corresponding E/p 3-prong distributions, then the subtractions are performed. The resulting distributions for different momentum intervals and for different ECL angular regions are reported in Figure 3.26. It is clear that this technique removes most of hadronic contribution from E/p 1-prong distributions. In each resulting histogram electron and muon peaks are well visible and distinct. In few of these regions data-MC agreement is not entirely satisfying. Moreover the poor statistics makes the agreements hard to establish. This technique allows a brilliant separation of leptonic peaks and to easily count electrons and muons in a certain phase space region without any use of particle identification criteria. Currently it is not possible to proceed further due to low statistics, but a more targeted use in the future is foreseen.





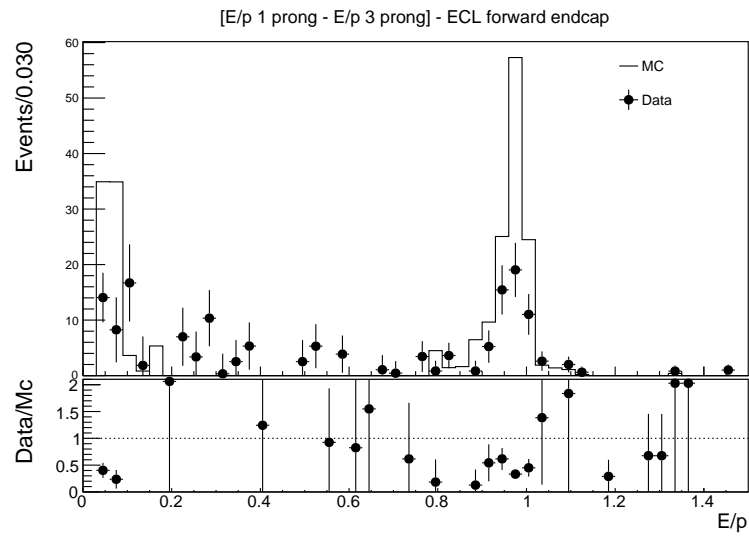
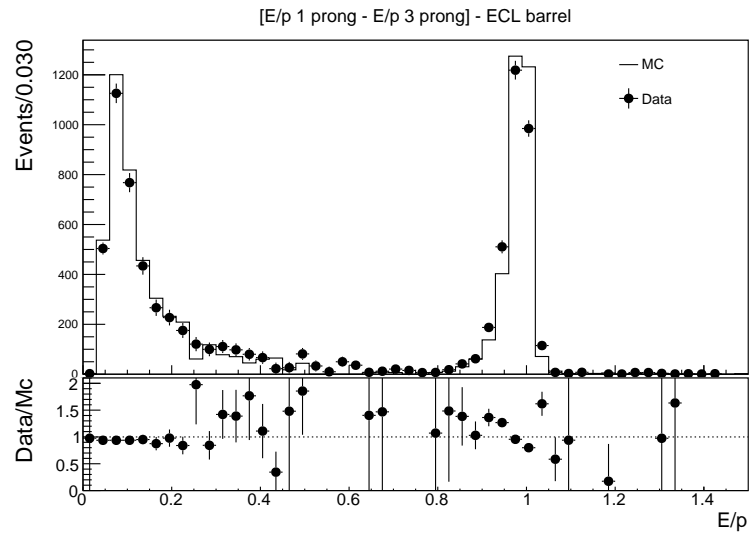


Figure 3.26: Resulting subtraction between $E/p^{1-prong}$ and scaled $E/p^{3-prong}$ distributions both for data and MC and their agreement, in ranges of momentum and angular regions of ECL.

Chapter 4

Study of $B \rightarrow \tau\nu$ decay

The aim of this chapter is to describe the sensitivity of the Belle II experiment to the search for $B \rightarrow \tau\nu$ decays performed on MonteCarlo simulated samples corresponding to an integrated luminosity of 1.6 ab^{-1} . First, a brief technical description of the dataset used is given, followed by the discussion of the strategy implemented in order to reject the most abundant backgrounds. The $B \rightarrow \tau\nu$ signal is searched for using the 1-prong decays of τ lepton: $\tau^- \rightarrow e^- \bar{\nu}_e \nu_\tau$, $\tau^- \rightarrow \mu^- \bar{\nu}_\mu \nu_\tau$, $\tau^- \rightarrow \pi^- \nu_\tau$, $\tau^- \rightarrow \rho^- \nu_\tau$ with $\rho^- \rightarrow \pi^- \pi^0$. The Full Event Interpretation to select the B_{tag} in each event and the Boost Decision Tree to suppress the continuum background are described. Subsequently, the signal selection and its optimization are described in detail. A projection to higher integrated luminosity is illustrated to show at which values it will be possible to reach the 5σ statistical significance of the signal and how the statistical and systematic uncertainties reduce with the increasing accumulated statistics. Finally, extended maximum likelihood fits for each of the four τ decay modes are performed on the data-challenge sample, corresponding to an integrated luminosity of 1 ab^{-1} and statistically independent of the MonteCarlo samples, in order to extract the signal yields and then the branching ratio of $B \rightarrow \tau\nu$.

4.1 Dataset

The MC production is based on the 9th campaign. The following categories of events have been simulated:

Category	Number of pairs
$e^+e^- \rightarrow \Upsilon(4S) \rightarrow B^+B^-, B^+ \rightarrow \text{generic}, B^- \rightarrow \tau^-\bar{\nu}_\tau$	7.94×10^7
$e^+e^- \rightarrow \Upsilon(4S) \rightarrow B^+B^-$	9.03×10^8
$e^+e^- \rightarrow \Upsilon(4S) \rightarrow B^0\bar{B}^0$	9.03×10^8
$e^+e^- \rightarrow u\bar{u}$	2.57×10^9
$e^+e^- \rightarrow d\bar{d}$	6.40×10^8
$e^+e^- \rightarrow c\bar{c}$	3.04×10^8
$e^+e^- \rightarrow s\bar{s}$	2.08×10^9
$e^+e^- \rightarrow \tau^+\tau^-$	1.47×10^9

Table 4.1: Categories of simulated events and corresponding generated pairs.

The generated $B\bar{B}$, continuum and τ pair backgrounds correspond to an integrated luminosity of 1.6 ab^{-1} . An additional simulated sample used is the data-challenge sample, which serve to mimic real data with unknown new physics contributions. The data-challenge sample corresponds to an integrated luminosity of $L = 1 \text{ ab}^{-1}$. Each MC sample is therefore preliminary normalized to $L = 1 \text{ ab}^{-1}$. The Basf2 release used to generate the Ntuples is 02-01-00. Preliminary requirements are applied on charged tracks:

- $|d_0| < 2 \text{ cm}$, $|z_0| < 4 \text{ cm}$ (impact parameters) and $0.29670 \text{ rad} < \theta < 2.61799 \text{ rad}$ (CDC acceptance).

Due to the high level of machine background in Belle II (\sim a factor 20 more than in Belle) a study has been performed on MC simulated events to optimally select the photon candidates from e^+e^- collisions (*physics photons*) and reject beam induced background photon candidates (*background photons*). Two cluster-related discriminating variables have been exploited, i.e. the cluster energy and the cluster timing. Physics photon candidates are required to satisfy a minimum energy threshold since they have a harder energy spectrum than background photons. Beam-induced photon production is not correlated with bunch crossing, and so the cluster time distribution

shows an uniform distribution for background photons and a peak near the bunch crossing time for physics photons. These photon candidates are used in π^0 reconstruction and for determining the remaining energy deposition in the calorimeter from physics photons. The requirements imposed are the following:

- γ from π^0 : $E_{cluster} > 50 \text{ MeV}$ and $|T_{cluster}| < |\Delta T_{cluster}|$;
- extra clusters: $E_{cluster} > 55 \text{ MeV}$ and $|T_{cluster}| < |\Delta T_{cluster}|$,

where $E_{cluster}$ is the energy of the cluster, $T_{cluster}$ is the time measured by the ECL and $\Delta T_{cluster}$ is the estimated uncertainty of $T_{cluster}$. The cut on the cluster timing has an efficiency equal to 99% for physics photons.

4.2 Signal event selection

The decay of one of the B mesons in the event is fully reconstructed (B_{tag}) and the properties of the remaining particles in the event (B_{sig}) are compared to those expected for signal and background. The requirement is that all remaining particles in the events after removing B_{tag} daughters are consistent with the decay product of $B \rightarrow \tau \nu$.

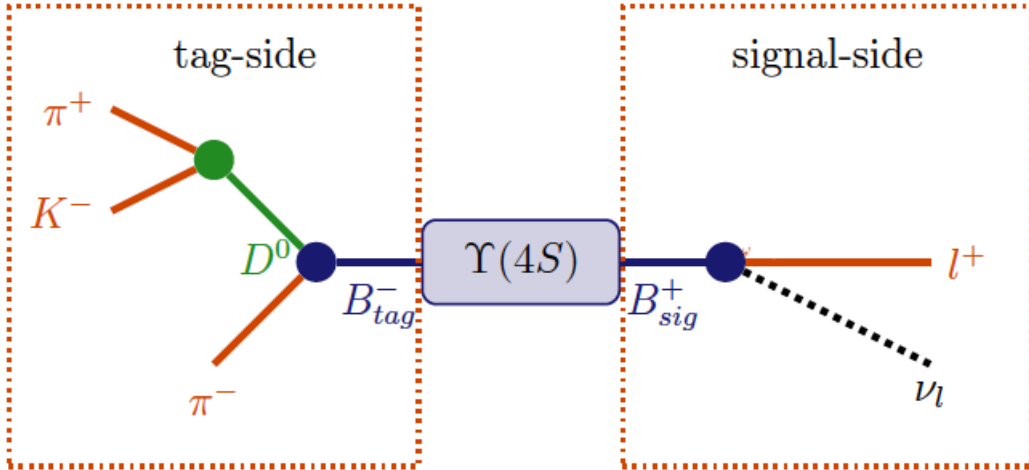


Figure 4.1: Decay of $\Upsilon(4S)$ into a charged B meson pair. The signal-side is shown on the right and an example of tag-side on the left.

4.2.1 Full Event Interpretation

The Full Event Interpretation (FEI) is part of BASF2 software package [21]. The algorithm is implemented purely in Python and takes care of:

- reconstructing a user-defined multi-level decay topology;
- training mutually dependent multivariate classifiers (MVCs) for each decay channel;
- determining sensible channel-specific pre-cuts and particle-specific post-cuts to reduce combinatorics;
- generating a document summarizing the key performance indicators and control plots of all decay channels and particles used in the FEI.

The reconstructed decay topology, methods and variables used in the multivariate classification are defined by the user. The FEI automatically reconstructs one out of the two B mesons in an $\Upsilon(4S)$ decay to recover information about the remaining B meson. In fact there is an entire class of analysis methods (*tagging-methods*) based on this concept. There are three distinct tagging-methods:

- hadronic tagging: solely uses hadronic decay channels for the reconstruction. Hence, the kinematics of the reconstructed candidates are well known and the tagged sample is the purest. This tagging is only possible for a tiny fraction of the dataset on the order of a few per mille;
- semileptonic tagging: uses semileptonic B decays. Due to the high branching ratio of semileptonic decays this approach usually has a higher tagging efficiency. On the other hand, the semileptonic reconstruction suffers from missing kinematic information due to the neutrino in the final state of the decay. Hence, the sample is not as pure as in the hadronic case;
- inclusive tagging: combines the four-momenta of all particles in the rest of the event of the signal-side B candidate. The achieved tagging

efficiency is usually one order of magnitude above the hadronic and semileptonic tagging. Yet the decay topology is not explicitly reconstructed and cannot be used to discard wrong candidates. In consequence, the methods suffers from a high background and the tagged sample is very impure.

The basic idea of the Full Event Interpretation is to reconstruct the particles and train the multivariate classifiers in a hierarchical approach. The approach is depicted in Figure 4.2. At first the final-state particle candidates are selected and corresponding classification methods are trained using the detector information. Building on this, intermediate particle candidates are reconstructed and a multivariate classifier is trained for each employed decay channel. The MVC combines all information about a candidate into a single value, i.e. the *signal-probability* (SigProb). In consequence, candidates from different decay channels can be treated equally in the following reconstruction steps.

Finally, the B candidates are reconstructed and the corresponding classifiers are trained. The final output of the FEI to the user contains four particle lists: B^+ : hadronic, B^+ : semileptonic, B^0 : hadronic, B^0 : semileptonic.

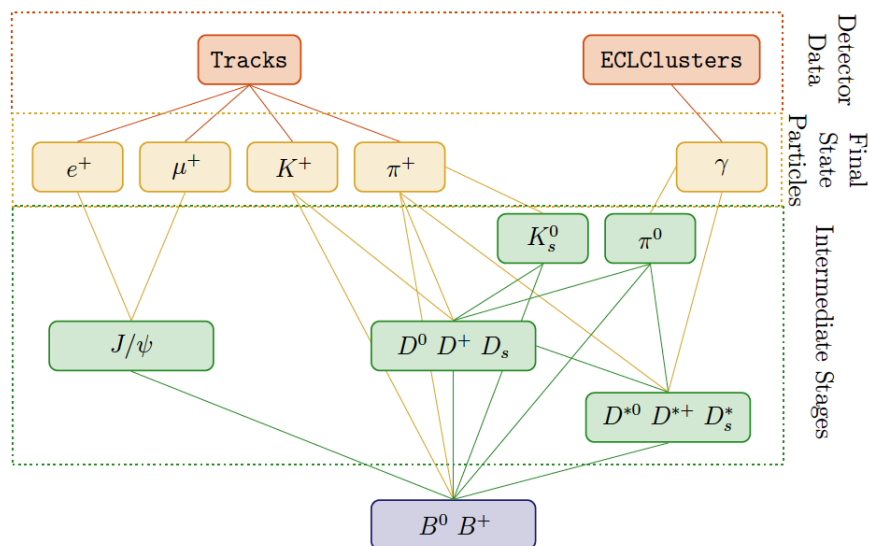


Figure 4.2: Hierarchical approach of the Full Event Interpretation.

The hadronic tagging-method is used in this analysis. The training of FEI classifier has been performed on $100 fb^{-1}$ of generic B^+B^- events (MC9 sample). The hadronic decay modes included in the FEI are summarized in Table 4.2.

B^+ modes	B^0 modes	D^+, D^{*+}, D_s^+ modes
$B^+ \rightarrow \bar{D}^0\pi^+$	$B^0 \rightarrow D^-\pi^+$	$D^+ \rightarrow K^-\pi^+\pi^+$
$B^+ \rightarrow \bar{D}^0\pi^+\pi^0$	$B^0 \rightarrow D^-\pi^+\pi^0$	$D^+ \rightarrow K^-\pi^+\pi^+\pi^0$
$B^+ \rightarrow \bar{D}^0\pi^+\pi^0\pi^0$	$B^0 \rightarrow D^-\pi^+\pi^+\pi^-$	$D^+ \rightarrow K^-K^+\pi^+$
$B^+ \rightarrow \bar{D}^0\pi^+\pi^+\pi^-$	$B^0 \rightarrow D_s^+D^-$	$D^+ \rightarrow K^-K^+\pi^+\pi^0$
$B^+ \rightarrow D_s^+\bar{D}^0$	$B^0 \rightarrow D^{*-}\pi^+$	$D^+ \rightarrow K_s^0\pi^+$
$B^+ \rightarrow \bar{D}^{*0}\pi^+$	$B^0 \rightarrow D^{*-}\pi^+\pi^0$	$D^+ \rightarrow K_s^0\pi^+\pi^0$
$B^+ \rightarrow \bar{D}^{*0}\pi^+\pi^0$	$B^0 \rightarrow D^{*-}\pi^+\pi^+\pi^-$	$D^+ \rightarrow K_s^0\pi^+\pi^+\pi^-$
$B^+ \rightarrow \bar{D}^{*0}\pi^+\pi^+\pi^-$	$B^0 \rightarrow D^{*-}\pi^+\pi^+\pi^-\pi^0$	$D^{*+} \rightarrow D^0\pi^+$
$B^+ \rightarrow \bar{D}^{*0}\pi^+\pi^+\pi^-\pi^0$	$B^0 \rightarrow D_s^{*+}D^-$	$D^{*+} \rightarrow D^+\pi^0$
$B^+ \rightarrow D_s^{*+}\bar{D}^0$	$B^0 \rightarrow D_s^+D^{*-}$	$D_s^+ \rightarrow K^+K_s^0$
$B^+ \rightarrow D_s^+\bar{D}^{*0}$	$B^0 \rightarrow D_s^{*+}D^{*-}$	$D_s^+ \rightarrow K^+\pi^+\pi^-$
$B^+ \rightarrow \bar{D}^0K^+$	$B^0 \rightarrow J/\psi K_s^0$	$D_s^+ \rightarrow K^+K^-\pi^+$
$B^+ \rightarrow D^-\pi^+\pi^+$	$B^0 \rightarrow J/\psi K^+\pi^+$	$D_s^+ \rightarrow K^+K^-\pi^+\pi^0$
$B^+ \rightarrow J/\psi K^+$	$B^0 \rightarrow J/\psi K_s^0\pi^+\pi^-$	$D_s^+ \rightarrow K^+K_s^0\pi^+\pi^-$
$B^+ \rightarrow J/\psi K^+\pi^+\pi^-$		$D_s^+ \rightarrow K^-K_s^0\pi^+\pi^+$
$B^+ \rightarrow J/\psi K^+\pi^0$		$D_s^+ \rightarrow K^+K^-\pi^+\pi^-\pi^-$
$B^+ \rightarrow D^-\pi^+\pi^+\pi^0$	$B^0 \rightarrow D^-\pi^+\pi^0\pi^0$	$D_s^+ \rightarrow \pi^+\pi^+\pi^-$
$B^+ \rightarrow \bar{D}^0\pi^+\pi^+\pi^-\pi^0$	$B^0 \rightarrow D^-\pi^+\pi^+\pi^-\pi^0$	$D_s^{*+} \rightarrow D_s^+\pi^0$
$B^+ \rightarrow \bar{D}^0D^+$	$B^0 \rightarrow \bar{D}^0\pi^+\pi^-$	$D^+ \rightarrow \pi^+\pi^0$
$B^+ \rightarrow \bar{D}^0D^+K_s^0$	$B^0 \rightarrow D^-D^0K^+$	$D^+ \rightarrow \pi^+\pi^+\pi^-$
$B^+ \rightarrow \bar{D}^{*0}D^+K_s^0$	$B^0 \rightarrow D^-D^{*0}K^+$	$D^+ \rightarrow \pi^+\pi^+\pi^-\pi^0$
$B^+ \rightarrow \bar{D}^0D^{*+}K_s^0$	$B^0 \rightarrow D^{*-}D^0K^+$	$D^+ \rightarrow K^+K_s^0K_s^0$
$B^+ \rightarrow \bar{D}^{*0}D^{*+}K_s^0$	$B^0 \rightarrow D^{*-}D^{*0}K^+$	$D^{*+} \rightarrow D^+\gamma$
$B^+ \rightarrow \bar{D}^0D^+K^+$	$B^0 \rightarrow D^-D^+K_s^0$	$D_s^+ \rightarrow K_s^0\pi^+$
$B^+ \rightarrow \bar{D}^{*0}D^+K^+$	$B^0 \rightarrow D^{*-}D^+K_s^0$	$D_s^+ \rightarrow K_s^0\pi^+\pi^0$
$B^+ \rightarrow \bar{D}^0D^{*+}K^+$	$B^0 \rightarrow D^-D^{*+}K_s^0$	$D_s^{*+} \rightarrow D_s^+\pi^0$
$B^+ \rightarrow \bar{D}^{*0}D^{*+}K^+$	$B^0 \rightarrow D^{*-}D^{*+}K_s^0$	
$B^+ \rightarrow \bar{D}^{*0}\pi^+\pi^0\pi^0$	$B^0 \rightarrow D^{*-}\pi^+\pi^0\pi^0$	

Table 4.2: B^+ , B^0 and D decay modes included in the FEI.

Some loose cuts are applied in order to reduce the number of B_{tag} candi-

dates:

- $M_{bc} > 5.24 \text{ GeV}$, where $M_{bc} = \sqrt{E_{beam}^2 - |\vec{p}_B|^2}$ is the beam-energy-constrained mass defined in the e^+e^- CMS (E_{beam} is the beam energy and $|\vec{p}_B|$ is the momentum of the B meson candidate);
- $|\Delta E| < 200 \text{ MeV}$, where $\Delta E = E_B - E_{beam}$ (E_B is the energy of the B meson candidate);
- $SigProb > 0.01$;
- $R_2 < 0.4$, where $R_2 = H_2/H_0$, with $H_l = \sum_{i,j}^N |p_i||p_j|P_l(\cos\theta_{ij})$ the Super-Fox-Wolfram momentum of order l (θ_{ij} the angle between the momenta p_i and p_j , P_l the Legendre polynomial of order l) [21].

M_{bc} and ΔE are constructed from the measured momenta and energies of visible decay products. In the case that multiple candidates are reconstructed in the event the one with the highest FEI discriminant is chosen. The $SigProb$ distribution at this stage is shown in Figure 4.3.

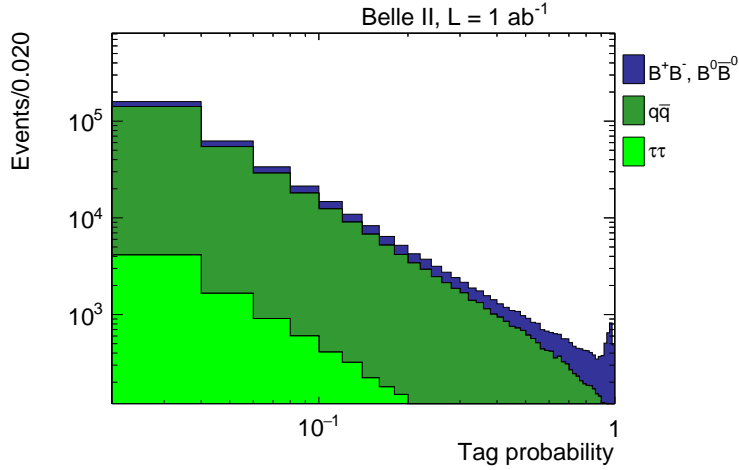


Figure 4.3: $SigProb$ distribution for $B\bar{B}$ background (blue), continuum (green) and τ pair (light green).

4.2.2 Event selection for B_{sig}

In the events where a B_{tag} is reconstructed, the presence of only one additional track is required, consistent with a 1-prong τ decay modes.

The charged particle identification (PID) relies on likelihood based selectors: the informations from the detector systems, i.e. specific ionization (dE/dx) from the SVD and the CDC, E/p from ECL and measurements from TOP, ARICH and KLM are analyzed independently to determine a likelihood for each charged particle hypothesis (electron, muon, pion, kaon, proton and deuteron). The likelihoods from each detector are used to construct a combined likelihood ratio:

$$\frac{\mathcal{L}(particle)}{\mathcal{L}(e) + \mathcal{L}(\mu) + \mathcal{L}(\pi) + \mathcal{L}(K) + \mathcal{L}(p) + \mathcal{L}(d)}. \quad (4.1)$$

Particle identification criteria are applied to select the following τ decay modes:

- $e^- \bar{\nu}_e \nu_\tau$;
- $\mu^- \bar{\nu}_\mu \nu_\tau$;
- $\pi^- \nu_\tau$;
- $\pi^- \pi^0 \nu_\tau$ ($\rho^- \nu_\tau$).

The selected categories all together correspond to approximately 72% of all τ decays.

Candidate events are required to have one charged track into signal-side for which the charge is opposite to that of B_{tag} . The working points of the PID official group are exploited (95% of identification efficiency for electrons, muons and kaons - 85% for pions). Tracks satisfying $EID > 0.047$ are taken as electron candidates for the $e^- \bar{\nu}_e \nu_\tau$ mode. The remaining tracks not passing the EID selection and satisfying $MUID > 0.008$ are taken as muon candidates for the $\mu^- \bar{\nu}_\mu \nu_\tau$ mode. The remaining tracks not passing the EID and the $MUID$ selections and satisfying $PID > 0.275$ are taken as pion candidates for the $\pi^- \nu_\tau$ and $\pi^- \pi^0 \nu_\tau$ modes. In additions, for the $\pi^- \pi^0 \nu_\tau$ mode is required only one π^0 candidate for which no daughter photons are

used in the B_{tag} reconstruction and the invariant mass of the state $\pi^-\pi^0$ is required to be within $625 \text{ MeV}/c^2 < M_{\pi^-\pi^0} < 925 \text{ MeV}/c^2$. In turn the π^0 candidates are reconstructed by pairing two neutral clusters and applying the invariant mass cut on the $\gamma\gamma$ pair of $120 \text{ MeV}/c^2 < m_{\gamma\gamma} < 160 \text{ MeV}/c^2$.

Mis-reconstructed B_{tag} candidates are suppressed requiring that the beam-energy constrained mass (Figure 4.4) $5.275 \text{ GeV}/c^2 < M_{bc} < 5.290 \text{ GeV}/c^2$.

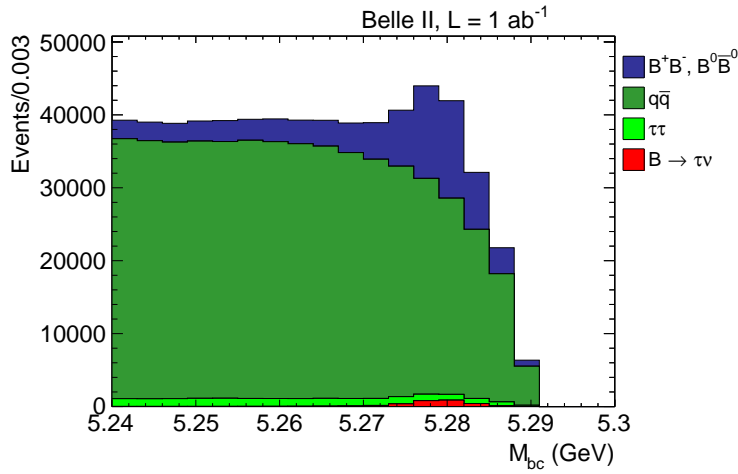


Figure 4.4: M_{bc} distribution before the cut on M_{bc} for signal (red, enhanced by a factor 15), $B\bar{B}$ background (blue), continuum (green) and τ pair (light green).

A powerful constrain is exploited at this stage to suppress the background, i.e. the missing mass squared defined as

$$M_{miss}^2 = \left(2E_{beam} - E_{B_{tag}} - E_{B_{sig}}\right)^2 - \left(p_{B_{tag}} - p_{B_{sig}}\right)^2. \quad (4.2)$$

A cut is imposed on M_{miss}^2 for both leptonic and hadronic modes (Figure 4.5 and 4.6):

- $(M_{miss}^2)_{lep} > 10 \text{ GeV}^2/c^4$;
- $(M_{miss}^2)_{had} < 12 \text{ GeV}^2/c^4$.

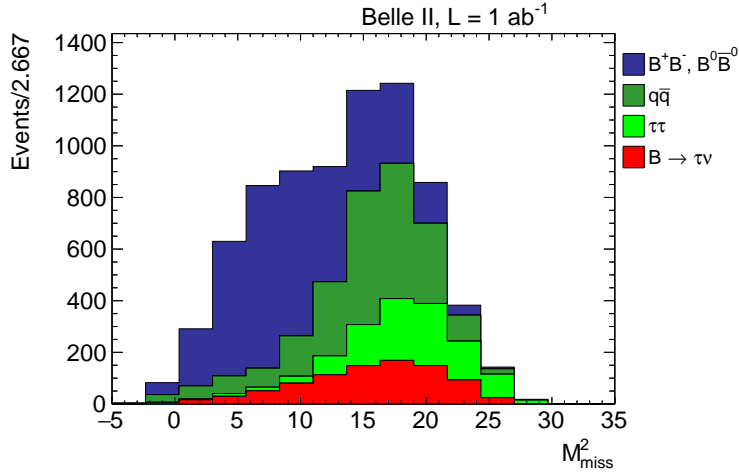


Figure 4.5: M_{miss}^2 distribution for leptonic mode for signal (red, enhanced by a factor 10), $B\bar{B}$ background (blue), continuum (green) and τ pair (light green).

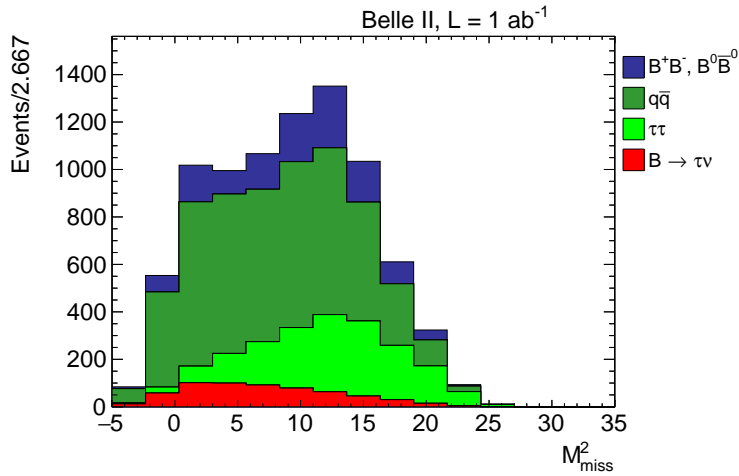


Figure 4.6: M_{miss}^2 distribution for hadronic mode for signal (red, enhanced by a factor 10), $B\bar{B}$ background (blue), continuum (green) and τ pair (light green).

For a $B\bar{B}$ event, both B mesons are produced almost at rest in the $\Upsilon(4S)$ frame, so their decay particles are isotropically distributed (uniform distribution of $\cos\theta_{Thrust}^{B\bar{B}}$ in the range $[0, 1]$). For $q\bar{q}$ events, the momenta of particles follow the direction of the jets in the event (strongly directional and collimated), and as a consequence the $\cos\theta_{Thrust}^{q\bar{q}}$ distribution is peaked at large values. To further reduce the contamination from continuum background exploiting the different topology of events (with spherical symmetry, i.e. B^+B^- , over back-to-back symmetry, i.e. $q\bar{q}$), a multivariate discriminant using Boost Decision Tree (BDT) has been trained on continuum background and signal $B \rightarrow \tau\nu$ events through the ROOT MultiVariate Analysis Toolkit (TMVA toolkit). The following weakly correlated kinematic variables are given in input:

- R_2 (Figure 4.7);
- $\cos\theta_{Thrust}$ (Figure 4.8);
- Cleo Clones, variables based on the sum of the absolute values of the momenta of all particles within angular sectors around the thrust axis in intervals of 10° resulting in 9 concentric cones (Figure 4.9);
- Super-Fox-Wolfram moments (Figure 4.10).

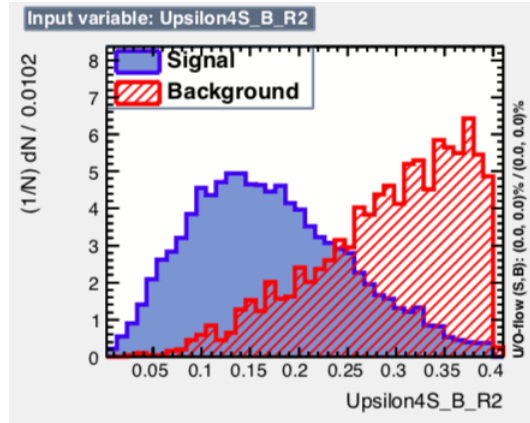


Figure 4.7: R_2 as input to the BDT. Blue histogram represents the signal and red histogram represents the background.

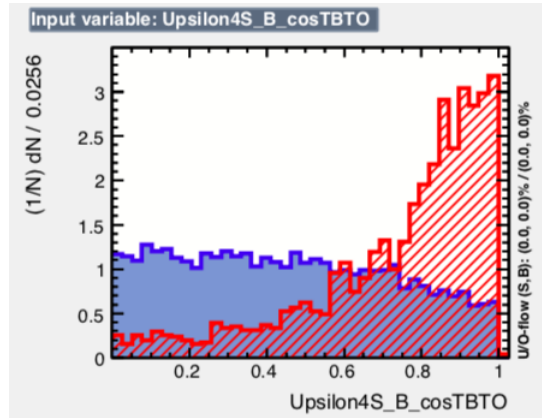


Figure 4.8: $\cos\theta_{Thrust}$ as input to the BDT. Blue histogram represents the signal and red histogram represents the background.

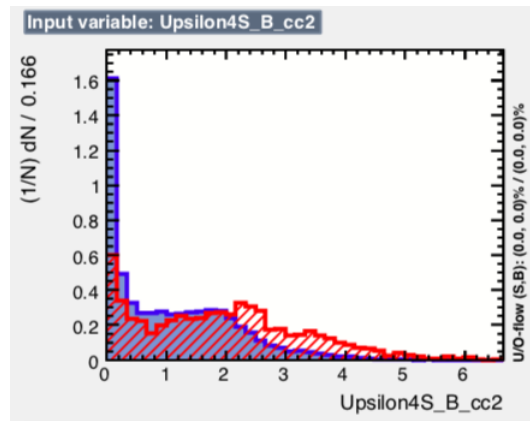


Figure 4.9: Example of Cleo Clones (02) as input to the BDT. Blue histogram represents the signal and red histogram represents the background.

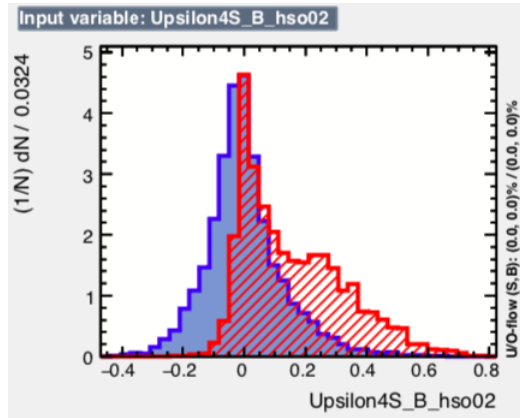


Figure 4.10: Example of Super-Fox-Wolfram moment (02) as input to the BDT. Blue histogram represents the signal and red histogram represents the background.

The output of the BDT is the multivariate discriminant, named BDT_{cont} , whose distributions for both leptonic and hadronic modes are shown in Figure 4.11 and 4.12.

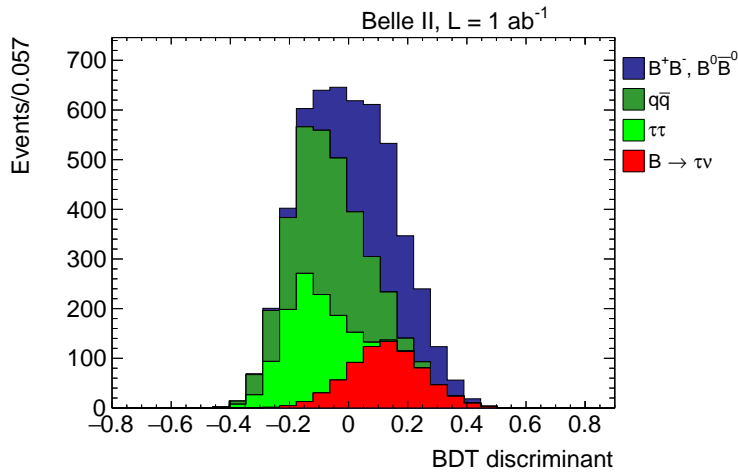


Figure 4.11: BDT_{cont} distribution for leptonic mode for signal (red, enhanced by a factor 10), $B\bar{B}$ background (blue), continuum (green) and τ pair (light green).

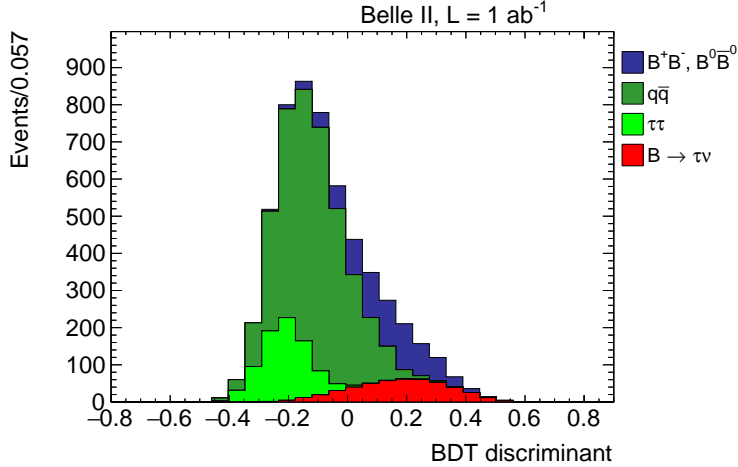


Figure 4.12: BDT_{cont} distribution for hadronic mode for signal (red, enhanced by a factor 10), $B\bar{B}$ background (blue), continuum (green) and τ pair (light green).

Leptonic and hadronic τ decay modes are trained separately, since the latter are more affected by continuum background.

Also the following variables are taken into account in the selection optimization regarding the signal region for the hadronic decay modes:

- P^* , i.e. the momentum of the charged decay product of τ lepton in the CMS frame (Figure 4.13);
- P_{miss} , i.e. the missing momentum of event (Figure 4.14);

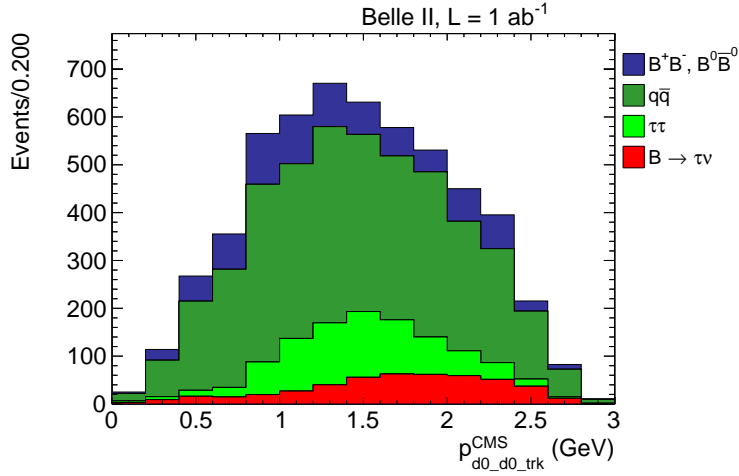


Figure 4.13: P^* distribution for hadronic mode for signal (red, enhanced by a factor 10), $B\bar{B}$ background (blue), continuum (green) and τ pair (light green).

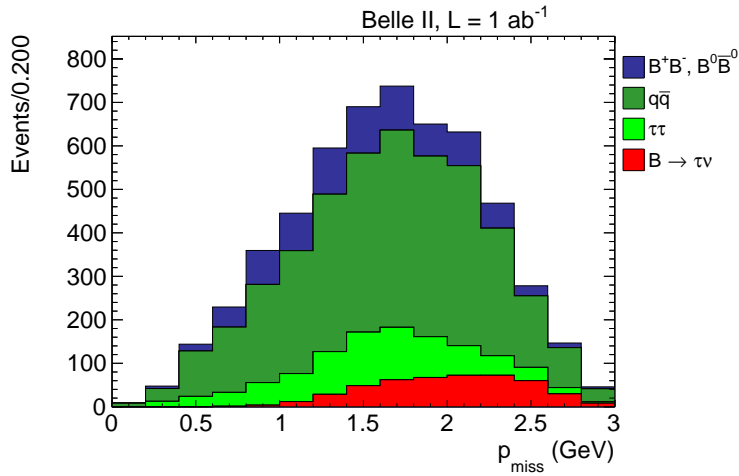


Figure 4.14: P_{miss} distribution for hadronic mode for signal (red, enhanced by a factor 10), $B\bar{B}$ background (blue), continuum (green) and τ pair (light green).

4.3 Selection optimization

The signal selection optimization is performed by cutting on the variables previously described in order to minimize a certain figure of merit (S_{L1}), which will be introduced below.

The best discriminant variable between the $B \rightarrow \tau\nu$ signal and all of the background contributions (continuum $q\bar{q}-\tau\bar{\tau}$ plus generic $B\bar{B}$ decays) is the extra energy in the electromagnetic calorimeter (E_{Extra}). E_{Extra} (Figure 4.15) is defined as the sum of the energy deposits in the calorimeter that cannot be directly associated with the reconstructed decay tree of the B_{tag} or the B_{sig} .

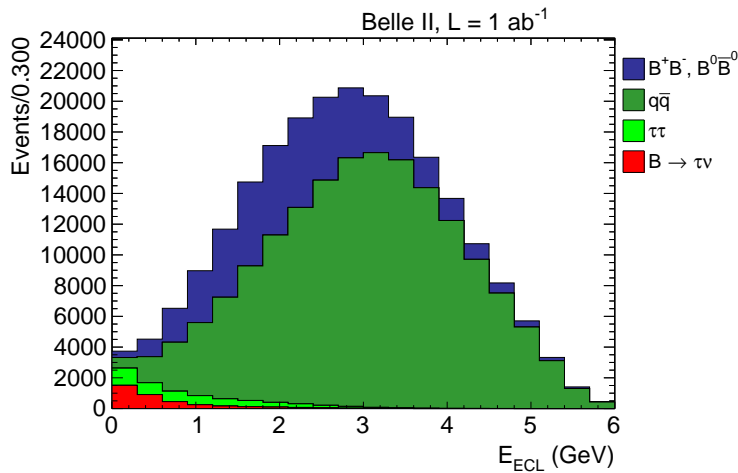


Figure 4.15: E_{Extra} distribution for signal (red, enhanced by a factor 20), $B\bar{B}$ background (blue), continuum (green) and τ pair (light green).

For signal events, E_{Extra} must be either zero or a small value arising from beam background hits and imperfect reconstruction (since neutrinos do not interact in the ECL). Moreover, most background events are distributed toward higher E_{Extra} due to the contribution from additional clusters produced by unassigned tracks and neutrals from the mis-reconstructed tag or signal B mesons. Therefore the selected window is $E_{Extra} < 1 \text{ GeV}$ (Figure 4.16 and 4.17).

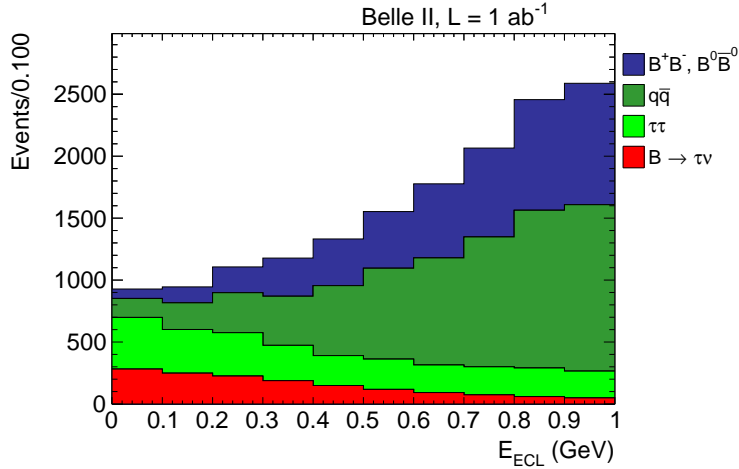


Figure 4.16: E_{Extra} distribution for signal (red, enhanced by a factor 10), $B\bar{B}$ background (blue), continuum (green) and τ pair (light green) in the $E_{Extra} < 1 \text{ GeV}$ window.

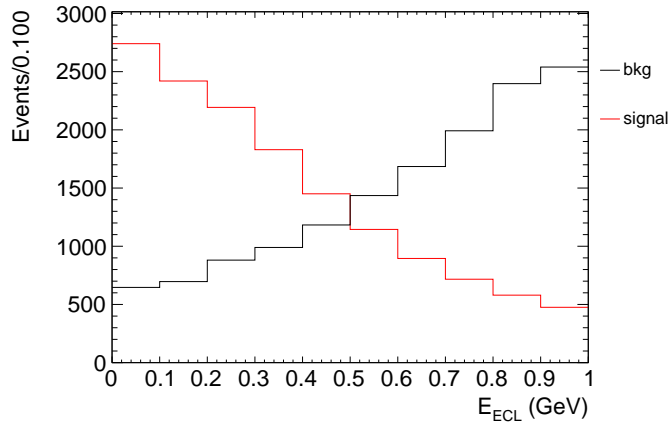


Figure 4.17: Comparison between E_{Extra} shapes for both signal (scaled to background histogram integral) and background in the $E_{Extra} < 1 \text{ GeV}$ window.

For each step of the selection optimization, a *toy-MC* study is performed:

20000 pseudo-experiments are produced and for each of them a certain pseudo-dataset is generated according to the signal and background MC expectations, with Poisson fluctuations. An extended binned maximum likelihood fit to E_{Extra} distribution is performed using a two-component parameterized function, in which the E_{Extra} distributions for signal and background events are taken from simulation, in order to extract the signal (N_S) and background (N_B) yields with their respective errors (σ_S and σ_B). By means of this procedure, for each step it is possible to calculate the value of the FOM [28]:

$$S_{L1} = \frac{\sigma_S}{N_S} \quad (4.3)$$

where N_S is the average value of the signal yield distribution and σ_S is the average value of the error on the signal yield distribution for each selection cut set of values. S_{L1} is the relative statistical uncertainty on the signal yield.

Starting from the above selection criteria on M_{bc} , M_{miss}^2 and E_{Extra} , the first cut to be optimized is the one on the $SigProb$ variable. Figure 4.18 shows that the minimum value of S_{L1} is reached for:

- $SigProb > 0.015$.

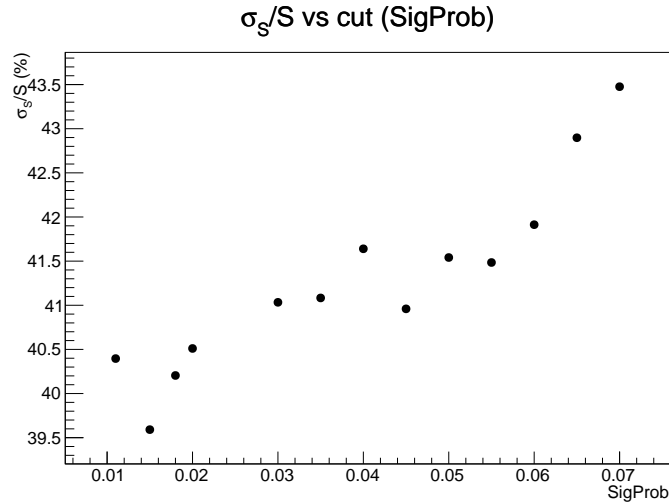


Figure 4.18: Plot of S_{L1} as a function of cut on $SigProb$.

The results of this specific toy MC study are shown in Figures 4.19-4.20-4.21.

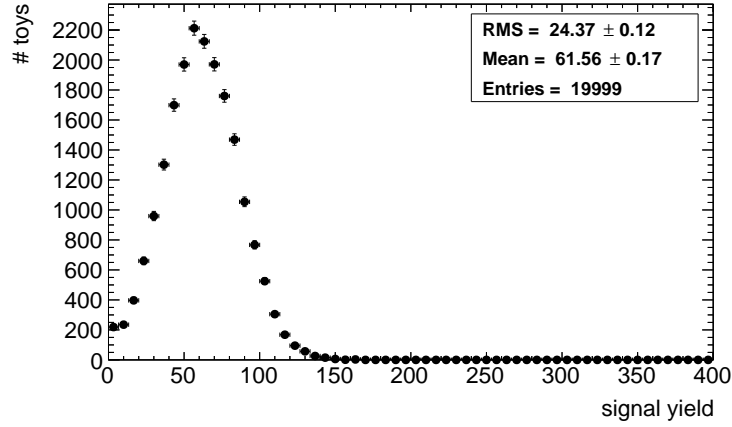


Figure 4.19: Signal yield distribution after 20000 pseudo-experiments (with the condition $SigProb > 0.015$).

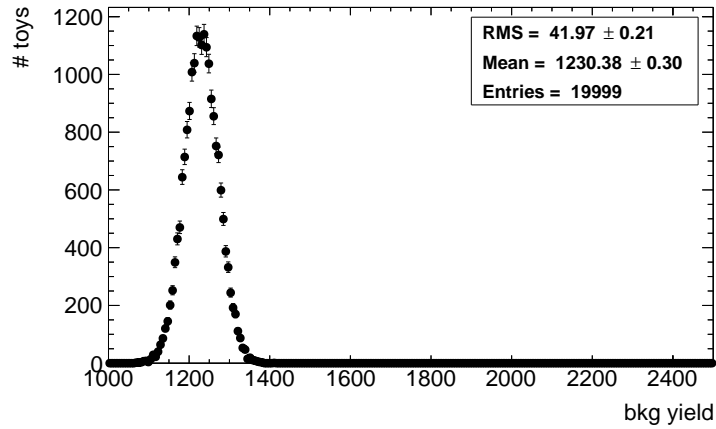


Figure 4.20: Background yield distribution after 20000 pseudo-experiments (with the condition $SigProb > 0.015$).

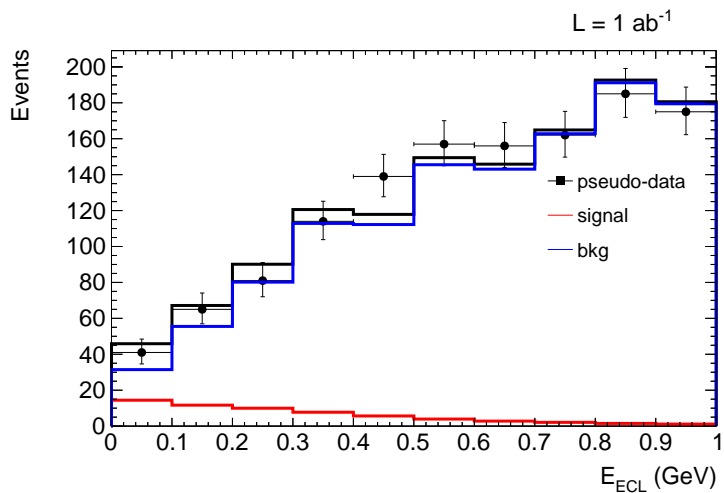


Figure 4.21: Extended maximum likelihood fit to pseudo-data E_{Extra} distribution as a result of a toy experiment (with the condition $SigProb > 0.015$). The red and blue histograms represent the signal and background fit functions (templates from simulation). The black histogram is the result of fit.

Subsequently the BDT_{cont} is optimized separately for the leptonic and hadronic modes (Figure 4.22 and 4.23). The selected cuts are:

- $(BDT_{cont})_{lep} > 0.06$;
- $(BDT_{cont})_{had} > 0.10$.

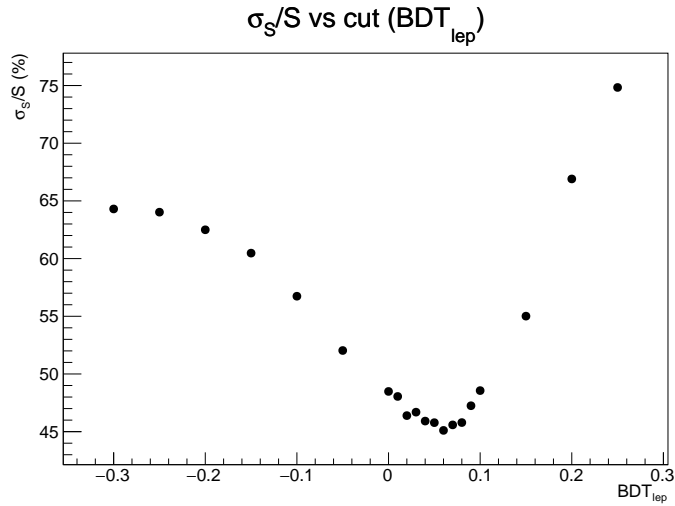


Figure 4.22: Plot of S_{L1} as a function of cut on $(BDT_{cont})_{lep}$.

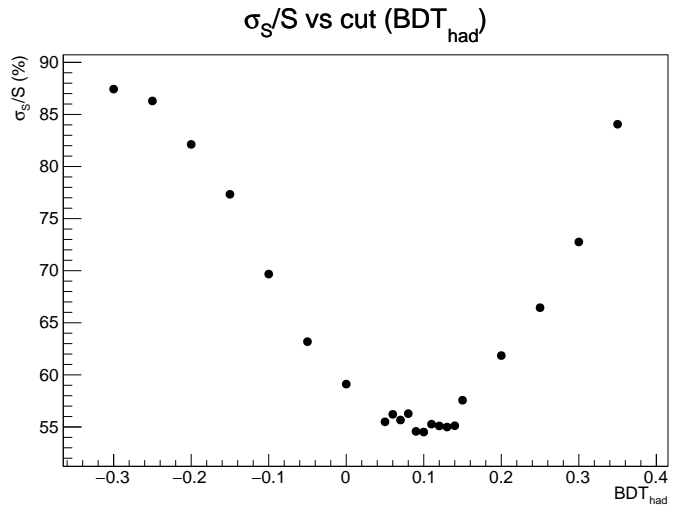


Figure 4.23: Plot of S_{L1} as a function of cut on $(BDT_{cont})_{had}$.

At this stage, the optimization on these variables is repeated again to check if the chosen cuts on the BDT_{cont} can affect the selection on $SigProb$. The results are shown in Figure 4.24 for $SigProb$, in Figure 4.25 for $(BDT_{cont})_{lep}$ and in Figure 4.26 for $(BDT_{cont})_{had}$. Therefore the selected cuts are:

- $SigProb > 0.026$;
- $(BDT_{cont})_{lep} > 0.06$;
- $(BDT_{cont})_{had} > 0.05$.

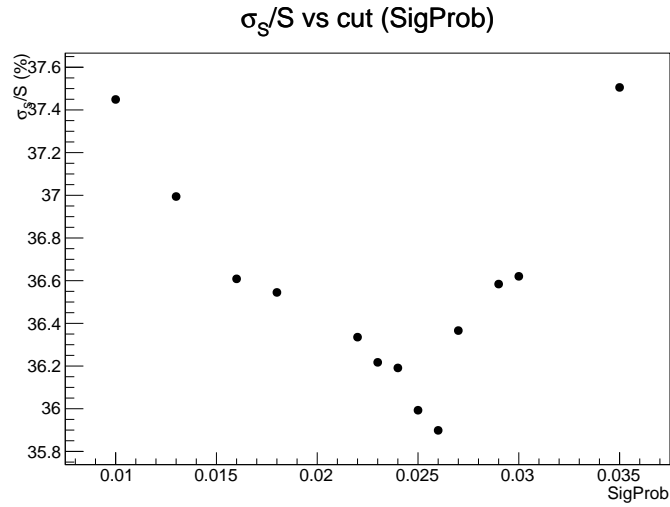


Figure 4.24: Plot of S_{L1} as a function of cut on $SigProb$.

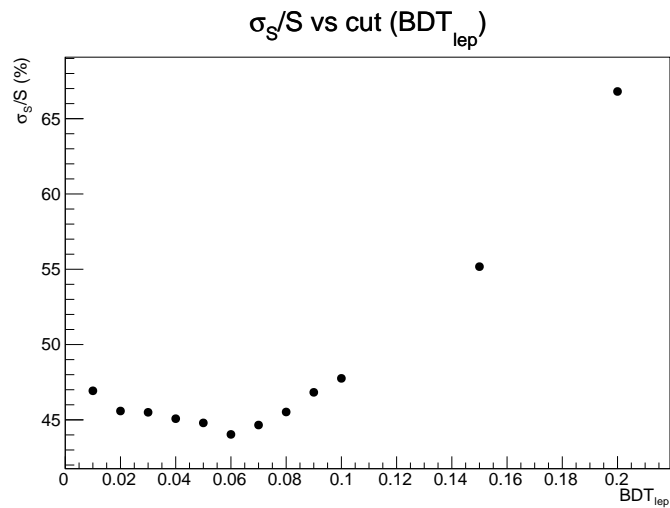


Figure 4.25: Plot of S_{L1} as a function of cut on $(BDT_{cont})_{lep}$.

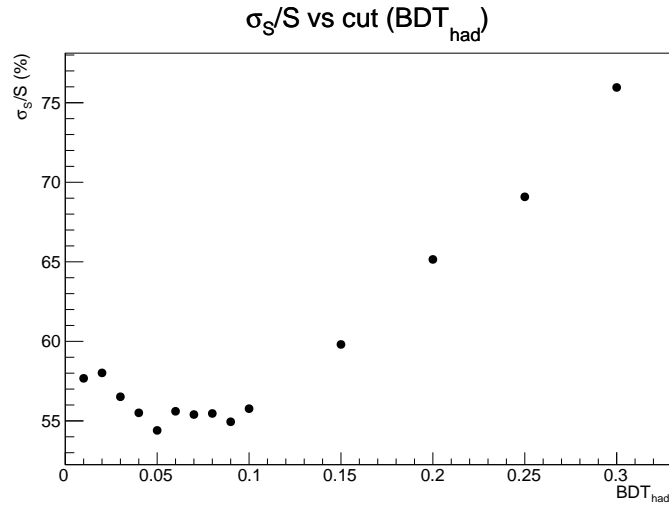


Figure 4.26: Plot of S_{L1} as a function of cut on $(BDT_{cont})_{lep}$.

The next step has been to optimize the selection first for the P^* and then for P_{miss} variables for the hadronic decay modes. The values that minimize S_{L1} are:

- $P^* > 0.4 \text{ GeV}/c$ (Figure 4.27);
- $P_{miss} > 0.6 \text{ GeV}/c$ (Figure 4.28).

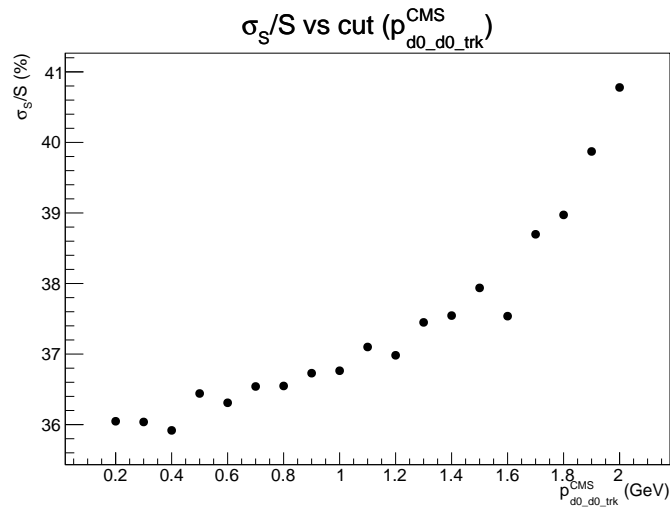


Figure 4.27: Plot of S_{L1} as a function of cut on P^* .

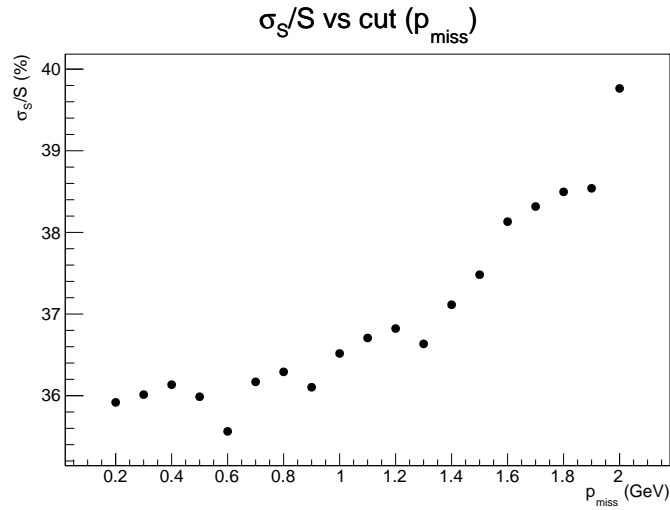


Figure 4.28: Plot of S_{L1} as a function of cut on P_{miss} .

Therefore the signal region is identified by the following overall selection:

	Leptonic	Hadronic	All
M_{bc} (GeV)			> 5.27
M_{miss}^2 (GeV ² /c ⁴)	> 10	< 12	
$SigProb$			> 0.026
BDT_{cont}	> 0.06	> 0.05	
P^* (GeV/c)		> 0.4	
P_{miss} (GeV/c)		> 0.6	
E_{Extra} (GeV)			< 1

Table 4.3: Final selection of the signal region.

The E_{Extra} distribution after applying all selection criteria is shown in Figure 4.29.

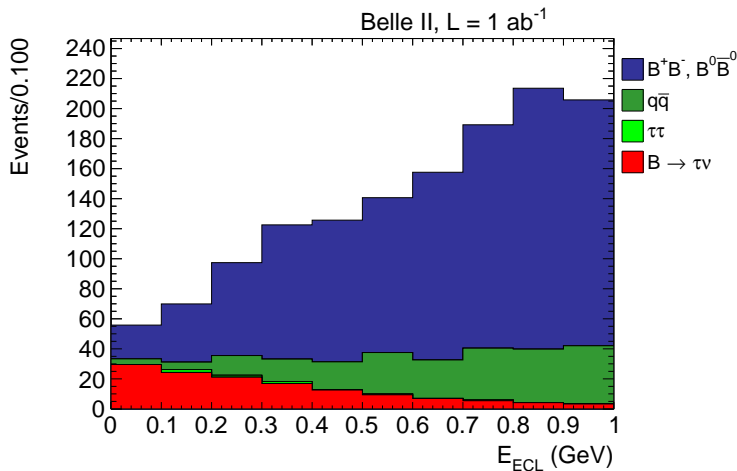


Figure 4.29: E_{Extra} distribution after applying all selection criteria for signal (red, enhanced by a factor 2), $B\bar{B}$ background (blue), continuum (green) and τ pair (light green).

4.4 Signal Cross Feeds

After the event selection, events may be found to be reconstructed from a τ decay mode different with respect to the mode generated (*cross feed*). The E_{Extra} distributions for signal MC sample for all the reconstructed τ modes

showing the different true τ decay mode are shown in Figures 4.30-4.31-4.32-4.33.

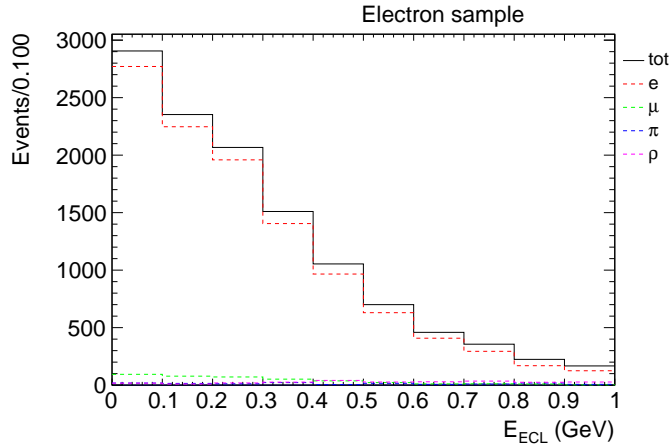


Figure 4.30: E_{Extra} distribution for the e^- mode with reconstructed signal (red) and cross feeds (green, blue and magenta). The black histogram is the sum of them.

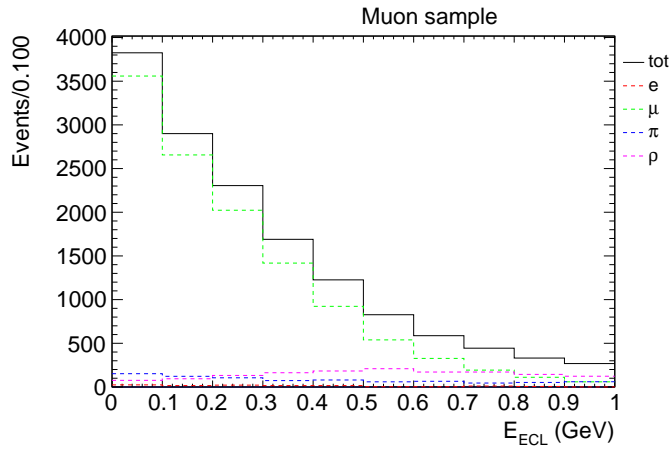


Figure 4.31: E_{Extra} distribution for the μ^- mode with reconstructed signal (green) and cross feeds (red, blue and magenta). The black histogram is the sum of them.

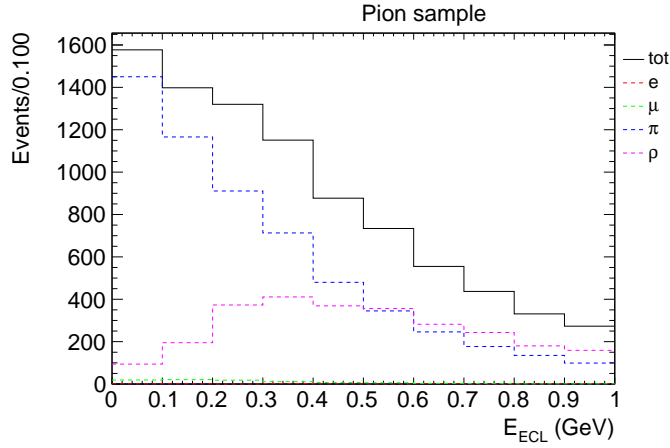


Figure 4.32: E_{Extra} distribution for the π^- mode with reconstructed signal (blu) and cross feeds (red, green and magenta). The black histogram is the sum of them.

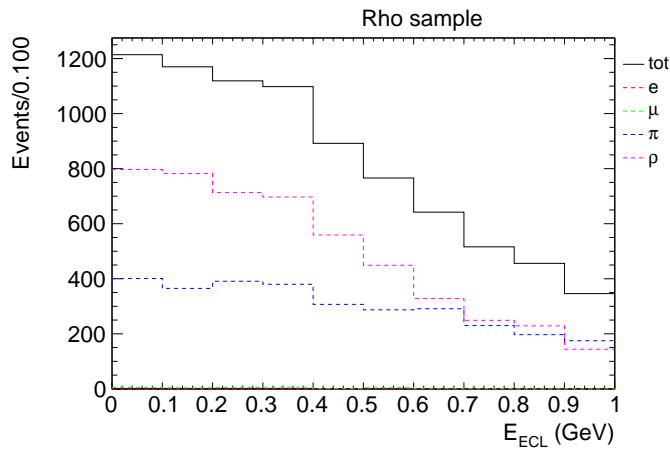


Figure 4.33: E_{Extra} distribution for the $\pi^- \pi^0$ mode with reconstructed signal (magenta) and cross feeds (red, green and blue). The black histogram is the sum of them.

The summary with the efficiencies and cross feeds is illustrated in Table 4.4.

Signal τ mode	Type	Fraction (%)
$e^- \bar{\nu}_e \nu_\tau$	correctly-reconstructed	93.0
	$\mu^- \bar{\nu}_\mu \nu_\tau$	3.3
	$\pi^- \nu_\tau$	1.1
	$\rho^- \nu_\tau$	2.2
	cross feeds	6.6
	other	0.4
$\mu^- \bar{\nu}_\mu \nu_\tau$	correctly-reconstructed	82.0
	$e^- \bar{\nu}_e \nu_\tau$	0.8
	$\pi^- \nu_\tau$	5.6
	$\rho^- \nu_\tau$	10.2
	cross feeds	16.6
	other	1.4
$\pi^- \nu_\tau$	correctly-reconstructed	66.1
	$e^- \bar{\nu}_e \nu_\tau$	0.1
	$\mu^- \bar{\nu}_\mu \nu_\tau$	1.0
	$\rho^- \nu_\tau$	30.8
	cross feeds	31.9
	other	2
$\rho^- \nu_\tau$	correctly-reconstructed	60.2
	$e^- \bar{\nu}_e \nu_\tau$	0.005
	$\mu^- \bar{\nu}_\mu \nu_\tau$	0.3
	$\pi^- \nu_\tau$	36.8
	cross feeds	37.2
	other	2.6

Table 4.4: Summary of correctly-reconstructed efficiencies and cross feeds.

4.5 Expected number of signal events and statistical significance

At this stage, the signal selection efficiency (ratio between the number of events passing the selection and the number of $B\bar{B}$ pairs generated in the signal MC sample) is evaluated for each of the four τ decay modes. An example of fit to E_{Extra} distribution for a single toy experiment is shown in the set of Figures 4.34-4.35-4.36-4.37-4.38.

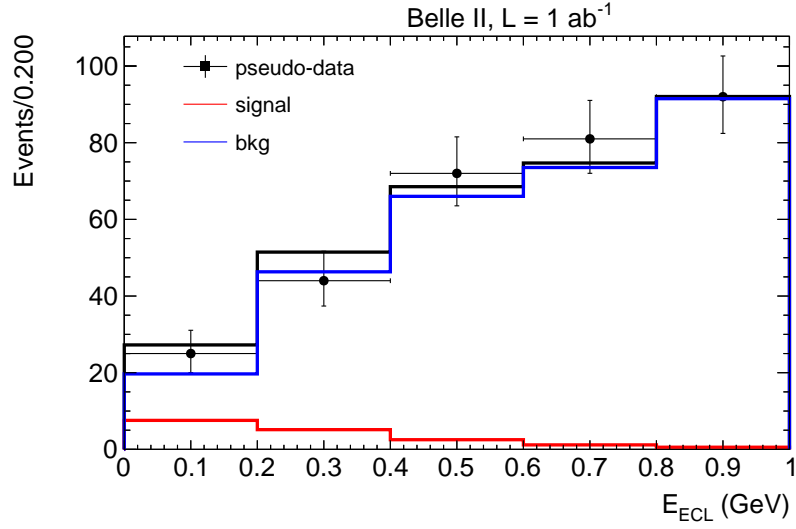


Figure 4.34: Extended maximum likelihood fit to E_{Extra} distribution as a result of a toy experiment for the $\tau^- \rightarrow e^- \bar{\nu}_e \nu_\tau$ mode.

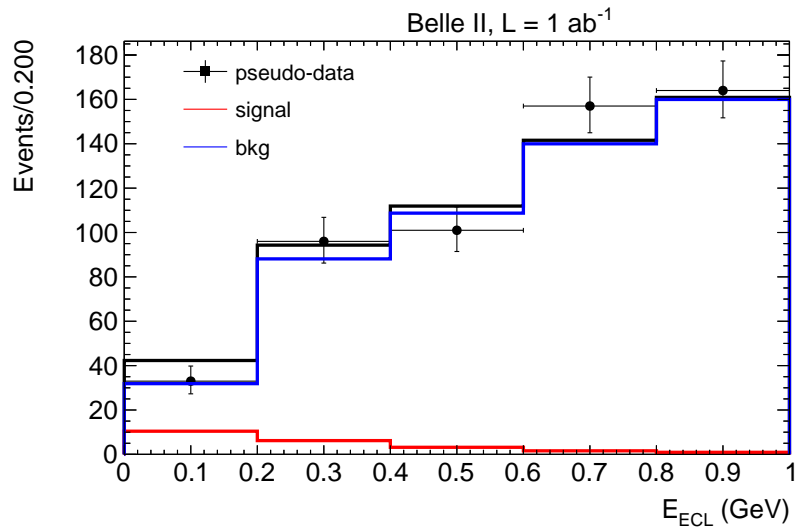


Figure 4.35: Extended maximum likelihood fit to E_{Extra} distribution as a result of a toy experiment for the $\tau^- \rightarrow \mu^- \bar{\nu}_\mu \nu_\tau$ mode.

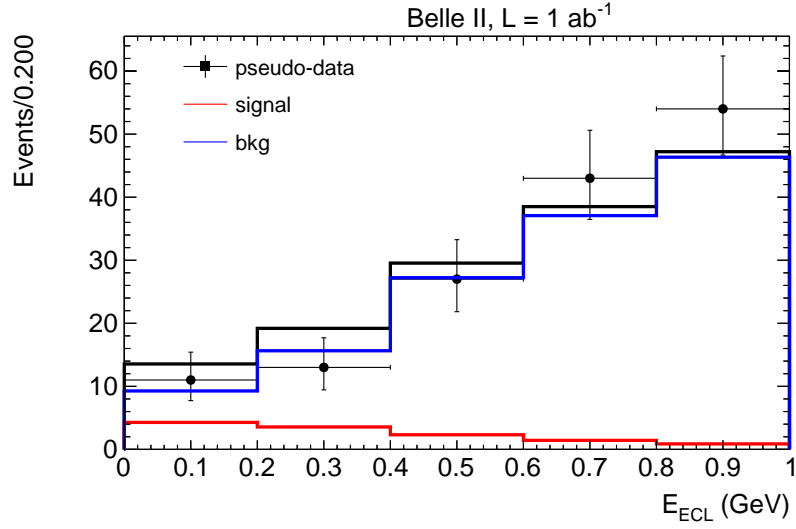


Figure 4.36: Extended maximum likelihood fit to E_{Extra} distribution as a result of a toy experiment for the $\tau^- \rightarrow \pi^- \nu_\tau$ mode.

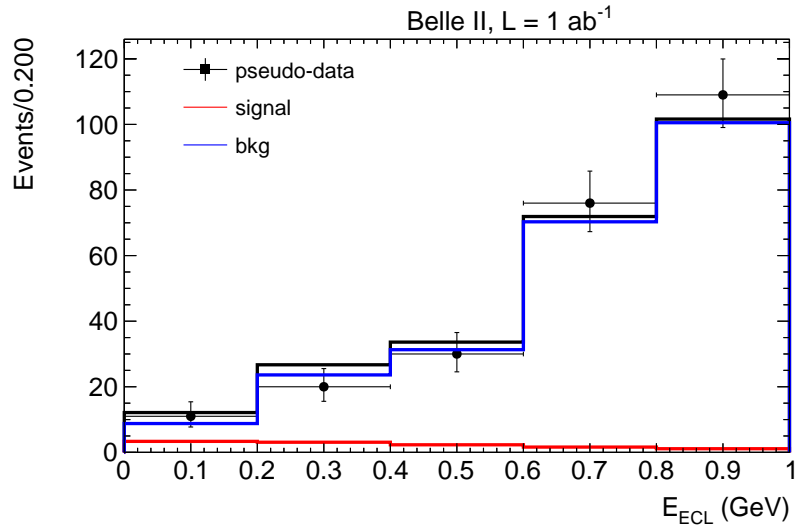


Figure 4.37: Extended maximum likelihood fit to E_{Extra} distribution as a result of a toy experiment for the $\tau^- \rightarrow \pi^- \pi^0 \nu_\tau$ mode.

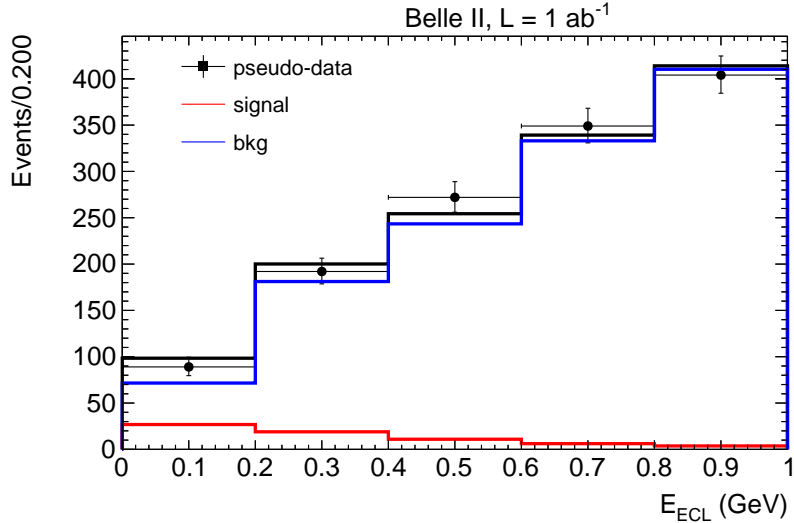


Figure 4.38: Extended maximum likelihood fit to E_{Extra} distribution as a result of a toy experiment for all of the four τ 1-prong decay modes.

The signal selection efficiencies and the average signal yields resulting from 20000 toy experiments corresponding to the four τ decay modes are summarized in Table 4.5.

Mode	ϵ_{sel}	N_S	S_{L1}
$\tau^- \rightarrow e^- \bar{\nu}_e \nu_\tau$	1.49×10^{-4}	18.8 ± 11.5	61.1%
$\tau^- \rightarrow \mu^- \bar{\nu}_\mu \nu_\tau$	1.81×10^{-4}	22.8 ± 13.2	57.9%
$\tau^- \rightarrow \pi^- \nu_\tau$	1.09×10^{-4}	14.3 ± 9.6	67.1%
$\tau^- \rightarrow \pi^- \pi^0 \nu_\tau$	1.06×10^{-4}	14.3 ± 10.7	74.8%
all	5.42×10^{-4}	66.9 ± 23.8	35.5%

Table 4.5: Selection efficiencies, average signal yields and statistical uncertainties resulting from 20000 toy experiments corresponding to the four τ 1-prong decay modes.

A high-statistics sample of pseudo-experiments (10^6) are generated in order to estimate the expected significance of the branching ratio measurement according to the following procedure [28, 29]: a likelihood ratio test statistic $Q = L(S + B)/L(B)$ is defined and the test statistic $\sqrt{2 \ln \left(\frac{L(S+B)}{L(B)} \right)}$ is

evaluated on pseudo-datasets sampled from signal plus background ($S + B$) and background (B) only E_{Extra} distributions (Figure 4.39). The confidence level of the background null hypothesis is evaluated as the ratio between the number of pseudo-experiments which give a value of Q greater than the expected test statistics for a $S + B$ hypothesis and the total number of pseudo-experiments:

$$CL_B = \frac{N_{Q_B > Q_{S+B}}}{N}. \quad (4.4)$$

The statistical significance is related to CL_B as follow:

$$N_\sigma = \sqrt{2} \text{Erf}^{-1}(2CL_B - 1), \quad (4.5)$$

where Erf is the error function.

The expected statistical significance is:

$$(3.04 \pm 0.01) \sigma.$$

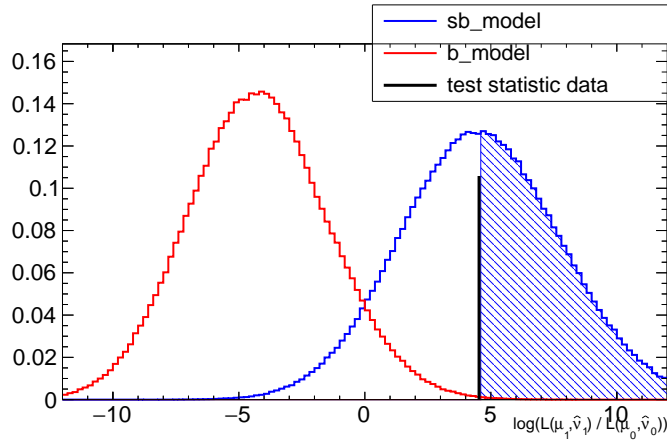


Figure 4.39: Hypothesis test for the expected statistical significance.

4.6 Expected systematic uncertainties

The systematic uncertainty on $B \rightarrow \tau\nu$ branching ratio measurement with an integrated luminosity of 1 ab^{-1} is estimated to be $\sim 13\%$, based on a scaling of the uncertainties of the Belle measurement with hadronic tag method [30]. The main sources of systematic uncertainties are the signal and background E_{Extra} PDFs, the uncertainty on the relative contributions from B decays that peak near zero E_{Extra} (i.e. peaking background), the tagging efficiency, K_L^0 veto efficiency and minor uncertainties due to the number of $B\bar{B}$ pairs, the signal efficiency (PID efficiency, τ branching ratios, π^0 efficiency and tracking efficiency), and MC samples used for background PDFs. The uncertainties on PDFs and tagging efficiency are limited by statistical precision in the $B \rightarrow D^{*0}l\nu$ control sample on data and so are expected to scale with luminosity similarly to the statistical uncertainty (i.e. as $1/\sqrt{L}$). The uncertainty on the signal efficiency is expected to scale with luminosity as in the case of the statistical uncertainty.

4.7 Projections

The results and projections of the uncertainties on the branching ratio measurement and the expected statistical significances with 1, 3, 5, 10, 20, 30 and 50 ab^{-1} using the hadronic tagging are summarized in Table 4.6.

Luminosity (ab^{-1})	1	3	5	10	20	30	50
Statistical uncertainty (%)	35.5	20.8	16.1	11.3	8.1	6.6	5.1
Systematic uncertainty (%)	12.7	8.1	6.8	5.7	5.1	4.8	4.6
Total uncertainty (%)	37.7	22.3	17.5	12.7	9.5	8.2	6.9
Statistical significance (σ)	3.0	4.8	6.2	8.8	12.4	15.2	19.8

Table 4.6: Expected uncertainties and statistical significances on the $B \rightarrow \tau\nu$ branching ratio measurement for different luminosity scenarios with hadronic tag method.

The plots of the statistical uncertainty and the statistical significance as functions of integrated luminosity are shown in Figure 4.40 and 4.41.

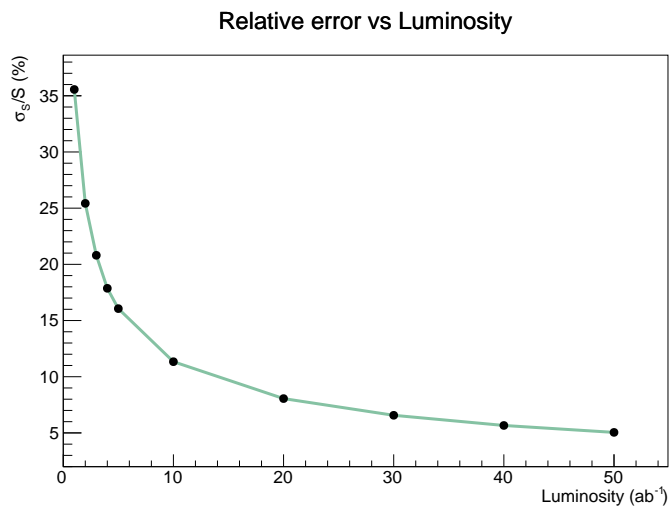


Figure 4.40: Plot of statistical uncertainty as a function of integrated luminosity.

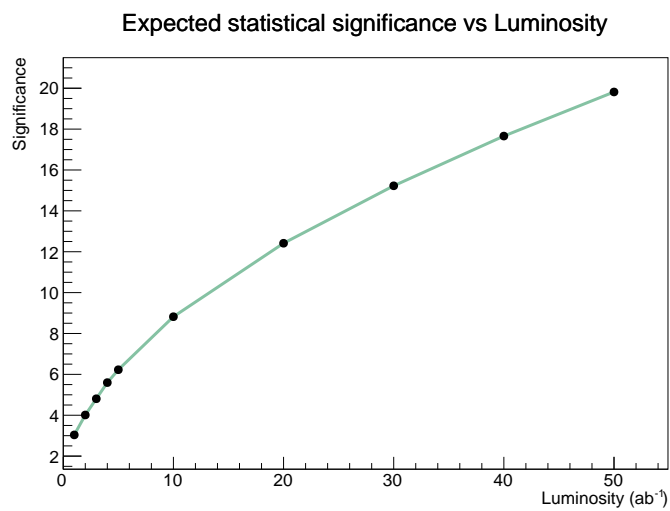


Figure 4.41: Plot of statistical significance as a function of integrated luminosity.

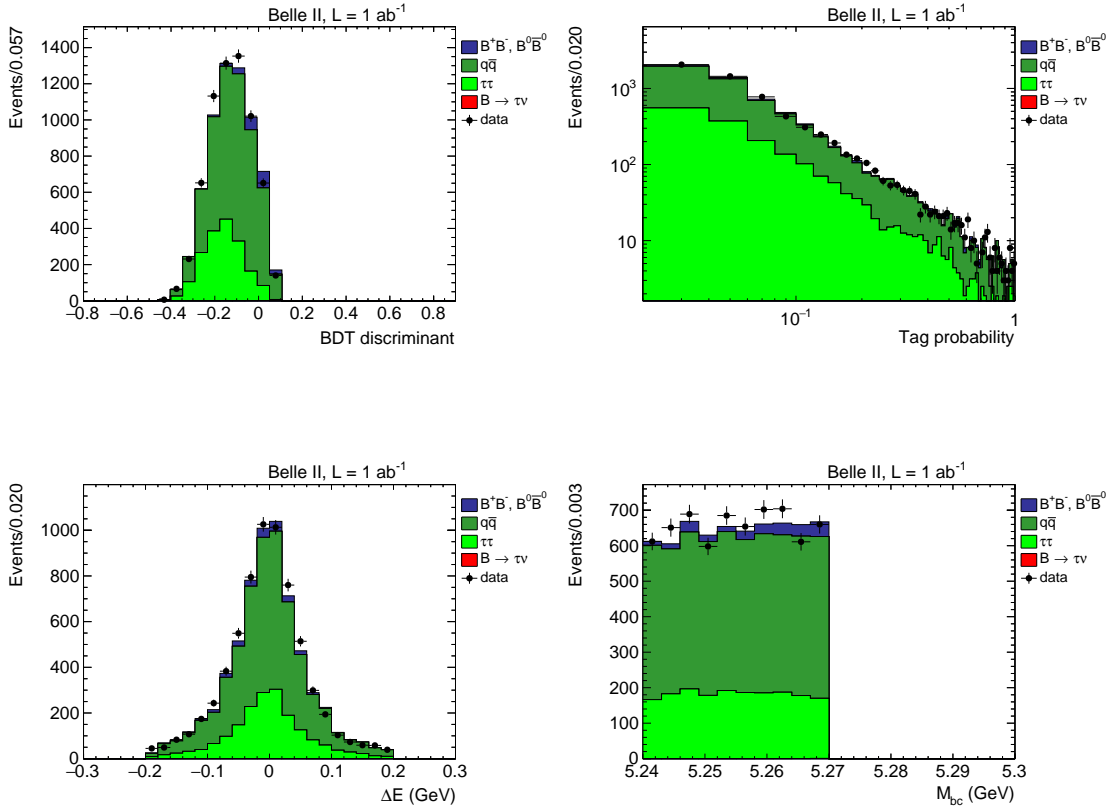
The luminosity needed to reach a 5σ discovery of $B \rightarrow \tau\nu$ is about $3.2 ab^{-1}$.

4.8 Data-MonteCarlo agreement

Before to extract the signal yield after the optimization of the overall selection, it is important to compare the distributions for both data and MC in regions where the signal contribution is negligible in order to check if the simulation well describes the real physics scenario, and otherwise to find out which type of contribution is the mostly source of discrepancies.

The agreement is evaluated in the two following different regions of the phase space:

- M_{bc} sideband, obtained inverting the cuts on M_{bc} itself and on $(BDT_{cont})_{lep}$ and $(BDT_{cont})_{had}$, in which the continuum background dominates (Figure 4.42);



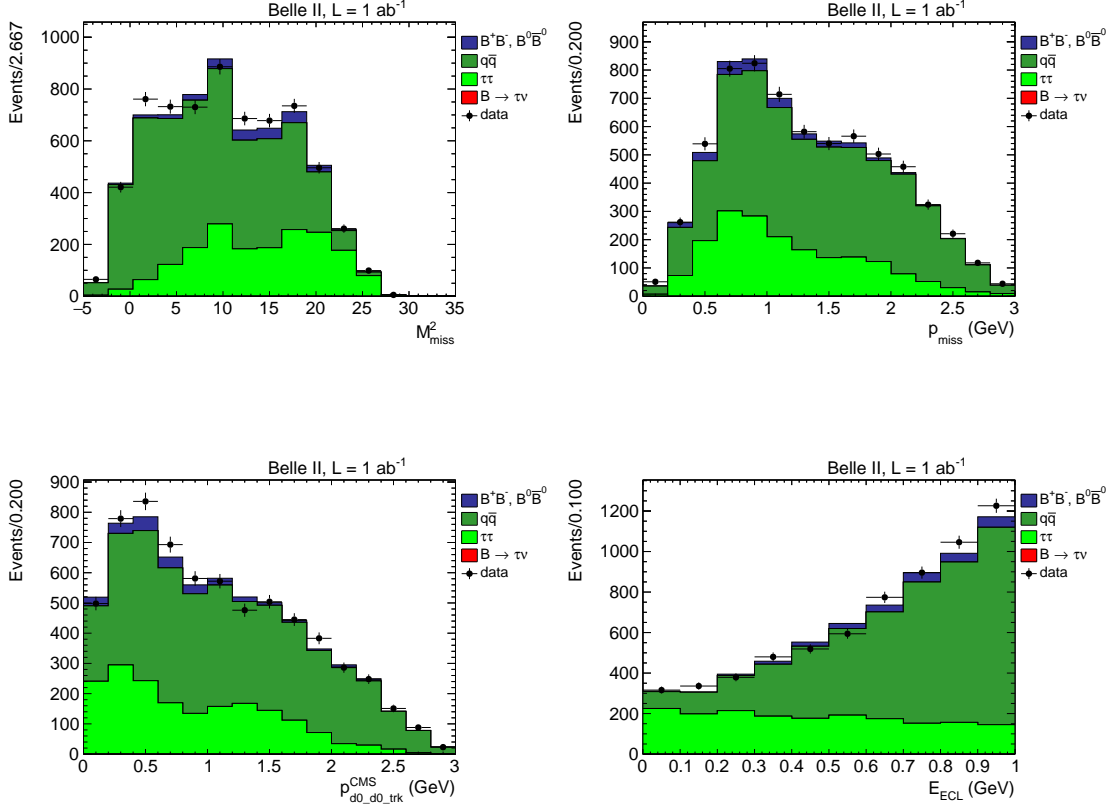
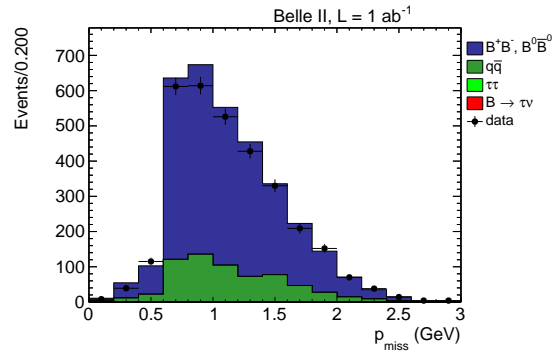
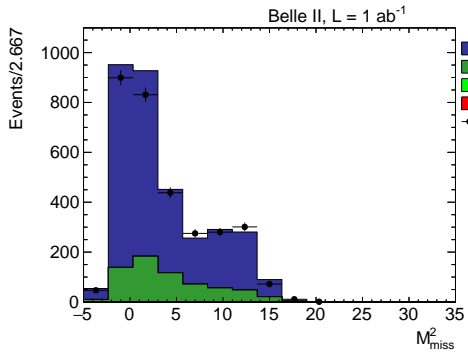
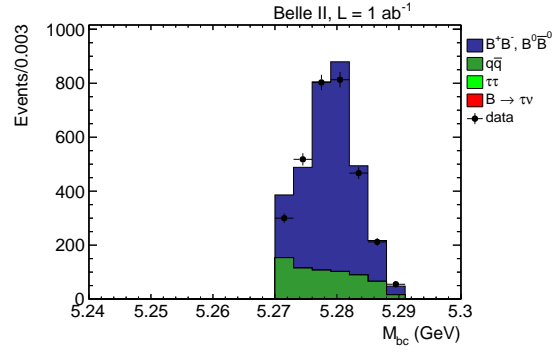
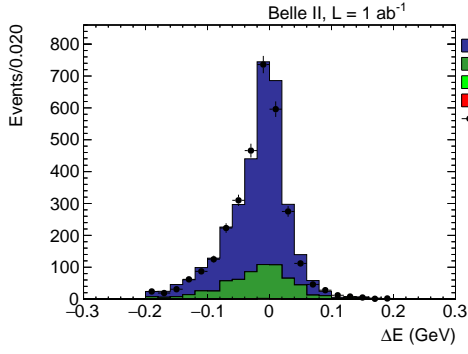
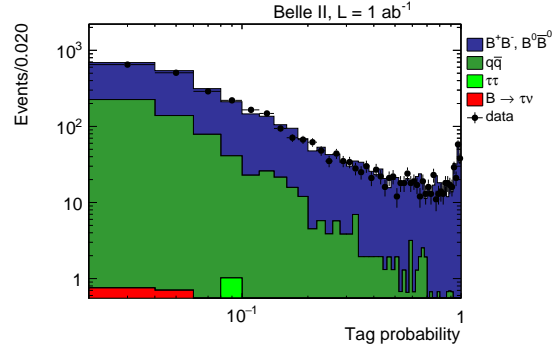
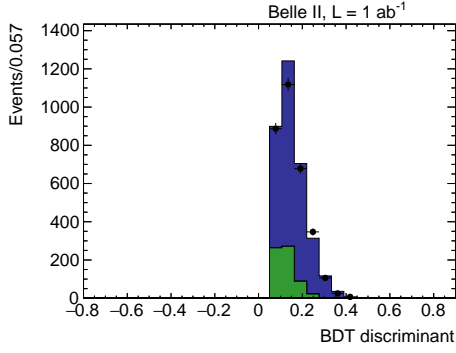


Figure 4.42: Data/MC agreement in the M_{bc} sideband for BDT_{cont} , $SigProb$, ΔE , M_{bc} , M_{miss}^2 , P_{miss} , P^* , E_{Extra} distributions for $B\bar{B}$ background (blue), continuum (green), τ pair (light green) and data (dots).

- E_{Extra} sideband, obtained selecting $E_{Extra} > 1$ GeV, in which the generic $B\bar{B}$ is expected to dominate, although there is contamination from continuum background (Figure 4.43).



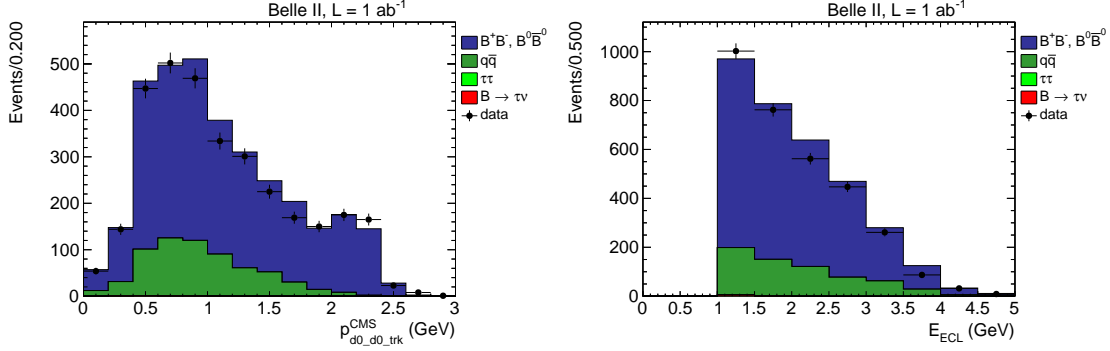


Figure 4.43: Data/MC agreement in the E_{Extra} sideband for BDT_{cont} , $SigProb$, ΔE , M_{bc} , M_{miss}^2 , P_{miss} , P^* , E_{Extra} distributions for $B\bar{B}$ background (blue), continuum (green), τ pair (light green) and data (dots).

The overall agreements are good.

4.9 Signal extraction and branching ratio measurement on data-challenge sample

The number of signal events on data-challenge sample is extracted following the same procedure, i.e. by performing an extended binned maximum likelihood fit to the E_{Extra} distribution (in which the signal and background yields are set as free parameters) for all of the four τ decay modes first separately and then merged in a single histogram. The resulting histograms of fits are shown in Figures 4.44 for e^- mode, in 4.45 for μ^- mode, in 4.46 for π^- mode, in 4.47 for $\pi^-\pi^0$ mode and in 4.48 for all of the four τ 1-prong decay modes.

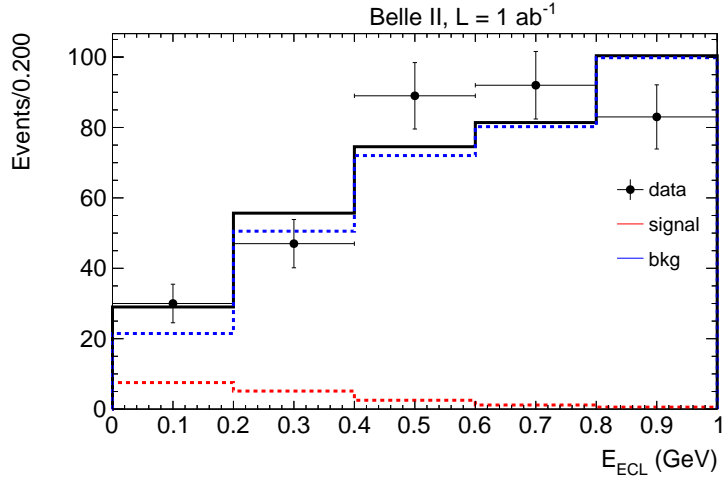


Figure 4.44: Extended maximum likelihood fit to $E_{E_{extra}}$ distribution on data-challenge sample for the $\tau^- \rightarrow e^- \bar{\nu}_e \nu_\tau$ mode.

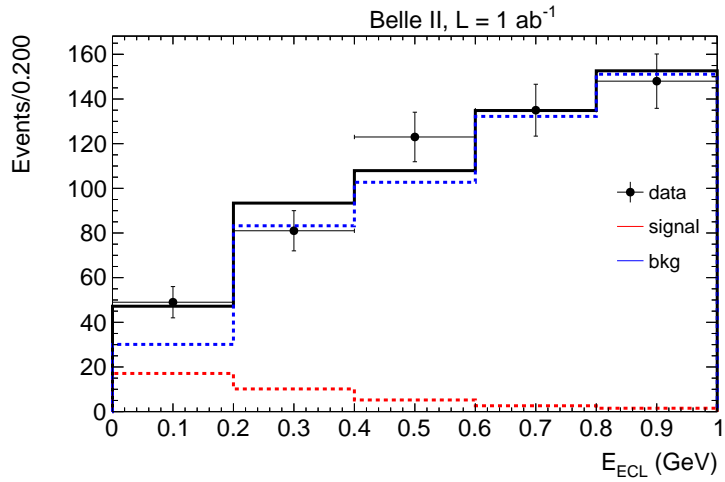


Figure 4.45: Extended maximum likelihood fit to $E_{E_{extra}}$ distribution on data-challenge sample for the $\tau^- \rightarrow \mu^- \bar{\nu}_\mu \nu_\tau$ mode.

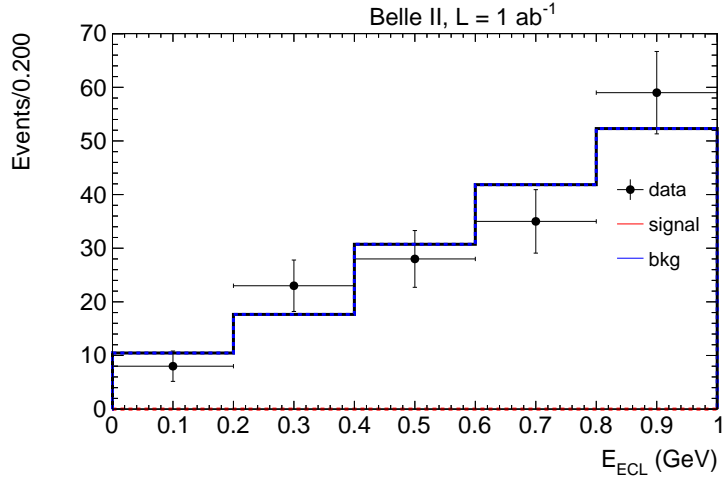


Figure 4.46: Extended maximum likelihood fit to E_{Extra} distribution on data-challenge sample for the $\tau^- \rightarrow \pi^- \nu_\tau$ mode.

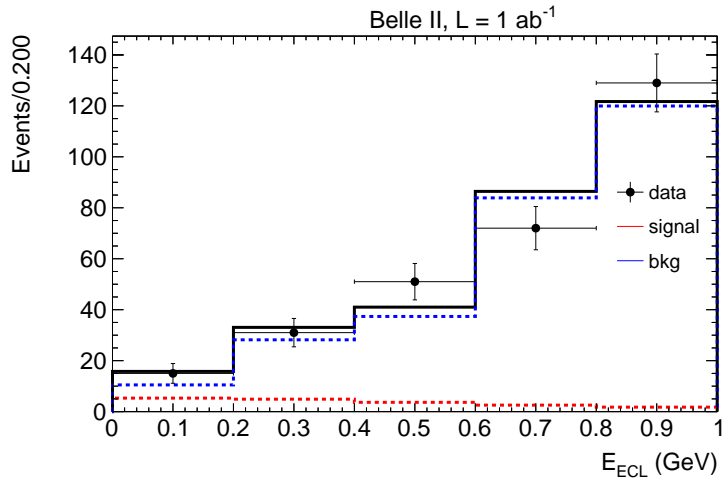


Figure 4.47: Extended maximum likelihood fit to E_{Extra} distribution on data-challenge sample for the $\tau^- \rightarrow \pi^- \pi^0 \nu_\tau$ mode.

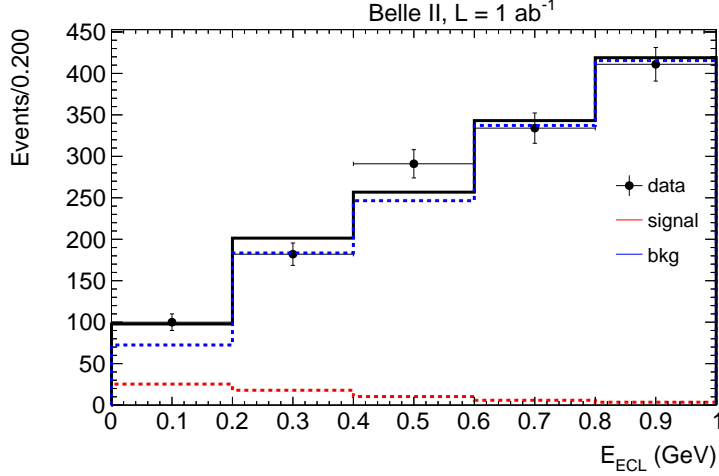


Figure 4.48: Extended maximum likelihood fit to E_{Extra} distribution on data-challenge sample for all of the four τ 1-prong decay modes.

The branching ratio is calculated as:

$$\mathcal{B}(B \rightarrow \tau\nu) = \frac{N_S}{2\sigma(e^+e^- \rightarrow B^+B^-) \cdot L_{int} \cdot \epsilon_{sel}} \quad (4.6)$$

where $N_{B^+B^-} = \sigma(e^+e^- \rightarrow B^+B^-) \cdot L_{int} = 565 \times 10^6$ is the number of B^+B^- pairs generated at $1ab^{-1}$ of integrated luminosity and ϵ_{sel} is the signal selection efficiency (Table 4.5).

The extracted signal yields and measured branching ratios are listed in Table 4.7.

Mode	Signal Yield	$\mathcal{B}(B \rightarrow \tau\nu)$
$\tau^- \rightarrow e^- \bar{\nu}_e \nu_\tau$	16.9 ± 12.1	$(0.96 \pm 0.69) \times 10^{-4}$
$\tau^- \rightarrow \mu^- \bar{\nu}_\mu \nu_\tau$	36.5 ± 14.8	$(1.66 \pm 0.68) \times 10^{-4}$
$\tau^- \rightarrow \pi^- \nu_\tau$	0	0
$\tau^- \rightarrow \pi^- \pi^0 \nu_\tau$	18.1 ± 12.5	$(1.57 \pm 0.97) \times 10^{-4}$
global	62.9 ± 24.9	$(0.94 \pm 0.37) \times 10^{-4}$

Table 4.7: Signal yields resulting from extended binned maximum likelihood fits on E_{Extra} distributions on data-challenge sample and measured branching ratio corresponding to the four τ 1-prong decay modes.

Regarding the merged category, the measured branching ratio is:

$$\mathcal{B}(B \rightarrow \tau\nu)_{global} = (1.0 \pm 0.4) \times 10^{-4},$$

with a statistical significance of:

$$(2.69 \pm 0.01) \sigma.$$

Subsequently, assuming the signal yield for the i -th category as:

$$S_i = B \sum_j \epsilon_{ij} \mathcal{B}(\tau \rightarrow j), \quad (4.7)$$

where B is the common parameter $\mathcal{B}(B \rightarrow \tau\nu)$ among the four τ decay modes and ϵ_{ij} are the efficiencies and cross feeds listed in Table 4.4, a simultaneous extended maximum likelihood fit to E_{Extra} distributions is performed. The resulting histograms of simultaneous fit are shown in Figures 4.49 for e^- mode, in 4.50 for μ^- mode, in 4.51 for π^- mode and in 4.52 for $\pi^-\pi^0$ mode.

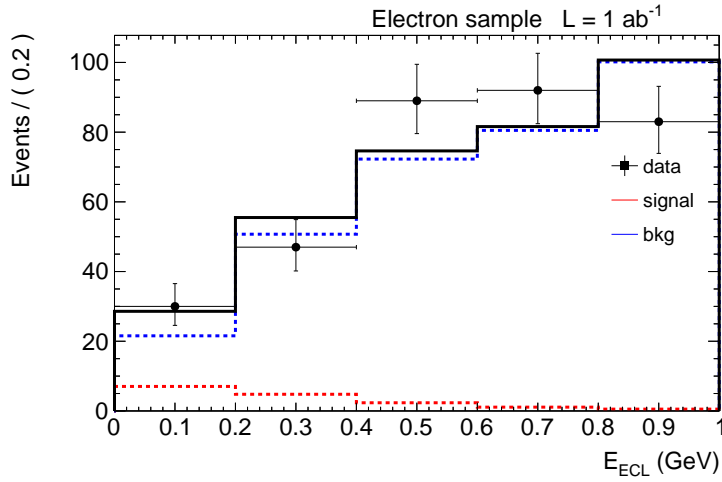


Figure 4.49: Simultaneous fit to E_{Extra} distribution on data-challenge sample for the $\tau^- \rightarrow e^- \bar{\nu}_e \nu_\tau$ mode.

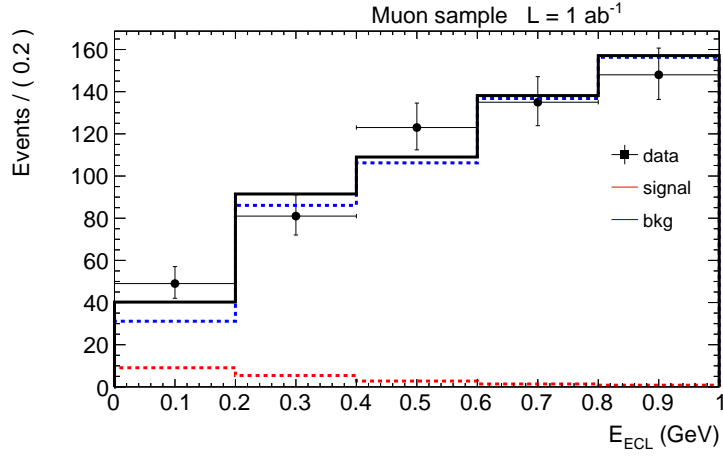


Figure 4.50: Simultaneous fit to E_{Extra} distribution on data-challenge sample for the $\tau^- \rightarrow \mu^- \bar{\nu}_\mu \nu_\tau$ mode.

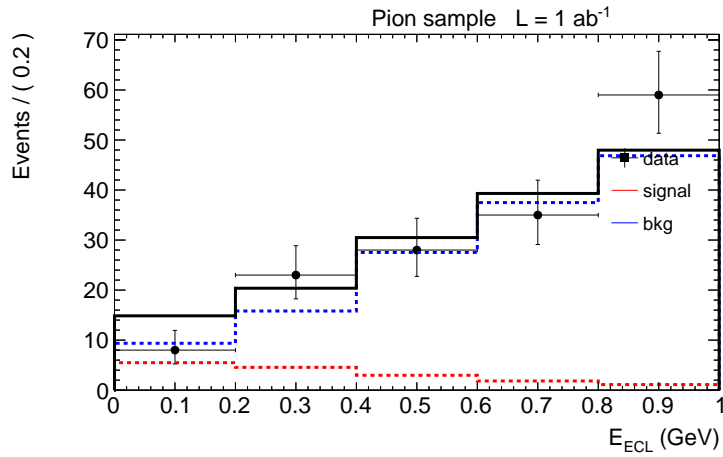


Figure 4.51: Simultaneous fit to E_{Extra} distribution on data-challenge sample for the $\tau^- \rightarrow \pi^- \nu_\tau$ mode.

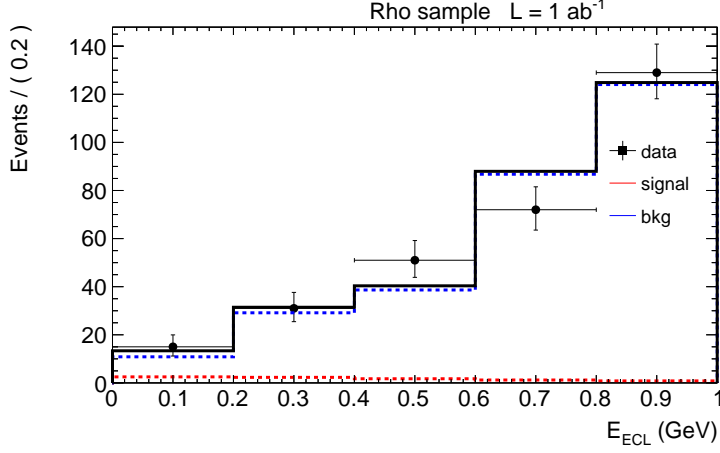


Figure 4.52: Simultaneous fit to E_{Extra} distribution on data-challenge sample for the $\tau^- \rightarrow \pi^- \pi^0 \nu_\tau$ mode.

The simultaneous fit to the common parameter B results in:

$$\mathcal{B}(B \rightarrow \tau\nu)_{simultaneous} = (0.94 \pm 0.37) \times 10^{-4}.$$

The results obtained in this analysis from the global fit and the simultaneous fit to E_{Extra} distribution are in good agreement with the branching ratio measured from the Belle collaboration [30]:

$$\mathcal{B}(B \rightarrow \tau\nu)_{Belle} = [0.72_{-0.25}^{+0.27}(stat) \pm 0.11(syst)] \times 10^{-4},$$

and with the average of Belle and BaBar measurements [14]:

$$\mathcal{B}(B \rightarrow \tau\nu) = (1.06 \pm 0.20) \times 10^{-4}.$$

Conclusions

In the first part of the analysis the τ -pairs production has been studied on collision data collected during the so-called Phase II and corresponding to an integrated luminosity of 480 pb^{-1} . Events from 3-prong and 1-prong decay channels of τ lepton have been selected. After a selection optimized to enrich the data sample in signal events, the distributions of the main variables have been compared to evaluate the agreement between experimental data and MonteCarlo simulation. A data-driven technique has been developed to obtain a separation of electron and muon candidates based on the ratio between the energy released in the electromagnetic calorimeter and the momentum of the track measured by the drift chamber.

In the second part of the analysis a sensitivity study of the leptonic $B \rightarrow \tau\nu$ decay has been performed on different MonteCarlo samples produced in the Belle II experiment. For each event a B mesons (B_{tag}) has been reconstructed by means of its hadronic decay modes through the Full Event Interpretation technique. The precision on the branching ratio measurement of the $B \rightarrow \tau\nu$ decay has been studied on MonteCarlo simulation by searching for the four main 1-prong decay channels of τ lepton: $\tau \rightarrow e\nu\bar{\nu}$, $\tau \rightarrow \mu\nu\bar{\nu}$, $\tau \rightarrow \pi\nu$ and $\tau \rightarrow \rho\nu$. Selection requirements have been applied to reject background events using different discriminators. For each level of selection, the signal yield has been evaluated by performing an extended maximum likelihood fit to E_{Extra} (i.e. the energy of charged tracks and neutral clusters not assigned to any reconstructed B meson) distribution of signal plus background. Therefore the selection requirements have been optimized by minimizing the statistical uncertainty in the signal yield fit results. The uncertainties for each configuration of selection criteria have been determined

by means of toy MonteCarlo experiments generated from the known E_{Extra} probability density functions of signal and background. Established the overall signal selection, the cross feeds and correctly-reconstruction efficiencies have been evaluated as well as the expected number of signal events and the statistical significance. The expected systematic uncertainty on $B \rightarrow \tau\nu$ branching ratio with an integrated luminosity of $1ab^{-1}$ has been estimated to be $\sim 13\%$, based on a scaling of the uncertainties of the Belle measurement with hadronic tag method. Projections in terms of luminosity have been developed in order to evaluate the uncertainties on the branching ratio measurement and the expected statistical significances. The luminosity needed to reach a 5σ discovery of $B \rightarrow \tau\nu$ has been estimated to be about $3.2ab^{-1}$. Subsequently, the agreements between data-challenge and MonteCarlo samples have been checked in the M_{bc} and E_{Extra} sidebands. Finally the branching ratio of $B \rightarrow \tau\nu$ has been measured with the data-challenge sample by performing an extended maximum likelihood fit to the global E_{Extra} distribution of signal plus background:

$$\mathcal{B}(B \rightarrow \tau\nu)_{global} = (1.0 \pm 0.4) \times 10^{-4},$$

and a simultaneous extended maximum likelihood fit to E_{Extra} distributions corresponding to the four τ decay modes:

$$\mathcal{B}(B \rightarrow \tau\nu)_{simultaneous} = (0.94 \pm 0.37) \times 10^{-4}.$$

The results are in good agreement with each other and with the previous measurements performed by Belle collaboration.

Future developments may concern the optimization of the signal selection to reduce the statistical uncertainty on the signal yield, refining the continuum rejection and estimating the peaking background contribution in order to reject it. This background mainly consists of semileptonic B decays with K_L in the final state and one or more particles outside the detector acceptance, faking the 1-prong signal signature. In addition the FEI algorithm needs to be calibrated on real collision data, as the efficiency of tag modes may differ in data and MC. Correction factors can be evaluated for each of the tag modes using as reference well known control samples (as $B \rightarrow D^*l\nu$).

Bibliography

- [1] T.D. Lee, C.N. Yang, Phys. Rev. 104 (1956) 254.
- [2] C.S. Wu et al., Phys. Rev. 106 (1957) 1412.
- [3] R.P. Feynmann, M. Gell'Mann, Phys. Rev. 109 (1958) 193.
- [4] S.L. Glashow, Nucl. Phys. 2 2, 579 (1961).
- [5] S. Weinberg, Phys. Rev. Lett. 19, 1264 (1967).
- [6] M. Thomson, Modern Particle Physics, (2013).
- [7] N. Cabibbo, Phys. Rev. Lett. 10, 531 (1963).
- [8] M. Kobayashi and T. Maskawa, Prog. Th. Phys. 49, 652 (1973).
- [9] L.L. Chau and W.Y. Keung, Phys. Rev. Lett. 53, 1802 (1984).
- [10] L. Wolfenstein, Phys. Rev. Lett. 51, 1945 (1983).
- [11] A.J. Buras, M.E. Lautenbacher and G. Ostermaier, Phys. Rev. D 50, 3433 (1994).
- [12] J.D. Bjorken, Phys. Rev. D 39, 1396 (1989).
- [13] C. Jarlskog and R. Stora, Phys. Lett. B 208, 268 (1988).
- [14] M. Tanabashi et al., (Particle Data Group), Phys. Rev. D 98, 030001 (2018).
- [15] J. Charles et al., (CKMfitter group), Eur. Phys. J. C 41,1 (2005).

- [16] W.S Hou, Phys. Rev. D48, 2342 (1993).
- [17] K. Hara, (Belle Collaboration), arXiv:0810.3301 (2008).
- [18] Belle II Collaboration, Belle II Technical Design Report, arXiv:1011.0352 (2015).
- [19] C. Patrignani et al., Chin. Phys. C40 10 (2016).
- [20] A.J. Bevan et al., Eur. Phys. J. C74 3026 (2014).
- [21] E. Kou et al., The Belle II Physics Book, arXiv:1808.10567 (2018).
- [22] Y. Ohnishi et al., Progress of Theoretical and Experimental Physics 2013.3 (2013).
- [23] M. Bona et al., Conceptual Design Report, arXiv:0709.0451 (2007).
- [24] S. Agostinelli et al., Nucl. Instrum. Meth. A506 (2003).
- [25] I. Antcheva et al., Comput. Phys. Commun. 180.12. (2009).
- [26] N. Katayama et al., Comput. Phys. Commun. 110 (1998).
- [27] R. Brun and F. Rademakers, Nucl. Instrum. Meth., 389 (1997).
- [28] V. Bartsch and G. Quast, CMS Note 2005/004.
- [29] K. Cranmer, Statistical Challenges for Searches for New Physics at the LHC, arXiv:physics/0511028 (2005).
- [30] K. Hara et al., Phys. Rev. Lett. 110.131801 (2013).